Influence of water on mechanical properties of cellulosic materials studied by AFM based methods

by
Dipl.-Ing. Christian Ganser
submitted in fulfillment of the requirements for the degree of
Doktor der montanistischen Wissenschaften
at the Institute of Physics
University of Leoben, Austria

under supervision of
Ao. Univ. Prof. Dr. Christian Teichert

refereed by
Ao. Univ. Prof. Dr. Christian Teichert
and
Ao. Univ. Prof. Dr. Robert Schennach

Leoben, July 2014

dedicated to my family

Eidesstattliche Erklärung

Ich erkläre an Eides statt, dass ich diese Arbeit selbständig verfasst, andere als die angegebenen Quellen und Hilfsmittel nicht benutzt und mich auch sonst keiner unerlaubten Hilfsmittel bedient habe.

Affidavit

I declare in lieu of oath that I wrote this thesis and performed the associated research myself, using only literature cited in this volume.

Dipl.-Ing. Christian Ganser
Leoben, July 2014

Abstract

Cellulosic materials constitute the basis for a variety of products such as several kinds of papers, medical and hygiene articles, as well as building materials. One of the most important cellulose products is paper, with uses ranging from data storage to packaging applications. Even though papermaking is practiced and continuously improved for several thousand years, the detailed mechanisms constituting a bond between two fibers are still elusive. In fact, some mechanisms – ranging from hydrogen bonds to mechanical interlocking – have been proposed, however, it is not clear to which extent these mechanisms contribute or if all of them have been identified yet. But exactly this information is of crucial importance when strength of paper is to be improved, without increasing the material input.

Hydrogen bonds and similar interactions exhibit a maximum effect when the area of the fiber-fiber bond in molecular contact is as high as possible. This would be the case when the surfaces are smooth, soft, and compliant. To assess the structure and mechanical properties of surfaces, atomic force microscopy (AFM) and AFM based nanoindentation (AFM-NI) was employed in this work. A developed measurement setup provided a possibility to control relative humidity and thus to study the influence of water on the materials under investigation. Also, measurements of fully swollen fibers in water were facilitated. This corresponds to the state in which bonds initially form during papermaking. Since paper fibers are a complex and inhomogeneous system, the characterization started with amorphous cellulose films and viscose fibers as model systems. These chemically and structural homogeneous materials permit to focus only on single mechanisms.

Topographical AFM investigations of cellulose films – before and after a bond had been formed between them – revealed that the initial roughness of 30 nm decreased to one third after the rupture of the bond. It was further observed that the surfaces were homogeneous which confirms that smooth surfaces are able to form a large area in molecular contact.

All materials' mechanical properties were determined by AFM-NI as reduced modulus – a measure for the Young's modulus – and hardness under controlled humidity as well as in water. Viscose and pulp fibers both exhibited a reduced modulus in water of about 0.05 GPa. For viscose fibers, this corresponds to a reduction by a factor of almost 200 compared to the dried state. Pulp fibers, on the other hand, are more compliant in dry conditions and, therefore, the reduced modulus in water decreased only by a factor of 100 to 150. The surface hardness of viscose fibers in water is approximately 14 MPa which is a decrease by a factor of 30 compared to the fully dried state. Pulp fibers, on the other hand, exhibited a hardness of 7 MPa in water, which corresponds to a decrease by a factor of 50 to 100, with respect to the dried state. Both materials exhibited an approximately linear relation between hardness and modulus with relative humidity. A deviation from the linear behavior was observed only at high humidities of more than 80 %.

The study has further proven that AFM-NI is an appropriate tool to investigate cellulose based materials under various relative humidities as well as fully swollen materials in water.

Kurzfassung

Cellulosische Materialien bilden die Basis für vielerlei moderne Produkte wie zum Beispiel verschiedene Papiersorten, Medizin- und Hygieneartikel und Baustoffe. Dabei ist Papier einer der wichtigsten Vertreter mit Anwendungen die von Datenspeicherung bis hin zu Verpackungsmaterial reichen. Obwohl die Papierherstellung seit mehreren tausend Jahren praktiziert und ständig verbessert wird, sind die Ursachen, die die Bindung zwischen zwei Papierfasern ausmachen, noch nicht vollständig geklärt. Zwar wurden verschiedene Mechanismen, beginnend mit Wasserstoffbrückenbindungen bis hin zu formschlüssigen Verbindungen, vorgeschlagen, doch ist weder bekannt mit welchem Ausmaß sie beitragen, noch ob bereits alle identifiziert worden sind. Genau diese Informationen sind jedoch von erhöhter Wichtigkeit, wenn die Festigkeit von Papier gesteigert werden soll, ohne aber die Menge an Material zu erhöhen.

Wasserstoffbrückenbindungen und vergleichbare Wechselwirkungen haben dann einen maximalen Effekt, wenn die Fläche der Faserbindung in molekularem Kontakt so groß wie möglich ist. Dies ist dann der Fall, wenn deren Oberflächen gleichmäßig beschaffen, weich und nachgiebig sind. Um die Struktur und die mechanischen Eigenschaften von Oberflächen zu bestimmen, wurde in dieser Arbeit Rasterkraftmikroskopie (AFM) und AFM basierte Nanoindentation (AFM-NI) eingesetzt. Ein speziell entwickelter Messaufbau ermöglichte, die relative Feuchtigkeit zu kontrollieren und so den Einfluss von Wasser auf die untersuchten Materialien zu studieren. Ebenso wurden Messungen an vollständig gequollenen Proben in Wasser ermöglicht. Dies ist der Zustand in dem sich Bindungen während der Papierherstellungen ausbilden. Da Papierfasern ein komplexes und inhomogenes System bilden, wurden zuerst amorphe Cellulosefilme und Viskosefasern als Modellsysteme charakterisiert. Diese chemisch und strukturell homogenen Materialien erlauben, den Fokus gezielt auf einzelne Mechanismen zu richten.

Topographische AFM Untersuchungen an Cellulosefilmen bevor und nachdem eine Bindung zwischen ihnen hergestellt wurde, zeigten dass die anfängliche Rauigkeit von 30 nm auf ein Drittel abgesunken war. Weiters war die resultierende Oberfläche homogen und bestätigte damit, dass glatte Oberflächen die Möglichkeit haben eine hohe Fläche in molekularem Kontakt auszubilden.

Die mechanischen Eigenschaften aller Materialien wurden mittels AFM-NI in Form von reduziertem Modul – ein Maß für den Elastizitätsmodul – und Eindringhärte bestimmt. Die Messungen wurden unter verschiedenen Luftfeuchtigkeiten sowie in Wasser durchgeführt. Sowohl Viskose- als auch Papierfasern wiesen in Wasser einen reduzierten Modul von 0.05 GPa auf. Dies bedeutet für Viskosefasern eine Reduktion um einen Faktor von fast 200 verglichen mit dem getrockneten Zustand. Papierfasern, andererseits, sind im Trockenen etwas nachgiebiger, daher nimmt der reduzierte Modul nur um einen Faktor zwischen 100 und 150 ab. Die Oberflächenhärte von Viskosefasern beträgt in

Wasser 14 MPa, was einer Abnahme um den Faktor 30, verglichen mit dem getrockneten Zustand, bedeutet. Papierfasern wiesen in Wasser allerdings eine Härte von nur 7 MPa auf, was einer Reduktion um einen Faktor von 50 bis 100 bezogen auf den getrockneten Zustand entspricht. Beide Materialien wiesen in etwa einen linearen Zusammenhang von Härte und Modul mit der relativen Feuchte auf. Ein Abweichen davon konnte erst bei hoher Luftfeuchtigkeit von über 80 % beobachtet werden. Es wurde mit der Studie gezeigt, dass außerdem AFM-NI ein geeignetes Werkzeug ist, um cellulosebasierte Materialien zu untersuchen, sowohl in verschiedenen relativen Luftfeuchtigkeiten als auch im gequollenen Zustand in Wasser.

Acronyms

1D	One-dimensional
2D	Two-dimensional
ACF	Auto-correlation function
ACovF	Autocovariance function
AFM	Atomic force microscop(e/y)
AFM-NI	AFM based nanoindentation
CCF	Cross-correlation function
CCovF	Cross-covariance function
CMC	Carboxymethyl cellulose
CS	Cationic starch
DFT	Discrete Fourier transform
DMSO	Dimethyl sulfoxide
DP	Degree of polymerization
FFT	Fast Fourier transform
FT	Fourier transform
GAB	Guggenheim-Anderson-de Boer
HHCF	Height-height correlation function
iDFT	Inverse discrete Fourier transform
iFT	Inverse Fourier transform
L	Lumen
ML	Middle lamella
NI	Nanoindentation

P	Primary wall
P - z	Load-vs-distance
P - z_i	Load-vs-indentation depth
PSD	Power spectral density
RMS	Root mean square
S1	Secondary wall number one
S2	Secondary wall number two
S3	Secondary wall number three
SEM	Scanning electron microscopy

List of Symbols

$A(z)$	Area function
$C(\rho)$	Height height correlation function
D_f	Fractal dimension
D_t	Topological dimension
E	Young's modulus
E_r	Reduced modulus
$F(f)$	Fourier transformation of f
H	Hardness
L	Observation length
P	Load
S	Stiffness
α	Hurst parameter
ν	Poisson's ratio
ρ	Lag
σ	Root mean square roughness
φ_r	Relative humidity
ϑ	Temperature (in ℃)
ξ	Lateral correlation length
ξ_c	Cut-off length
b	Width (of a cantilever)
$f(x, y)$	Arbitrary function of the real-valued variables x and y
f_r	Resonance frequency
$f_{(p)(q)}$	Arbitrary function of the discrete variables p and q
k	Spring constant (of a cantilever)
l	Length (of a cantilever)
r_{sp}	Setpoint ratio
s	Thickness (of a cantilever)
w	Gravimetric water content
x	x coordinate, fast scanning axis
y	y coordinate, slow scanning axis
z	z coordinate, vertical coordinate of the AFM tip
z_c	Contact depth during indentation
z_d	Cantilever deflection

z_i	Indentation depth
z_p	Persistent indentation depth
$z_{a,free}$	Free oscillation amplitude
$z_{a,sp}$	Amplitude setpoint
z_{max}	Maximum indentation depth

Contents

1. Motivation

Cellulose is the most abundant bio-polymer on the face of earth with an annual production of about 1.5×10^{12} tons [1]. It is not surprising that cellulose-containing materials were one of the earliest to be used by our ancestors. Cotton, flax, jute, and others were appreciated as base materials for textile fabrics [2], whereas wood could be shaped into tools and used as a construction material. By disintegrating wood (and other cellulosic materials gathered from plants) into its cells, it was possible to form flexible sheets out of it – paper. Most of these materials are still used in a very similar fashion as they were millennia ago.

1.1. Paper

One of the most important cellulose based materials is paper. It was developed several thousand years ago [3] and is used as an information carrier, packaging material, and for hygiene products, such as tissues. Although paper is known and produced for thousands of years, the detailed mechanisms holding the material together are still elusive. Nevertheless, five mechanisms that could contribute to the strength of a bond between two paper fibers have been identified [4]:

1. hydrogen bonds
2. van der Waals interactions
3. Coulomb interactions
4. interdiffusion of cellulose molecules
5. mechanical interlocking

It is, however, unknown to which extent these mechanisms contribute and if there are additional ones present. Also capillary bridges [5,6] and microcompressions induced by stresses during drying of the fibers [7,8] are likely to have an effect on the bond strength.

The detailed knowledge of fiber-fiber bonding is important when one seeks to improve paper for a certain application. Cement bags, for instance, should withstand the weight of their contents and still be permeable when filling the bag with a gas stream. Another example are shopping bags: They need the strength to hold the groceries, while being cheap with little environmental impact. Both applications call for a low amount of material which can sustain high loads. This can be achieved by porous paper, with fiber-fiber bonds tuned to yield maximum strength. To have an intimate understanding of how the fibers in the paper network interact with each other would allow to pinpoint and manipulate the correct parameters – push the right buttons, in a sense – and produce paper optimally suited for the application.

From the five bonding mechanisms listed above, numbers one to four would lead to a stronger bond when the area in molecular contact is maximized. The fifth mechanism, on the other hand, depends on the surface structure and its features. To gain understanding of these mechanisms, the mechanical properties of the paper fibers' surfaces and their morphology needs to be known on the *nanometer* scale – the scale on which bond formation takes place. Moreover, bonds are initially formed between highly swollen fibers in an aqueous environment and it is usually insufficient to consider the properties of dried fibers. Both, the mechanical parameters and surface morphology will change drastically – and to some degree irreversibly [9] – after water is removed from the fiber.

1.2. Model systems

Since paper fibers are an inhomogeneous material – as will be discussed in section 2.1 – they are difficult to study. Therefore, model systems are often employed to focus only on a single mechanism.

Cellulose films are one possibility of such a model system. They have the advantage of being chemically pure with an ideally smooth surface. Increasing the system's complexity by adding different species – such as hemicelluloses – is easily achieved. A step towards further complexity are regenerated cellulose fibers, a material with its own, vast field of applications ranging from various textiles, via hygiene products, to paper additives and special papers. In being fibers, they share the same macroscopic appearance as paper fibers and have even microscopic similarities such as fibrils and partly crystallized cellulose. The fact that regenerated fibers are pure cellulose fibers, places them also close to cellulose films. One could, therefore, consider them as a link between model films and paper fibers.

1.3. This work

In this work, a focus is set on mechanical properties of cellulosic materials and on the influence water has on them. The majority of the fiber-fiber bonding mechanisms listed above rely on a high area in molecular contact. Hence, a measure for the fibers' ability to conform to each other is needed. It is long known that yield strength and Young's modulus are such measures. On the nanometer scale, classical nanoindentation is usually employed to determine these properties. Due to the rough nature of paper fibers, the application of this method is limited and likely to result in a large scattering of the data. Therefore, an AFM-based version of nanoindentation is used in this work to approximate these material parameters. By employing a setup to control the environment's water content, the effect of water uptake is studied beginning with the fully dried state until highly swollen materials. While the goal is ultimately to understand the importance of fiber swelling during bond formation in paper, a comprehensive mechanical characterization of cellulosic materials is achieved as well. The present study does not only compare the dry and wet states of cellulose materials, but aims to indicate the transition from one to the other and to demonstrate the effectiveness of industrially available ways to influence the swelling behavior.

This study leads to the result that in the presence of water, the hardness of paper fibers is decreased by a factor of 50 to 100 compared to the dried state. Simultaneously, the stiffness of paper fibers reduces by a factor of 100 to 150 times. While the decrease in hardness for paper fibers is the highest observed in this work, the stiffness is decreasing the most for viscose fibers which become in water approximately 200 times more compliant.

2. Theoretical background

2.1. Cellulose fibers

All cellulose fibers investigated in this work originated from wood. Wood itself is a natural polymer composite consisting mostly of cellulose, hemicelluloses, and lignin which are organized in a hierarchical structure. The smallest elements in the hierarchy are the single molecules, with cellulose being the most important one.

2.1.1. Cellulose, hemicelluloses, and lignin

Cellulose is a polysaccharide of cellobiose, i.e., the repeating unit is two D-glucopyranose molecules linked by a β-(1$\rightarrow$4)-glycosidic bond. A cellulose chain can exhibit a degree of polymerization (DP) of up to 15 000. Note that the DP usually refers to the number of D-glucopyranose units and not to that of cellobiose units. The structural formula of cellulose is sketched in figure 2.1. Cellulose, like many polymers, is able to form crystalline regions which are separated by amorphous areas. In wood, for example, as much as 65 % of the cellulose is crystalline [10].

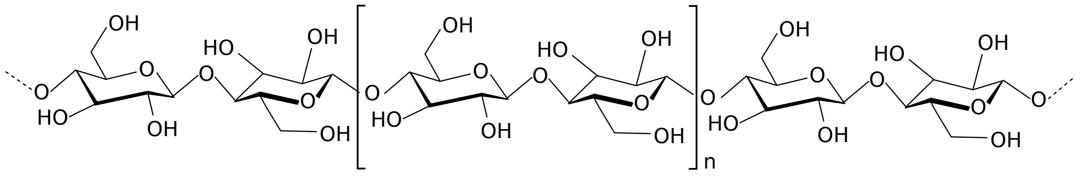

Figure 2.1.: Structural representation of a cellulose molecule. The part in brackets is the repeating unit cellobiose and the DP is $2n$.

Hemicelluloses are – like cellulose – polysaccharides, but they are branched with DPs of only 100 - 200. Also, they do not consist of only one type of cyclic sugar, but several different ones which leads to a large diversity of hemicelluloses. All of them are purely amorphous, without any crystallinity. One of the most common and thereby important groups of hemicelluloses are xylans [10].

Lignin, similar to hemicelluloses, is a group of diverse, branched and amorphous polymers. However, these bio-polymers are not polysaccharides but consist of a complex, three-dimensional structure of aromatic units [10].

2.1.2. Wood

The aforementioned hierarchical structure of wood is sketched in figure 2.2, using softwood tracheids as an example. Cellulose chains pack together to form elementary fibrils with crystalline and amorphous regions. The elementary fibrils (<10 nm in diameter), in turn, bundle to form microfibrils (10 nm - 60 nm in diameter) [11,12]. These microfibrils compose the cell wall of wood cells by winding helically around a central void called the *lumen* (L). Such cells are composed of layers, with the primary layer (P) being the outermost one. Beyond P, the secondary layers one to three (S1, S2, S3) follow, where S2 is by far the thickest layer and determines the mechanical properties of the cell. In the P layer, the microfibrils are arranged in a disordered fashion, whereas in the layers S1 to S3 highly oriented fibrils are found. After S3, the lumen is located, which is used for water transport in the tree. Between the cells, the middle lamella (ML) is located, which is rich in lignin. Lignin and hemicelluloses are located between the nano- and microfibrils and are thought of as a glue that adds stiffness to the wood [13,14].

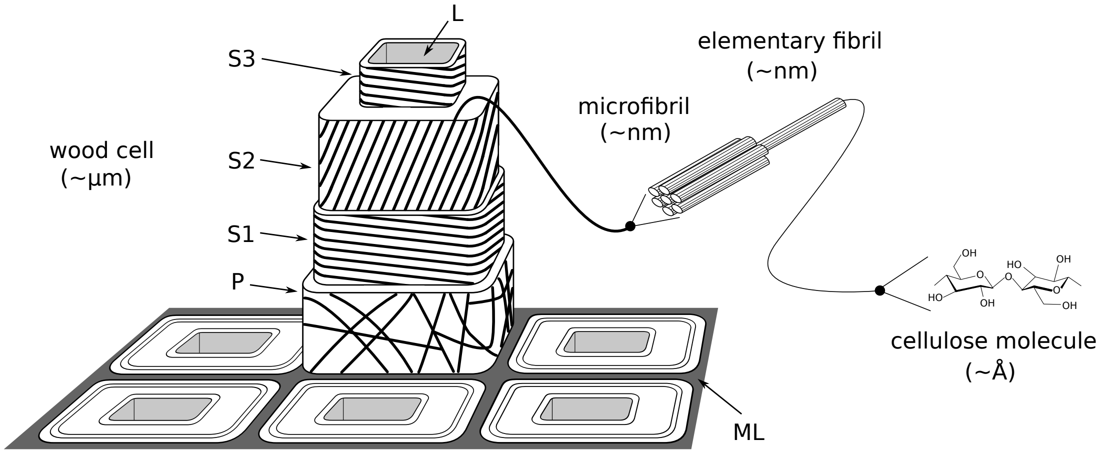

Figure 2.2.: The hierarchical structure of wood by example of a conifer tracheid. Starting with a single cellulose molecule, a complex system is formed. The units in brackets denote the characteristic length scale of the respective hierarchy level.

Tree cells are mostly aligned in the longitudinal direction of the stem and are alive only in its outer region. This region is called *cambium* and is protected from outside influences by the bark. The cambium is the growth zone of a tree, where cell division takes place. In this zone, the lumina of the cells are still filled with protoplasm. The protoplasm is excreted when the cells mature and turn into cyclic arrest to form the *xylem*, the part of a tree which is commonly known as wood. In a living tree, the trunk consists mostly of dead cells which provide mechanical strength and the possibility to transport water and minerals throughout the plant [15].

Hardwood and softwood

Woods can be grouped in softwoods – or *conifers* – which are gymnosperms and hardwoods, which are angiosperms. The wood of conifers consists basically of only two types of cells: the longitudinally aligned *tracheids* (shown in figure 2.2), and *rays*, which connect the tracheids radially. Tracheids in softwood provide channels for water transport in their lumina and – at the same time – are also responsible for a tree's mechanical stability due to their thick S2 layer. Cells of hardwoods, on the other hand, are more differentiated. So-called *fibers* with thick cell walls provide mechanical strength to the plant, whereas *vessels* function as conduits for water. The aforementioned rays are also present in hardwood [15,16]. In addition, the amount and the types of hemicelluloses and lignin present in the wood differ between softwood and hardwood as well. While the most common hemicelluloses in softwoods are galactoglucomannan and arabinoglucuronoxylan, in hardwoods glucuronoxylan and glucomannan are the dominant ones [10,16].

2.1.3. Kraft pulp fibers

To produce paper, the aforementioned wood cells have to be extracted from the wood first. This can be achieved by mechanical and/or chemical methods. Afterwards, the freed cells – commonly named pulp fibers – are dispersed into a dilute aqueous suspension and basically poured onto a filter. The water is drained and the fibers move closer together, forming a loose sheet. During drying, bonds form between the pulp fibers and the sheet gains strength.

The name *kraft pulp* refers to softwood pulp, extracted by the so-called kraft (sulfate) process. In this pulping process, lignin and hemicelluloses are removed chemically from the wood, leading to the disintegration into its cells. Since the matrices of the pulp fibers are weakened by the loss of lignin and hemicelluloses, the fibers collapse, as is presented schematically in figure 2.3.

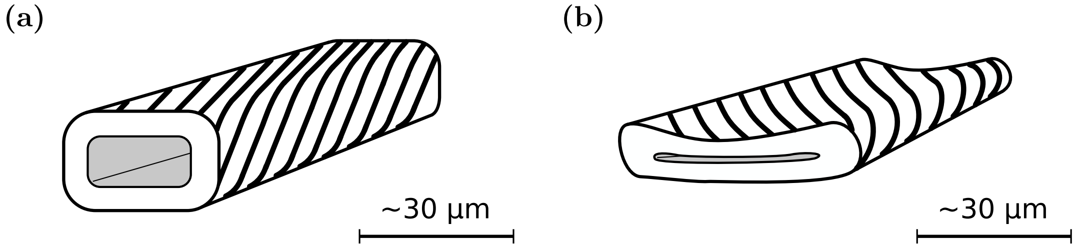

Figure 2.3.: The micrometer scale structural effect of kraft pulping on wood cells. (a) Before pulping, the cell is stiff and the lumen is open. (b) After pulping, the lumen collapses, leading to a cross-section typical for pulp fibers.

Refining

The process of refining refers to a mechanical treatment of pulp fibers. There, the pulp is ground in a mill consisting of two plates with ribs attached to them. One plate is rotating and the other is fixed, so that a shear force is exerted on the pulp. This treatment increases the flexibility of pulp fibers, leading to highly conformable fibers. Furthermore, some microfibrils are released and dangle loosely from the fibers. This process is long known to increase the strength of paper. A recent study, however, could give for the first time evidence about the mechanism underlying the beneficial effect of refining [17].

2.1.4. Regenerated cellulose fibers

Properties of pulp fibers are obviously advantageous for papermaking and can be tuned to produce a large variety of papers. However, the use of pulp fibers in other areas, such as textiles, would be quite limited. Reasons for that are their short length of only a few millimeters, a predefined cross-section, and the limited possibility to incorporate additives. Cotton fibers, on the other hand, are very long and, therefore, can be spun into yarns to be used in textile fabrication. However, also they lack in geometrical and chemical tunability. A way around these limits was discovered in the 19th century by dissolving the cellulose of natural materials and spinning it into fibers with a desired geometry. This process is called *regeneration* [11]. Today, several methods to regenerate cellulose are known. Examples are the viscose, modal, and NMMO (lyocell) processes, with viscose being the industrially most important one.

Viscose fibers

In the viscose process, pulp is first treated with sodium hydroxide (NaOH) to form sodium (Na) cellulose. The swollen Na-cellulose is then treated with carbon disulfide (CS_2) to generate cellulose xanthogenate, which is soluble in aqueous NaOH. This yields a viscous solution, called the *viscose dope*. Dissolved cellulose xanthogenate is then spun through a spinneret into fibers, which are regenerated in a spinning bath consisting mainly of aqueous sulfuric acid (H_2SO_4). The result is a pure cellulose fiber where the cross-section is determined by the shape of the holes in the spinneret. To adjust the length, fibers can be simply cut into the desired length directly after spinning. Compositional modifications are achieved by adding substances directly into the viscose dope [1,11].

Viscose fibers differ in composition and structure from pulp fibers. Regenerated cellulose exhibits a crystalline structure different from the one found in wood. Crystalline wood cellulose is called cellulose I, whereas regenerated cellulose crystallizes as cellulose II. It is believed that cellulose II is the thermodynamically more stable structure [1].

The amount of crystalline domains in viscose fibers is reported to be mostly between 30 % and 50 %, [1,18,19] but can be as much as 68 % [20]. This number, however, seems strongly dependent on the exact process parameters and modifications. Large variations between fibers of different manufacturers are, therefore, expected.

The DP of cellulose in viscose is approximately 300, which is much lower than the one of pulp fibers (DP $\approx$ 1000 to 2000) [11,19–21].

Applications of viscose fibers range from textiles and hygiene articles to special papers such as for money bills. For some time, the ability of viscose fibers to enhance the mechanical properties of paper has been investigated [22]. In academic research, viscose fibers have recently been used as model systems to investigate mechanisms of fiber-fiber bond formation in paper [23].

2.2. Atomic force microscopy

Atomic force microscopy (AFM) is a technique where a sharp tip at the end of a cantilever is scanned across a surface to record its topography [24]. The operation principle of AFM is presented in figure 2.4a. Frequently, the sample is scanned laterally in x and y directions, while the cantilever is fixed in a holder which can move only in z direction. The movement in x, y, and z is usually achieved by employing piezo actuators, which allow sub-nm position accuracy. Scanning is performed by moving the cantilever along a line in its longitudinal direction (the fast scanning axis x) and incrementally increasing the slow scanning axis coordinate y after a line was scanned back and forth.

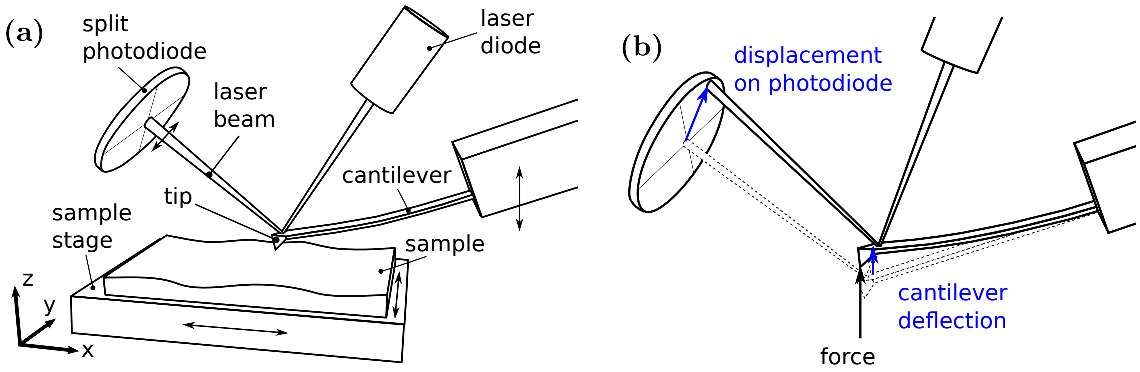

Figure 2.4.: The operating principle of AFM. (a) An illustration of the scanning procedure. Here, the sample moves in x and y, whereas the cantilever moves in z. After [25]. (b) The detection of an applied force by reading out the cantilever's deflection.

In most commercially available systems, a laser beam reflected from the cantilever's backside onto a split photodiode is used to detect its deflection (see figure 2.4b). This is achieved by subtracting the light intensity recorded at the photodiode's lower quarter from the one of the upper quarter. By analyzing the intensity difference between the right and left quarters, the cantilever's torsion can be detected. For small deflections z_d, it is possible to calculate the force that leads to the bending of the cantilever by the linear relation

$$F = kz_d. \tag{2.1}$$

The spring constant k depends only on the cantilever's geometry (width b, length l, and thickness s) and Young's modulus E. For a rectangular, uniform cross-section of the cantilever the spring constant is

$$k = \frac{Ebs^3}{12l^3}. \tag{2.2}$$

Using a feedback loop to keep the deflection at a constant value by moving it in z and scanning the sample in x and y directions, the sample's surface topography is recorded as $z(x, y)$. This is the most simple imaging procedure and is called *contact mode*. It is likely that the surface will be influenced – or even severely damaged – due to the constant lateral force that is exerted.

To prevent this entirely, the AFM can be operated in *non-contact mode* [26]. There, the cantilever is excited at its resonance frequency f_r and oscillates without touching the surface. Since a force gradient emanates from each surface, e.g. due to van der Waals interactions, the effective k – and thereby f_r – depends on the distance between tip and sample. By adjusting z to keep f_r constant, the topography signal is recorded again as $z(x, y)$. The disadvantage of non-contact mode is that it basically works best only in ultra-high vacuum, where it yields sub-atomic resolution.

Intermittent contact mode (also called tapping mode and AC mode) is a compromise between the two described techniques [27]. Here, the cantilever is excited slightly below f_r in close proximity to the surface so that the tip apex is periodically touching the sample. The sample will dampen the oscillation amplitude z_a to a value below its free amplitude $z_{a,free}$. A feedback loop to keep z_a at a constant value – the so-called set-point $z_{a,sp}$ – controls the movement in z to gain the topography $z(x, y)$. A measure for the force applied to the sample during scanning is the amplitude-to-setpoint ratio r_{sp}, with

$$r_{sp} = \frac{z_{a,sp}}{z_{a,free}}. \tag{2.3}$$

The great advantage of intermittent contact mode is that it can be performed in air as well as in liquids [28] and is comparably gentle. The lateral resolution is determined by the radius of the tip apex and is typically below 10 nm. For soft samples, such as a variety of biomaterials, this technique is the preferred choice [29–31]. Additionally, by recording the phase shift between the exciting oscillation and the cantilever's actual oscillation, qualitative information on a material's mechanical properties is obtained [32]. This phase shift is the result of oscillation energy dissipated into the material due to the tip's periodic contact with the surface. A so-called phase image is then generated by plotting the phase shift as a function of x and y coordinates. This method is commonly used on soft samples such as polymers [33,34] and pulp fibers [35].

2.3. Nanoindentation

Nanoindentation (NI) is a technique to determine a material's mechanical properties on the nanometer scale. This is achieved by pressing a tip – the so-called *indenter* – with a defined shape and known elastic properties (elastic modulus E_i and Poisson's ratio ν_i) into a material's surface. During this process, the applied load and the resulting deformation – measured by the *indentation depth* z_i – is recorded constantly. From such a load-vs-indentation depth (P - z_i) plot, the hardness H and the reduced modulus E_r are determined according to the method of Oliver and Pharr [36] which is described in the following.

The hardness H, which is a measure for a material's yield strength, is calculated by

$$H = \frac{P_{max}}{A(z_c)}, \tag{2.4}$$

with P_{max} denoting the maximum applied load and $A(z_c)$ the indenters projected area at contact indentation depth z_c. It is noteworthy that z_c is neither the indentation depth at maximum load, z_{max}, nor the depth of the persistent indent z_p but somewhere in between, as is illustrated in figure 2.5. z_c can be determined by the relation

$$z_c = z_{max} - \epsilon \frac{P_{max}}{S}, \tag{2.5}$$

where S is the unloading stiffness at P_{max}. It can be determined as $S = \frac{dP}{dz}|_{z_{max}}$ like it is indicated in figure 2.5b. The factor ϵ in equation 2.5 depends only on the indenter shape and ranges between 0.72 and 1. For the purpose of this work, ϵ is assumed to be 0.75 which is equivalent to a Berkovich indenter. To gain S, the unloading part of the P - z_i plot (as indicated in figure 2.5b) is first fitted by the function

$$P(z_i) = C(z_i - z_p)^m. \tag{2.6}$$

Evaluating the derivation $\frac{dP}{dz}|_{z_{max}}$ of equation 2.6 with the obtained fit parameters C, z_p, and m yields the unloading stiffness S.

In equation 2.4, the projected area at contact depth $A(z_c)$ is usually determined by evaluating the indenter's area function $A(z)$ at $z = z_c$. $A(z)$ is obviously only dependent on the indenter's geometry and is obtained by either calibrating the indenter on a material with known mechanical properties [36] or by directly imaging the indenter by SEM or AFM [37,38]. A discussion about methods to experimentally obtain the area function is presented in subsection 3.2.1.

The reduced modulus E_r is calculated via

$$E_r = \frac{\sqrt{\pi}}{2} \frac{S}{\sqrt{A(z_c)}} \tag{2.7}$$

and is a measure for a material's Young's modulus E_s [36]. If the material under investigation is isotropic – like, e.g., polycrystalline metals – E_r and E_s obey the relation

$$\frac{1}{E_r} = \frac{(1-\nu_s^2)}{E_s} + \frac{(1-\nu_i^2)}{E_i}. \tag{2.8}$$

ν denotes the Poisson's ratio and indices s and i identify sample and indenter properties, respectively. If $E_s \ll E_i$, then equation 2.8 can be simplified to

$$E_r \approx \frac{E_s}{(1-\nu_s^2)}, \tag{2.9}$$

which has the advantage of being independent from the indenter properties. However, equation 2.9 requires still the Poisson's ratio of the sample ν_s.

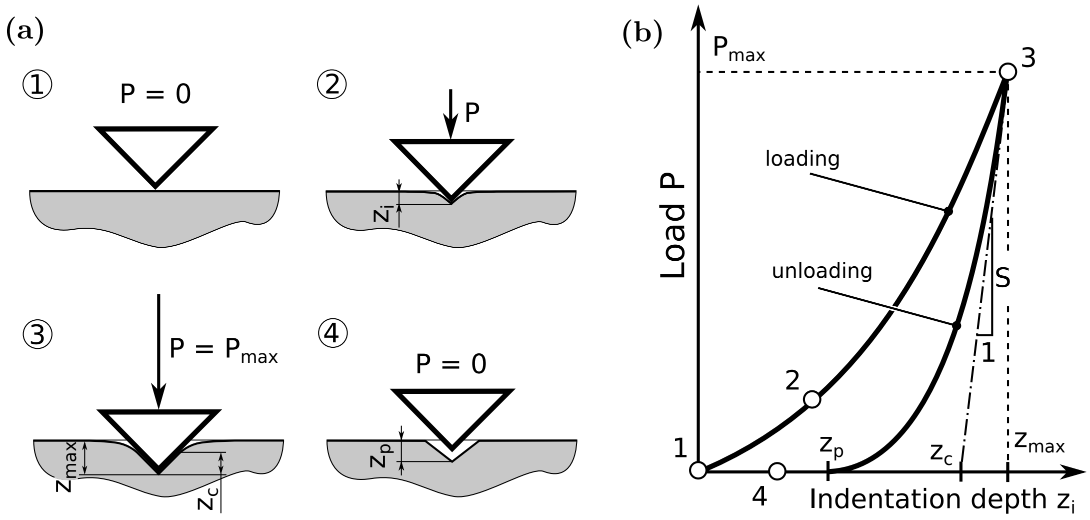

Figure 2.5.: The working principle of classical nanoindentation illustrated by (a) the indenter's interaction with the sample and (b) the resulting P - z_i plot. Note that the images in (a) correspond to points in (b) marked with the respective numbers.

2.3.1. Modifications for viscoelastic materials

Viscoelastic materials – such as polymers, including cellulose – feature a time dependent behavior when a load is applied. This time dependence manifests in effects such as creep and relaxation or a load rate sensitivity of the deformation response. These three effects are sketched qualitatively in figure 2.6.

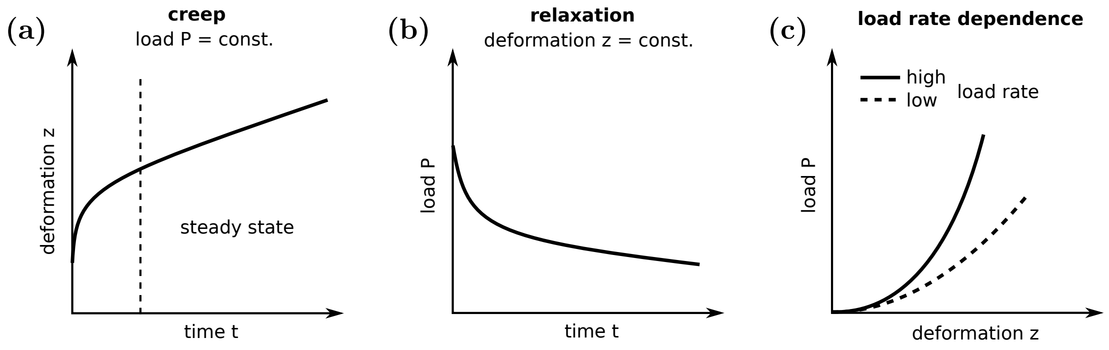

Figure 2.6.: Qualitative illustration of the time and load rate dependence of viscoelastic materials. In (a) the load is constant and the deformation increases with time, in (b) the deformation is constant, and (c) depicts the effect of the load rate.

Creep (figure 2.6a) and load rate dependence (figure 2.6c), will obviously influence the determination of H and E_r. Especially during the unloading segment, a so-called *nose* can form due to creep effects, which is sketched in figure 2.7a [39,40]. The resulting unloading stiffness S as well as the reduced modulus E_r would appear to be negative (according to equation 2.7). To prevent the occurrence of a nose, a holding time $t_{h,c}$ at maximum load P_{max} can be introduced [39–41]. This time of constant load needs to be long enough to ensure that the steady state creep, indicated in figure 2.6a, is reached. Only in this case, the creep rate $\frac{dz_c}{dt}$ will be at a minimum. A qualitative load schedule with $t_{h,c} \neq 0$ including a possible P - z_i plot is shown in figure 2.7b.

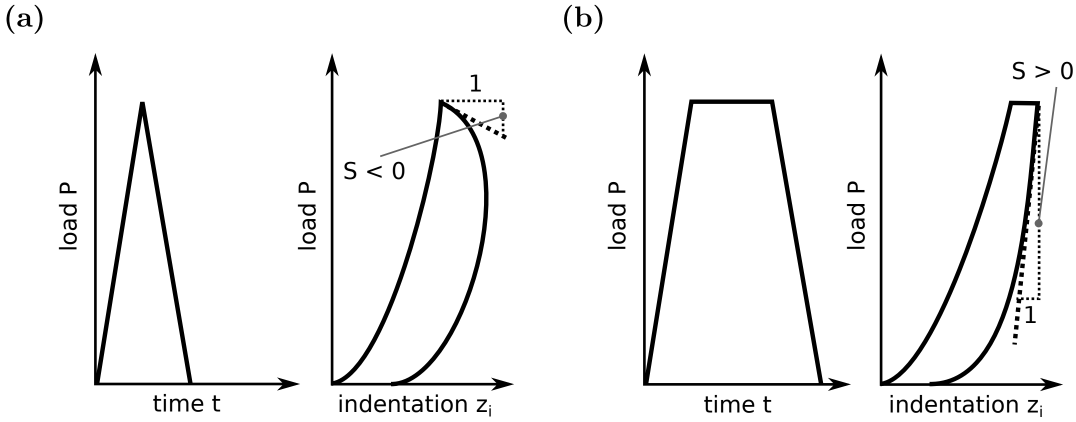

Figure 2.7.: (a) A triangular load schedule and a possible response from a viscoelastic material are sketched. Note that the beginning of the unloading segment features a negative stiffness, which is called a *nose* (b). If a holding time at the load maximum is introduced, the nose can disappear and the stiffness S becomes positive.

Although the introduction of $t_{h,c}$ reduces the influence of creep effects on E_r, it does not cancel the creep effects completely. In order to improve the determination of E_r as well as H of viscoelastic materials, a modification of Oliver and Pharr's method was proposed [39,40]. First of all, the obtained P - z_i plot needs to be corrected for thermal drift effects. For this purpose, a thermal holding time $t_{h,t}$ is introduced near the end of the unloading part. A typical load schedule used for viscoelastic materials is presented in figure 2.8, featuring $t_{h,c}$ and $t_{h,t}$. To determine the thermal drift rate $\frac{dz_t}{dt} = \dot{z}_t$, the thermal holding part of the unloading segment is fitted with

$$z_t(t) = z_{t,0} + \dot{z}_t t. \tag{2.10}$$

Then, $z_i(t)$ is corrected by subtracting the thermally induced change of z_i, i.e.

$$z_i(t) = z_i^{(t)}(t) - \dot{z}_t t. \tag{2.11}$$

In equation 2.11, the uncorrected indentation depth is denoted $z_i^{(t)}(t)$ to avoid confusion. Note that the procedure described here only works if $\dot{z}_t = const.$, which was true for the course of this work.

In the next step, the steady state creep rate $\frac{dz_c}{dt}|_s = \dot{z}_{c,s}$ is determined from the holding segment at P_{max} by fitting the temporal evolution of the creep induced indentation z_c with

$$z_c(t) = z_{c,0} + a(t-t_0)^{\frac{1}{2}} + b(t-t_0)^{\frac{1}{4}} + c(t-t_0)^{\frac{1}{8}}. \tag{2.12}$$

Equation 2.12 has been found empirically to be the best fit [40]. $\dot{z}_{c,s}$ is then gained by differentiating equation 2.12 with respect to time at the end of the holding segment, i.e. $\dot{z}_c(t_{h,c})$. It was shown that an improved value for E_r is then obtained by using the creep-reduced unloading stiffness

$$S^* = \left[\frac{1}{S} + \frac{\dot{z}_c(t_{h,c})}{|\dot{P}|}\right]^{-1}, \tag{2.13}$$

with $|\dot{P}|$ denoting the absolute value of the unloading rate [39]. To gain an improved value for the hardness H, the contact depth is calculated by substituting S with S^* in equation 2.5 [40] which yields

$$z_c = z_{max} - \epsilon\frac{P_{max}}{S^*}. \tag{2.14}$$

Finally, it was also found empirically that for viscoelastic materials, the unloading part is best described by

$$z_i(P) = z_p + dP^{\frac{1}{2}} + eP^{\frac{1}{4}} + fP^{\frac{1}{8}}, \tag{2.15}$$

instead by equation 2.6 [40]. z_p, d, e, and f are parameters to be determined from a least squares fit. Note that while equation 2.6 expresses $P(z)$, equation 2.15 describes $z(P)$.

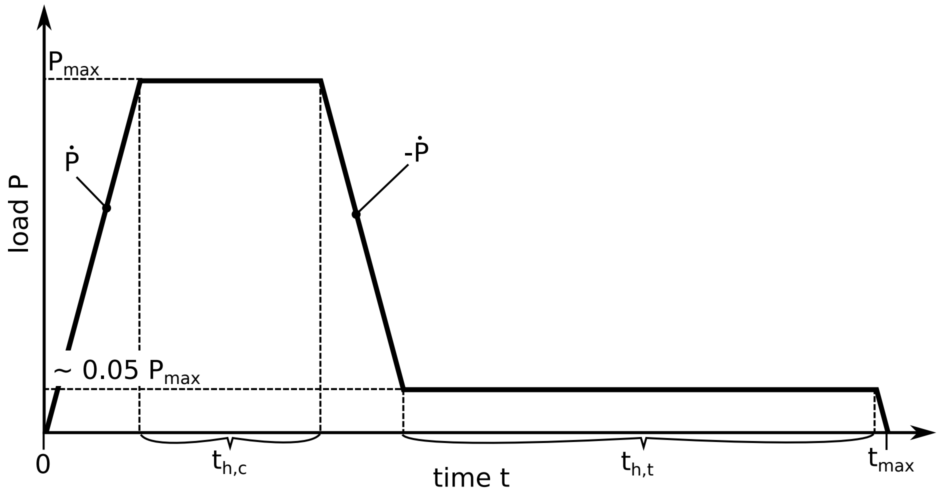

Figure 2.8.: For viscoelastic materials, the load schedule of NI experiments should feature a holding time $t_{h,c}$ at P_{max} to reduce creep effects and a second holding time $t_{h,t}$ close to $P = 0$, to compensate for thermal drifting.

2.3.2. AFM based nanoindentation

When performing nanoindentation, the surface morphology of the sample under investigation will influence the results. Height fluctuations with the same or a higher magnitude as the indentation depth and lateral fluctuations similar or smaller as a characteristic size of the indent during contact will distort the determination of $A(z_c)$ and thereby E_r as well as H. Figure 2.9 presents the effects of surface roughness schematically. In the ideal case (figure 2.9a), the contact area behaves as is assumed by the area function $A(z)$. If, however, a spike protruding from the surface has contact with the indenter (figure 2.9b), the indentation depth z_i is not defined properly, since no indentation takes place. A possible result would be an underestimation of E_r and H by measuring a z_c larger than in the ideal case $z_c^{(i)}$. When the tip indents at a position where a depression in the surface is located (figure 2.9c), a contact area much lower than the actual contact area (indicated in figure 2.9c) is calculated from the P - z_i plot. Thus, E_r and H would be overestimated. It would be, therefore, an asset to image the surface before indentation and select appropriate positions to indent. Although modern nanoindenters have scanning capabilities, only contact mode imaging is possible which is likely to damage soft samples and to contaminate the indenter with debris. AFM, on the other hand, implements the comparatively gentle intermittent contact mode. This feature is the main reason to combine AFM with NI to perform AFM-based nanoindentation (AFM-NI).

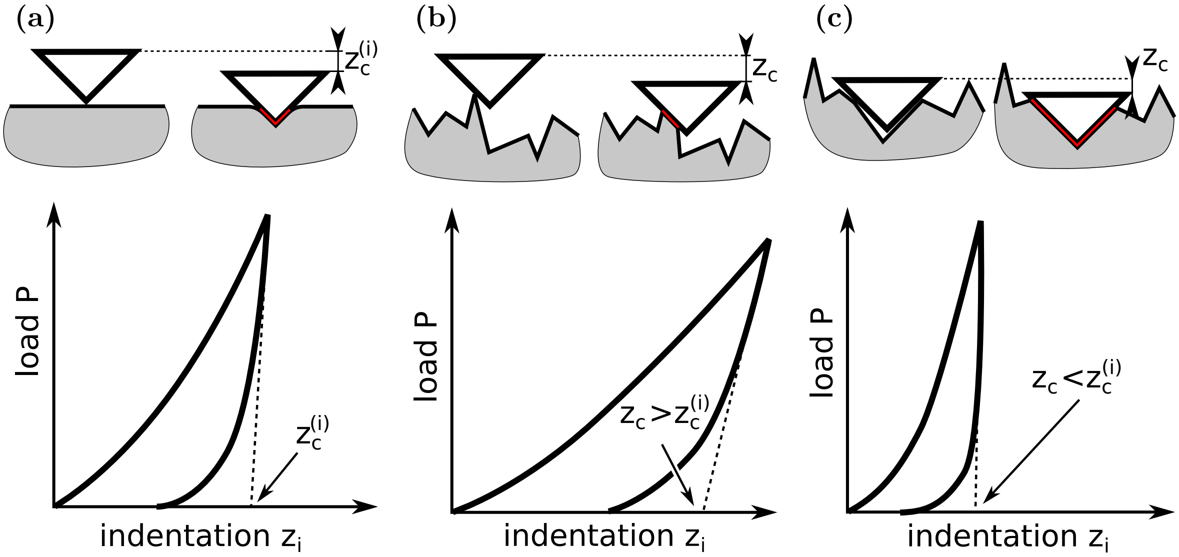

Figure 2.9.: The influence of surface roughness in nanoindentation. (a) presents the ideal case. In (b), only one side of the indenter has contact with the sample, whereas in (c) a hole is indented. The red lines are an indication for the area in contact.

In AFM-NI, the tip that is used to scan a surface represents also the indenter and the AFM cantilever acts as the force sensor and actuator at the same time. This fact implies that the raw data obtained from an AFM-NI experiment is a force-vs-piezo distance

(P - z) plot. In this case, the distance z is the piezo's movement in the vertical direction, measured from the point of contact with the sample (see figure 2.10). Naturally, z is not only composed of the indentation depth z_i but includes also the cantilever's deflection z_d. Therefore, the cantilevers deflection z_d has to be subtracted from z for all collected data points after contact to gain z_i. This is easily performed by

$$z_i(t) = z(t) - z_d(t), \tag{2.16}$$

with t starting at the point of contact $t = 0$ and ending at $t = t_{max}$, which is the end of the load schedule as indicated in figure 2.8. After applying equation 2.16, the resulting P - z_i plot is evaluated using the procedures given previously for classical NI, including the modifications for viscoelastic materials.

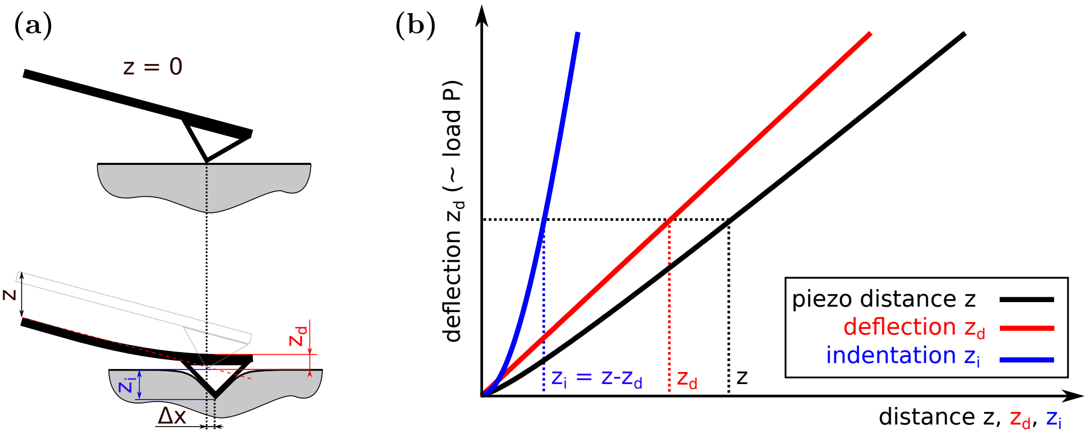

Figure 2.10.: Schematic representation of (a) an AFM-NI experiment and (b) the corresponding P - z plot. Please note that to get the P - z_i plot, the deflection z_d has to be subtracted from the piezo distance z, as is illustrated.

In figure 2.10a, the distance Δx is used to describe the lateral movement of the cantilever during force application. This is the main drawback of AFM-NI. While in classical NI, the force application is purely vertical, lateral force components are induced in AFM-NI, influencing the correct determination of H and E_r. Results obtained by AFM-NI should hence not be used to calculate material's properties like Young's modulus E or yield strength, which is possible for classical NI. However, for cellulosic materials it was found that results from AFM-NI and classical NI are similar when using the evaluation procedures described previously in this section [38].

While classical NI is still the best choice for studying metals, the use of AFM-NI is popular when characterizing soft matter such as polymers [42–44], cells [45], viruses [46], and pulp fibers [37,38,47–50].

2.4. Relative humidity

When studying water uptake of a material from the surrounding air, the relative humidity φ_r is the most important parameter to know. Commonly, φ_r is defined as

$$\varphi_r = \frac{p_{H_2O}}{p^*_{H_2O}(\vartheta)}. \tag{2.17}$$

Here, p_{H_2O} denotes the partial water vapor pressure, i.e. the absolute amount of water present in the air and $p^*_{H_2O}(\vartheta)$ refers to the saturation water vapor pressure. $p^*_{H_2O}(\vartheta)$ describes the maximum amount of gaseous water that can be present at a certain temperature ϑ and is given by the relation

$$p^*_{H_2O}(\vartheta) = \alpha \cdot \exp\left(\frac{\beta\vartheta}{\lambda + \vartheta}\right), \tag{2.18}$$

with ϑ in ℃, $\alpha = 6.112\,\text{hPa}$, $\beta = 17.62$, and $\lambda = 243.12$℃ [51].

It is obvious from equation 2.18 and figure 2.11a that the maximum possible amount of water vapor increases greatly with increasing temperature. Therefore, φ_r will decrease with increasing temperature, since p_{H_2O} will remain constant. On the other hand, if the temperature is lowered, φ_r will increase until $p^*_{H_2O}(\vartheta) = p_{H_2O}$ at which point condensation will occur, as indicated in figure 2.11b.

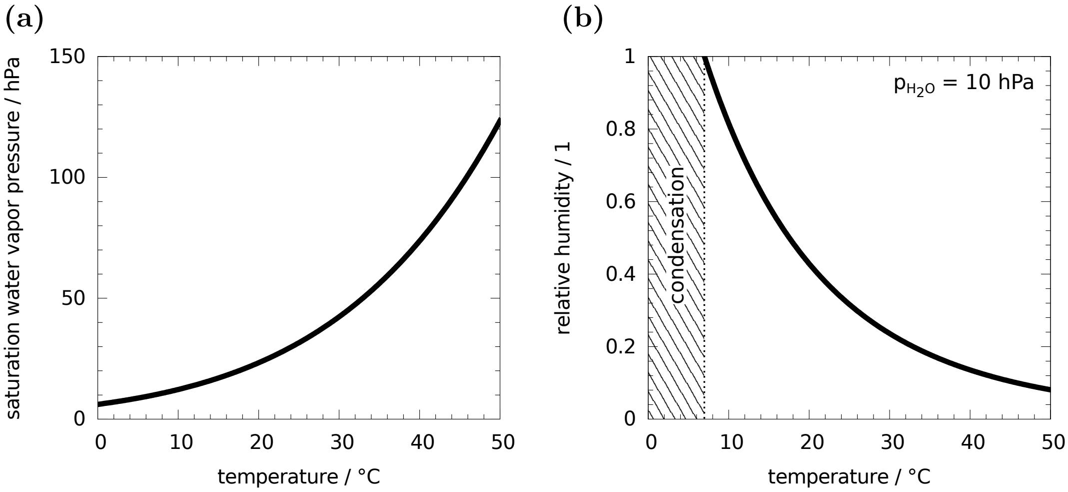

Figure 2.11.: Temperature influence to (a) the saturation water vapor pressure and (b) the relative humidity. Note that in (b) at $\vartheta \approx 7$℃, $\varphi_r > 1$ and thus, condensation would occur.

2.5. Roughness characterization

Atomic force microscopy allows to record a sample's topography with nanometer resolution in lateral directions and sub-nanometer resolution in z-direction as a two-dimensional height map (see section 2.2 for further details). This fact facilitates the use of statistical methods to comprehensively analyze a sample's morphology. In this section, the necessary statistical and mathematical background is covered and brought in context with the fractal geometry of surfaces.

2.5.1. Height-height correlation function

Analytical form

In statistical analysis of time series, the height-height correlation function (HHCF) $C(\rho)$ is known as the autocovariance function (ACovF) [52]. The ACovF is a special case of the cross-covariance function (CCovF) $C_{pq}(\rho),\ (p,q) \in \{1,\,2\}$ of the two functions $f_p(x),\ f_q(x)$. By assuming $f_p,\ f_q$ to be in general complex valued functions with their means $\langle f_p(x)\rangle = \langle f_q(x)\rangle = 0$ and limiting the problem to one dimension, the CCovF is given as

$$C_{pq}(\rho) = \int\limits_{-\infty}^{\infty} f_p^*(x) \cdot f_q(x+\rho)dx. \tag{2.19}$$

In the above equation, ρ is called the *lag* and denotes the shift between the two functions f_p and f_q, f_p^* denotes the complex conjugate of f_p[1]. The ACovF of, e.g. f_p, is given by setting $q = p$ which leads to

$$C_{pp}(\rho) = C_p(\rho) = \int\limits_{-\infty}^{\infty} f_p^*(x) \cdot f_p(x+\rho)dx. \tag{2.20}$$

Henceforth, if only a single function $f(x)$ is considered, $C_p(\rho)$ will be further abbreviated to $C(\rho)$ and called the HHCF of $f(x)$.

To generate a point of the HHCF at lag ρ, $f(x)$ is first shifted by ρ to the left, thus becoming $f(x+\rho)$. Then, an integration of the product $f^*(x) \cdot f(x+\rho)$ is performed, which yields $C(\rho)$. This is illustrated in figure 2.12. The maximum of $C(\rho)$ is located at $\rho = 0$ and is equal to the variance σ^2 of $f(x)$. When applying equation 2.20 to to a surface profile $h(x)$, then σ is called the root mean square (RMS) roughness.

Discrete form

When analyzing AFM topography scans, one has to deal with a finite sample size consisting of discrete data points in an $M \times N$ matrix. Therefore, it is necessary to rewrite the equations presented so far in their discrete form. The function $f(x)$ or $f(x,y)$ will hence be denoted as $f(x_p)$ and $f(x_p, y_q)$ respectively. The indices of the arguments indicate the discrete nature of the sample. Furthermore, $p \in \{1,\,2,\,\ldots,\,M\}$ and $q \in \{1,\,2,\,\ldots,\,N\}$ with $M, N \in \mathbb{N}$.

---

[1] For a complex number $z = a + ib = Re^{i\phi}$, the complex conjugate is defined as $z^* = a - ib = Re^{-i\phi}$, so that $z \cdot z^* = a^2 + b^2 = R^2 = |z|^2$.

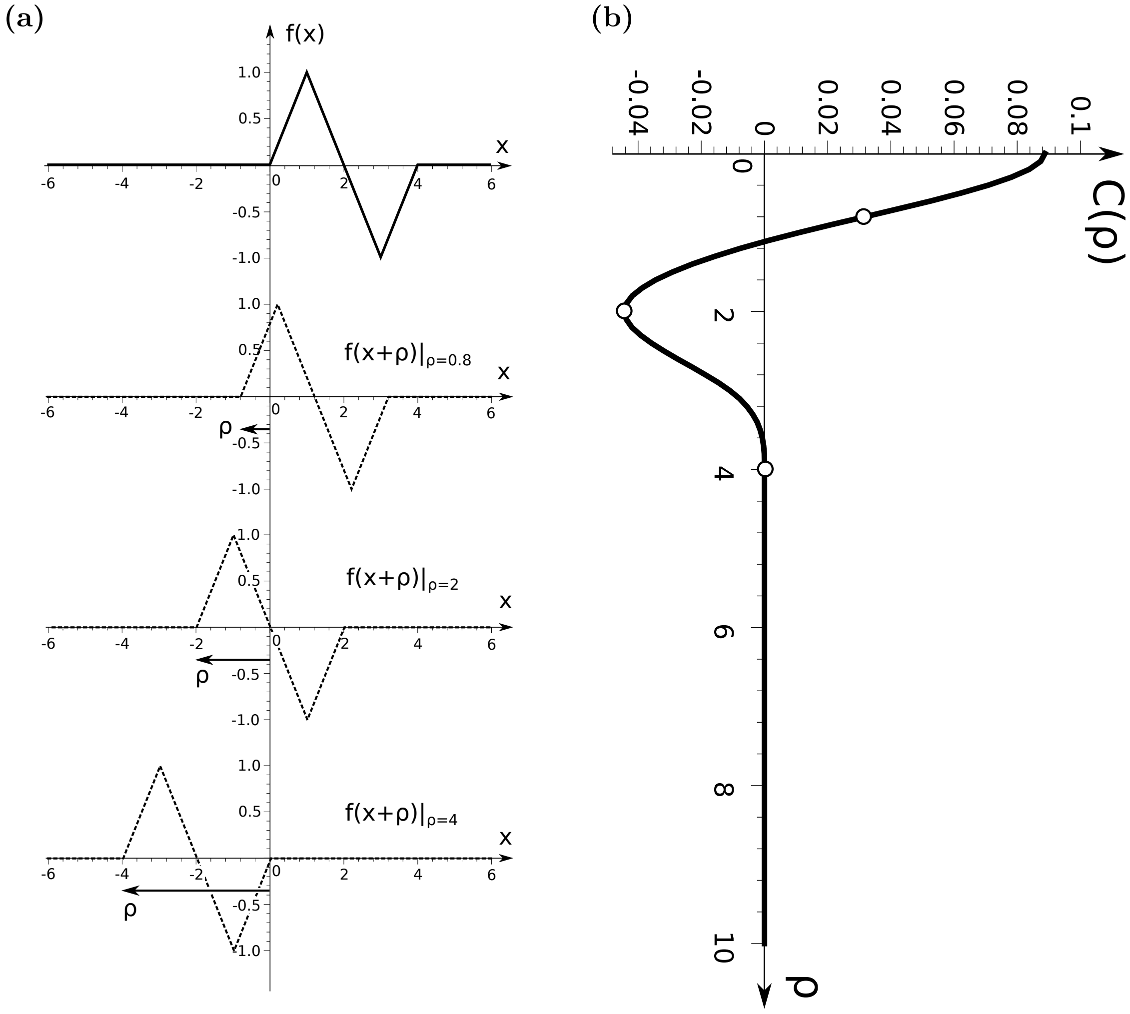

Figure 2.12.: The generation of the HHCF (see equation 2.20). In (a) the shift of the function $f(x)$ by ρ, $f(x+\rho)$, is illustrated for three values of ρ. The resulting HHCF is drawn in (b), where the circles indicate the respective lags in (a).

A discrete form of equation 2.20 in 2D representation would be

$$C(\rho_m, \rho_n) = \langle [f(x_p + \rho_m, y_q + \rho_n) - \langle f(x_p, y_q)\rangle][f(x_p, y_q) - \langle f(x_p, y_q)\rangle]\rangle, \tag{2.21}$$

$m \in \{1, 2, \ldots, M\}$ and $n \in \{1, 2, \ldots, N\}$ [53]. To simplify the notation of this equation, $f(x_p, y_q)$ is abbreviated as $f_{(p)(q)}$ and the sample mean $\langle f_{(p)(q)}\rangle$ as $\bar{f}$ with

$$\bar{f} = \frac{1}{MN} \sum_{p=1}^{M} \sum_{q=1}^{N} f_{(p)(q)}. \tag{2.22}$$

In equation 2.21 the lags ρ_m and ρ_n are also discrete values $\rho_m \in \{\rho_1, \rho_2, \ldots, \rho_M\}$ and $\rho_n \in \{\rho_1, \rho_2, \ldots, \rho_N\}$ and can be described as $\rho_m = x_{p+m} - x_p$ and $\rho_n = y_{q+n} - y_q$, respectively. Therefore, $f(x_p+\rho_m, y_q+\rho_n) = f(x_{p+m}, y_{q+n})$ and can be abbreviated to $f_{(p+m)(q+n)}$, which leads to

$$C_{(m)(n)} = \langle [f_{(p+m)(q+n)} - \bar{f}][f_{(p)(q)} - \bar{f}] \rangle \tag{2.23}$$

or, alternatively,

$$C_{(m)(n)} = \frac{1}{(M-m)(N-n)} \sum_{p=1}^{M-m} \sum_{q=1}^{N-n} [f_{(p+m)(q+n)} - \bar{f}][f_{(p)(q)} - \bar{f}]. \tag{2.24}$$

Note that $\bar{f}$ can be subtracted beforehand, as was assumed before. It is immediately obvious that when $m = n = 0$, $C_{(0)(0)} = \sigma^2$.

When dealing with isotropic surfaces, it will suffice to regard a 1D representation of equation 2.24 by either averaging circularly or calculating the HHCF per line and averaging then. Note that when dealing with AFM scans, the HHCF is usually calculated along the fast scan axis, when represented as a line average, which is

$$C_{(m)} = \frac{1}{N(M-m)} \sum_{q=1}^{N} \sum_{p=1}^{M-m} [f_{(p+m)(q)} - \bar{f}][f_{(p)(q)} - \bar{f}]. \tag{2.25}$$

When a general ACovF is regarded, two points of $f(x)$ with distance ρ can be considered correlated if $C(\rho)$ is significantly larger than zero. To statistically check for significance, the so called auto-correlation function (ACF) can be employed, which is given as

$$G(\rho) = \frac{C(\rho)}{\sigma^2} = \frac{C(\rho)}{C(0)}. \tag{2.26}$$

The maximum of this function is obviously $G(0) = 1$. If $f(x)$ is random, significant correlation can then be assumed if $G(\rho) > \pm 2/\sqrt{N}$, where N describes the number of independent observations [52].

Alternating terminology

In the literature, equations 2.20 and 2.21 are sometimes referred to as height difference function (HDF) [54] or as ACovF [55,56] instead. In these works, the term HHCF denotes the function

$$H_{(m)(n)} = \langle [f_{(p+m)(q+n)} - f_{(p)(q)}]^2 \rangle = 2\sigma^2[1 - G_{(m)(n)}], \tag{2.27}$$

with $G_{(m)(n)}$ being the discrete 2D ACF, analogous to equation 2.26. Usually, $H_{(m)(n)}$ is named HDF, according to its calculation of height differences. Furthermore, using HHCF for $C_{(m)(n)}$ underlines the function's statistical meaning and will thus be used in this work. Note that the HDF and HHCF provide the same information, as is obvious from equation 2.27.

Another separate naming convention was introduced by the developers of the SPM image analysis software Gwyddion [57]. In Gwyddion, the HHCF is named ACF, whereas the HDF is referred to as HHCF instead.

2.5.2. Power spectral density

The power spectral density (PSD) is a way to represent the complex-valued Fourier transform (FT) as a real-valued function. Both can be used to identify harmonic parts of a arbitrary function $f(x)$ by transforming it into its spectrum. Moreover, PSD contains essentially the same information as the HHCF and provides an additional way to calculate the HHCF. Unfortunately, PSD and FT are defined differently in different fields. Therefore, this subsection is solely dedicated to define FT and PSD for the use in this work and give alternate descriptions of equations 2.19 and 2.20 as well as the discrete HHCF (equation 2.23). Again, the analytical representations will be covered first.

Analytical form

Since the PSD is calculated from the FT, the FT is defined first. Assuming a function $f(x)$ with mean $\langle f(x)\rangle = 0$, the one-dimensional (1D) Fourier transform of $f(x)$ is given by

$$F(f)(k_x) = F(k_x) = \int\limits_{-\infty}^{\infty} f(x) \cdot e^{-ik_x x} dx. \tag{2.28}$$

In equation 2.28, $i = \sqrt{-1}$ is the imaginary unit, leading to a complex $F(k_x)$ in general. The inverse transformation is

$$F^{-1}(F(k_x))(x) = f(x) = \frac{1}{2\pi} \int\limits_{-\infty}^{\infty} F(k_x) \cdot e^{+ik_x x} dk_x. \tag{2.29}$$

Note that the assumption $\langle f(x)\rangle = 0$ is not necessary, however, it will simplify $F(k_x)$. Assume $g(x) = f(x) + \bar{g}$ with $\bar{g} = \langle g(x)\rangle \neq 0$, then obviously

$$F(g)(k_x) = \int\limits_{-\infty}^{\infty} g(x) \cdot e^{-ik_x x} dx = \int\limits_{-\infty}^{\infty} f(x) \cdot e^{-ik_x x} dx + \int\limits_{-\infty}^{\infty} \bar{g} \cdot e^{-ik_x x} dx. \tag{2.30}$$

And since $\int_{-\infty}^{\infty} \bar{g} \cdot e^{-ik_x x} dx = 2\pi\bar{g}\delta(k_x)$ [58], with $\delta(k_x)$ denoting the delta distribution, equation 2.30 can be shortened to

$$F(g)(k_x) = F(f)(x) + 2\pi\bar{g}\delta(k_x). \tag{2.31}$$

This demonstrates that for functions $g(x)$ with non-zero mean, a delta peak at $k_x = 0$ is introduced. When $\bar{g}$ is subtracted from $g(x)$, the FT is simplified and easier to visualize, since one does not have to deal with plotting the value $F(x) = \infty$, which is especially problematic in numerical calculations. Also note that the nature of the function $g(x)$ is not changed when $\bar{g}$ is subtracted beforehand.

Using equation 2.28, the PSD shall be defined as

$$P(k_x) = F^*(k_x)F(k_x) = |F(k_x)|^2. \tag{2.32}$$

Per definition, the PSD is – in contrast to the FT – a real valued function. The PSD and the FT are often used to visualize and quantify orientation in an AFM image, as well as identifying periodic or quasi-periodic structures [53]. Another use of PSD and FT is the calculation of CCovF and HHCF (ACovF). Taking the FT of the CCovF yields

$$\begin{aligned}
F(C_{pq})(k_x) &= \int\limits_{-\infty}^{\infty} C_{pq}(\rho) \cdot e^{-ik_x\rho} d\rho = \int\limits_{-\infty}^{\infty}\int\limits_{-\infty}^{\infty} f_p^*(x) \cdot f_q(x+\rho) dx \cdot e^{-ik_x\rho} d\rho = \\
&= \int\limits_{-\infty}^{\infty} f_p^*(x) \cdot \left[\int\limits_{-\infty}^{\infty} f_q(x+\rho) \cdot e^{-ik_x\rho} d\rho \right] dx = \\
&= \int\limits_{-\infty}^{\infty} f_p^*(x) \cdot F(f_q)(k_x) \cdot e^{ik_x x} dx = \\
&= F^*(f_p)(k_x) \cdot F(f_q)(k_x). \qquad (2.33)
\end{aligned}$$

In equation 2.33 the fact that $F(f(x-a))(k_x) = F(f(x))(k_x)e^{-ik_x a}$ is used [58,59]. Note also that $\int_{-\infty}^{\infty} f^*(x)e^{ik_x x} = F^*(k_x)$ is used[2]. For the HHCF (or ACovF), equation 2.33 results in

$$F(C)(k_x) = F^*(k_x)F(k_x) = |F(k_x)|^2 = P(k_x), \qquad (2.34)$$

which means that the HHCF can be calculated by performing the inverse Fourier transform (iFT) of the PSD. The advantage of this relation for practical calculations will be discussed below.

Since AFM scans yield a two-dimensional (2D) height map, the 2D FT is frequently applied:

$$F(f)(k_x, k_y) = F(k_x, k_y) = \int\limits_{-\infty}^{\infty}\int\limits_{-\infty}^{\infty} f(x,y) \cdot e^{-i(k_x x + k_y y)} dx\, dy. \qquad (2.35)$$

2D PSD and 2D HHCF are calculated by using equation 2.35 in equations 2.32 and 2.34 respectively.

Discrete form

The discrete Fourier transform (DFT) of $f_{(p)(q)}$ in 2D form shall be defined as

$$F(f_{(p)(q)})(k_m, k_n) = F_{(m)(n)} = \frac{1}{MN} \sum_{p=1}^{M} \sum_{q=1}^{N} f_{(p)(q)} \cdot e^{-i(k_m x_p + k_n y_q)}. \qquad (2.36)$$

The variables in the exponent are

---

[2] $z = Re^{i\phi}$, $z^* = Re^{-i\phi} \Rightarrow S = Re^{i\phi}e^{-ik} = Re^{i(\phi-k)}$ and $S' = Re^{-i\phi}e^{ik} = Re^{-i(\phi-k)} = S^*$

$$\begin{aligned} x_p &= p\Delta x = p\frac{L_x}{M}, \\ y_q &= q\Delta y = q\frac{L_y}{N}, \\ k_m &= m\Delta k_m = m\frac{2\pi}{L_x}, \\ k_n &= n\Delta k_m = n\frac{2\pi}{L_y} \end{aligned} \tag{2.37}$$

L_x and L_y denote the physical lengths of the sample in x- and y-direction. Using the relations 2.37 it can be easily seen that

$$\begin{aligned} k_m x_p &= m\frac{2\pi}{L_x}p\frac{L_x}{M} = \frac{2\pi mp}{M}, \\ k_n y_q &= \frac{2\pi nq}{N}. \end{aligned} \tag{2.38}$$

Now equation 2.36 can be rewritten as

$$F_{(m)(n)} = \frac{1}{MN}\sum_{p=1}^{M}\sum_{q=1}^{N} f_{(p)(q)} \cdot e^{-\frac{2\pi i}{MN}(Nmp+Mnq)}, \tag{2.39}$$

and the inverse transformation is

$$F^{-1}_{(p)(q)} = \sum_{p=1}^{M}\sum_{q=1}^{N} F_{(m)(n)} \cdot e^{\frac{2\pi i}{MN}(Nmp+Mnq)}. \tag{2.40}$$

Both equations 2.39 and 2.40 have the advantage of being independent from the physical size of the sample. The discrete PSD is defined accordingly to equation 2.32

$$P_{(m)(n)} = |F_{(m)(n)}|^2 \tag{2.41}$$

and yields the 2D HHCF as

$$C_{(p)(q)} = F^{-1}_{(p)(q)}(P_{(m)(n)}). \tag{2.42}$$

The advantage of equation 2.42 becomes apparent, when the fast Fourier transform (FFT) [60] is used instead of equation 2.39. To calculate a DFT according to equation 2.39, N^2M^2 steps are needed and to compute the HHCF as given in equation 2.24 $\frac{1}{4}(N^2 - N)(M^2 - M)$ steps would be necessary. In contrast, the number of steps when using an FFT algorithm is of the order $\mathcal{O}(NM \cdot \log NM)$, which implies that it is still much faster to compute two FFTs[3] instead of calculating the HHCF according to equation 2.24 one time[4].

---

[3] One DFT to calculate the PSD and an iDFT to get the HHCF.

[4] Note that the calculation of the DFT according to equation 2.39 of data with size 1024 × 1024 can take several hours even on a modern computer.

The classical FFT-algorithm is limited in datasizes of the form $2^n \times 2^m$, $(n, m) \in \mathbb{N}$ [60]. A modern implementation of FFT-algorithms, the FFTW library, has overcome this limitation and computes DFTs in $\mathcal{O}(N \cdot \log N)$ time, for any datasize even when N is prime [61].

2.5.3. Self-affine random rough surfaces with a cut-off

Many surfaces of technical and academic interest can be described as being random rough and self-affine with a finite cut-off length. This classification originates from the surface's fractal scaling behavior, which follows

$$\sigma \propto L^{\alpha} \tag{2.43}$$

until a certain cut-off length ξ_c with σ denoting the RMS roughness, L the lateral observation length, and $0 \leq \alpha \leq 1$ the roughness exponent [62–64]. For a surface to be self-affine – in contrast to self-similar – σ has to be of a different order of magnitude than L. When $L > \xi_c$, then σ becomes constant and independent of L. This scaling behavior is illustrated in figure 2.13.

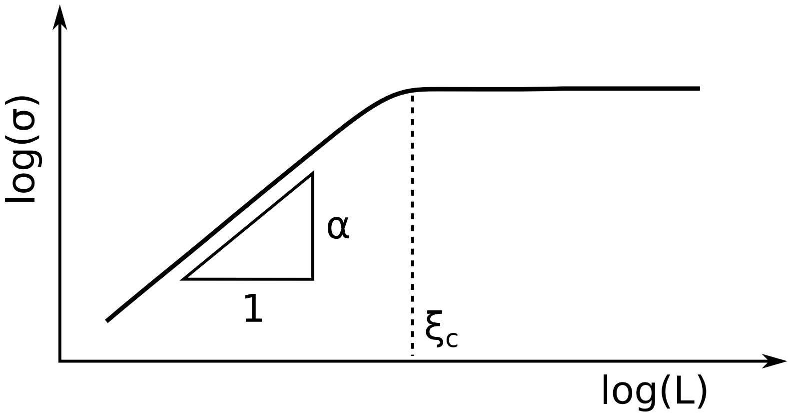

Figure 2.13.: The scaling behavior of self-affine random rough surfaces with a cut-off.

The roughness exponent α in equation 2.43 is sometimes also named *Hurst parameter* [65]. It quantifies how the surface roughness is changing with the length scale under consideration [66]. α is linked to the fractal dimension D_f by

$$D_f = D_t + 1 - \alpha, \tag{2.44}$$

where D_t represents the topological dimension [62].[5] Note that if $\alpha = 1$, the fractal and topological dimensions coincide and the surface is not fractal. On the other hand, if $\alpha = 0$, the surface would have a dimension of $D_f = D_t + 1$ and according to equation 2.43 $\sigma = const.$ at all length scales.

---

[5] $D_t = 1$ for line profiles, $D_t = 2$ for 2D height maps

One could in principle characterize a surface's topography comprehensively using σ, ξ_c, and α by recording AFM images with varying sizes, instead of using σ alone. The drawback is that such an endeavor would be tedious and time consuming. It is, however, possible to extract σ, α, and a measure for ξ_c from a single AFM scan. This is performed by calculating the HHCF of a surface according to, e.g., equation 2.23 and fit $C_{(m)(n)}$ using the function [67]

$$C(\boldsymbol{\rho}) = \sigma^2 e^{-\left(\frac{|\boldsymbol{\rho}|}{\xi}\right)^{2\alpha}}. \tag{2.45}$$

Here, $\boldsymbol{\rho} = [\rho_x, \rho_y]'$ is the vector of the lags in x and y directions. Since only isotropic surfaces are considered in this work, a 1D HHCF is calculated by averaging the HHCF of each line or performing a radial average. Equation 2.45 can then be simplified to

$$C(|\boldsymbol{\rho}|) = C(\rho). \tag{2.46}$$

In equation 2.45, ξ describes a lateral correlation length and is different from the cut-off length ξ_c. The lateral correlation is a measure for lateral roughness fluctuations or – in other words – denotes the maximum distance for which two points are still considered to be correlated. In figure 2.14, the physical meaning of ξ is illustrated by two line profiles which were generated using the convolution method [55]. It is evident that the profile in figure 2.14b features more hill-like structures as the one presented in figure 2.14a at the same lateral scale. To relate the lateral correlation length to the cut-off length, it should be noted that $\xi_c \gg \xi$. This makes sense, since σ will only be independent of L, when the topographical structures defined by ξ are small compared to the observing length. Therefore, the larger ξ, the larger ξ_c becomes and $\xi \propto \xi_c$ [68].

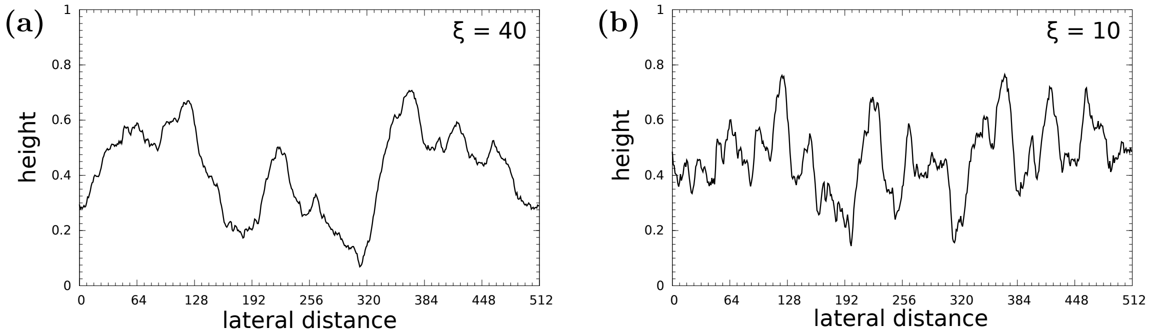

Figure 2.14.: Simulated surface profiles to illustrate the lateral correlation length ξ. In (a), ξ is four times larger than in (b). σ and α are the same in both graphs.

The other parameters, σ and α, have the same meaning as discussed before. The physical meaning of α can be considered as the *jaggedness* of the surface under consideration. It is obvious why this terminology was chosen when comparing the two simulated surface profiles shown in figure 2.15. While the profile in figure 2.15a appears perfectly smooth, the profile in figure 2.15b is jagged and one would consider it more rough than the one in figure 2.15a.

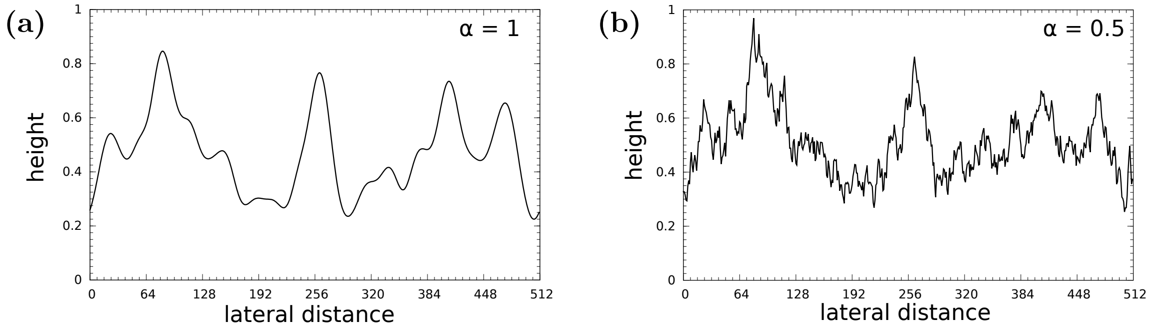

Figure 2.15.: Simulated surface profiles to illustrate the Hurst parameter α. In (a), $\alpha = 1.0$, whereas in (b) $\alpha = 0.5$. σ and ξ are the same in both graphs.

On a side note, equation 2.45 has the drawback that it becomes invalid for $\alpha \to 0$. Therefore, a more complex function – the K-correlation model [68] – was proposed, which can be used in these cases [69–72].

3. Experimental

3.1. AFM Instrumentation

The atomic force microscope used for all experiments in this work was an Asylum Research MFP-3D (Santa Barbara, CA), equipped with a planar closed loop sample scanner. Its maximum x-y scan size is $90\,\mu\text{m} \times 90\,\mu\text{m}$, and the z-range is $15\,\mu\text{m}$. In this AFM system, the cantilever is tilted by 11° – which is the case for most commercial AFMs.

3.1.1. Probes

Basically, two types of AFM probes were used: one for imaging and another for AFM-NI. Probes for imaging should provide a low tip apex radius and a low opening angle to gain a high resolution. On the other hand, probes for AFM-NI should feature a tip geometry that is easy to characterize – meaning a high opening angle (see subsection 3.2.1) – and the cantilever should be stiff enough to apply a sufficiently high load. It is further beneficial for the tip to be hard and stiff, so that it will not deform during indentation or is even damaged. For soft materials, such as cellulose, this is easily achieved, since commonly used tip materials (silicon, silicon nitride, diamond, etc.) are much harder and stiffer than cellulose.

Imaging

For imaging, Olympus AC160TS-R3 and AC240TS-R3 silicon probes (Tokyo, Japan) with aluminum reflex coating at the back side of the cantilever were used. Both feature a tetrahedral tip at the very end of the cantilever with a front angle of 0°, a back angle of 35°, and side angles of 15° (see figure 3.1a). The tip apex radius is typically 7 nm. AC160TS-R3 probes feature an average spring constant of $26\,\frac{\text{N}}{\text{m}}$, whereas AC240TS-R3 probes have a spring constant of $2\,\frac{\text{N}}{\text{m}}$. Average resonance frequencies are 300 kHz and 70 kHz, respectively. The cantilevers' dimensions are listed in table 3.1.

AFM-NI

For AFM-NI, ND-DTIRS full diamond probes with aluminum reflex coating (Advanced Diamond Technologies, Romeoville, IL) were used at first. Their three-sided pyramidal tips have a front and back angle of 65° and side angles of 35°. At the apex, the radius of curvature is 15 nm in average and at least smaller than 50 nm. To get exact results for

Table 3.1.: Cantilever geometry of the Olympus AC160TS-R3 and AC240TS-R3 silicon probes.

designation	length / μm	width / μm	thickness / μm	shape
AC160TS-R3	160	40	3.7	rectangular
AC240TS-R3	240	40	3.3	rectangular

the applied forces, the cantilevers' spring constants were determined using the thermal sweep method [73] (see below) and were found to be between 50 $\frac{\mathrm{N}}{\mathrm{m}}$ and 65 $\frac{\mathrm{N}}{\mathrm{m}}$.

After the first AFM-NI results were obtained on pulp fibers and cellulose films, the ND-DTIRS probe line was discontinued by the manufacturer. As a replacement, ND-DYIRS probes from the same manufacturer were introduced. These are also full-diamond probes with aluminum reflex side coating, but feature a regular, four-sided pyramid as a tip. The front, back and side angles are all 45° (see figure 3.1b) and the apex radius is also 15 nm in average and less than 50 nm. Spring constants were determined to be between 45 $\frac{\mathrm{N}}{\mathrm{m}}$ and 60 $\frac{\mathrm{N}}{\mathrm{m}}$. The cantilever dimensions for both probe types are listed in table 3.2.

Table 3.2.: Cantilever geometry of the ND-DTIRS and ND-DYIRS full diamond probes.

designation	length / μm	width / μm	thickness / μm	shape
ND-DTIRS	120	33	3	rectangular
ND-DYIRS	135	33	3	rectangular

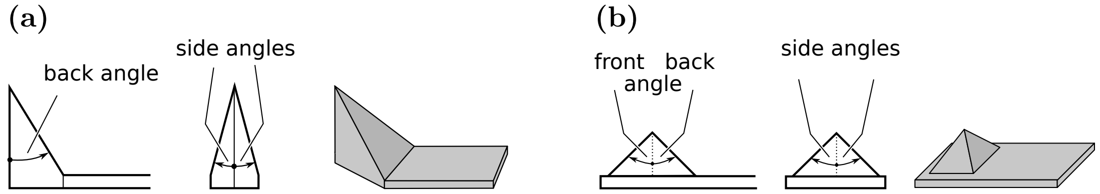

Figure 3.1.: Sketch of (a) the tips used for imaging and (b) the ND-DYIRS tips used for AFM-NI.

Calibration of cantilever spring constants

In order to measure forces with an AFM, the cantilever's spring constant k as well as the optical lever sensitivity S_{OLS} have to be determined precisely. The sensitivity is the ratio between the signal at the diode V_{PD} and the cantilever's actual deflection z_d

$$V_{PD} = S_{OLS} \cdot z_d. \tag{3.1}$$

It is calibrated by pressing the cantilever on a hard substrate and recording V_{PD} as a function of the piezo movement z. If the substrate does not deform, this is a straight line and, obviously, $z = z_d$. Plotting V_{PD} versus z_d and measuring the slope yields directly S_{OLS}. Note that this method implies a calibrated z-piezo or an active z-sensor, otherwise the deflection z_d cannot be determined. In this work, a silicon wafer with native oxide was used as the hard substrate. To verify if a silicon wafer is appropriate, the calibration of S_{OLS} has been cross-checked on a diamond coated fused silica substrate where no difference was detectable. Note that in the Asylum Research software, the inverse optical lever sensitivity $S_{iOLS} = S_{OLS}^{-1}$ is calibrated.

The spring constant can be determined after S_{OLS} is known using the thermal sweep method [73]. This procedure is a built-in function of the Asylum Research MFP-3D's software.

3.1.2. Controlled relative humidity

To control relative humidity inside the fluid cell, the setup presented schematically in figure 3.2 is employed. A flow of dry nitrogen is divided into two lines with adjustable flow rates. One line is kept dry, whereas the other one is lead through a bubbler where the nitrogen is saturated with water ($\varphi_r = 1$). Since the bubbler is – due to the fact that water is evaporated – most likely the coldest spot in the system, φ_r of the humid line will decrease below 1 outside the bubbler. Heating the bubbler by two 3 W PTC heating foils (thermo Technologies, Germany) above room temperature, ensures that φ_r cannot drop below its initial value. This is a direct consequence of equations 2.17 and 2.18.

After the bubbler, the dry and saturated nitrogen lines are merged together, leading to a mixture with a water content according to the flow rates of the two lines. Before the fluid cell, a buffer volume is located which absorbs fluctuations in relative humidity. This is necessary, since the fluid cell has a volume of only 10 mℓ. Since temperatures of up to 32 ℃ are observed in the fluid cell, the buffer as well as the tubes between bubbler and fluid cell are also heated. This, however, is realized with a HST III heating wire (Carl Roth, Germany), operated at a power of ≈ 50 W. Separate heating circuits for buffer and bubbler result in a high flexibility in the temperature profile and allow to reach very high relative humidities in the fluid cell. For example, without heating the buffer, the maximum φ_r was ≈ 0.8, whereas by heating it, a relative humidity of up to $\varphi_r = 0.95$ can be generated inside the fluid cell. Note that at $\varphi_r = 0.95$ a temperature decrease from 30 ℃ to 29.11 ℃ results already in condensation. Condensation inside the fluid cell can be a problem, since the sample will then be subject to bulk water and not only humid air. Also, the humidity sensor might be covered with water droplets, causing short-circuits, false readings, and – in the worst case – permanent damage to the sensor.

For the bubbler as well as the buffer, 500 mℓ DURAN glass gas-washing bottles (Carl

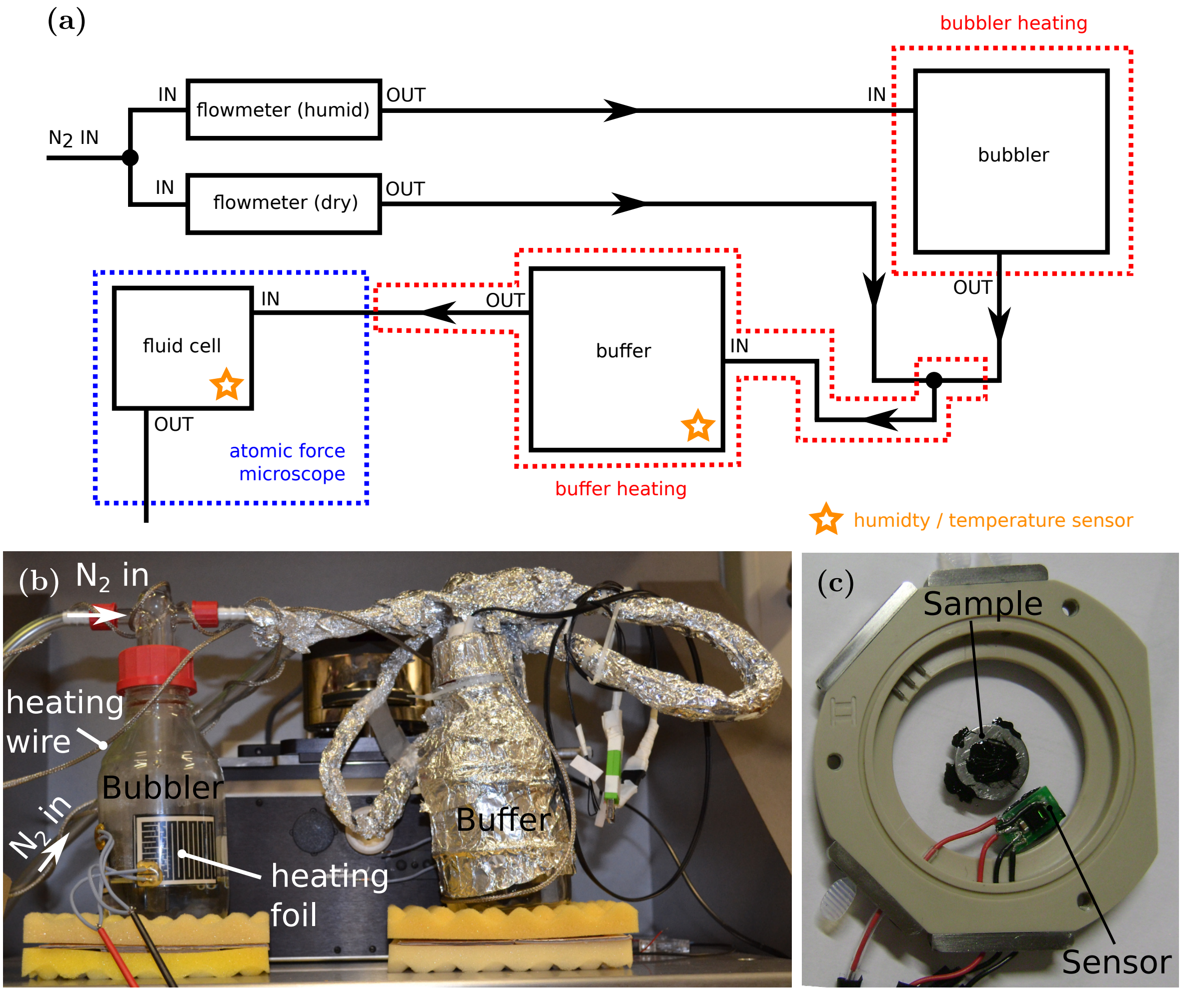

Figure 3.2.: Setup to control relative humidity within the AFM's fluid cell as (a) a schematical representation, (b) a photograph of the actual setup, and (c) the sample mounted in the fluid cell, including the humidity sensor.

Roth, Germany) were used. The connection tubes are transparent Rotilabo PVC tubes with a diameter of 10 mm (Carl Roth, Germany). The flow meters to regulate and monitor the nitrogen are acrylic Omega FL 4213 rotameters (Stamford, CT). Sensirion SHT 21 humidity sensors (Staefa, Switzerland) are positioned inside the fluid cell as well as the buffer. The sensors record the relative humidity with a tolerance of ± 0.03 in the φ_r interval $[0.2, 0.8]$ which increases linearly to 0.05 until $\varphi_r = 0.0$ and $\varphi_r = 1.0$. Additionally, the temperature is recorded with a maximum tolerance of 0.4 ℃ between 5 ℃ and 60 ℃. During the course of an experiment, the SHT 21 sensor in the fluid cell is constantly logging data, whereas the sensor in the buffer, is used only for troubleshooting purposes. Note that the thickness of the printed circuit board on which the sensor is mounted had to be reduced by approximately 50 %, so it would fit into the fluid cell.

3.1.3. Fluid cell

For AFM measurements in water as well as experiments under controlled relative humidity, an Asylum Research fluid cell was employed. The setup to control relative humidity requires in- and outlets for nitrogen and connections to the humidity sensor. Therefore the fluid cell body drawn in figure 3.3a was used in a closed configuration, in order to establish a stable environment. The cell's interior was sealed completely (figure 3.3c), allowing only the passing of the controlled nitrogen flow through the open ports.

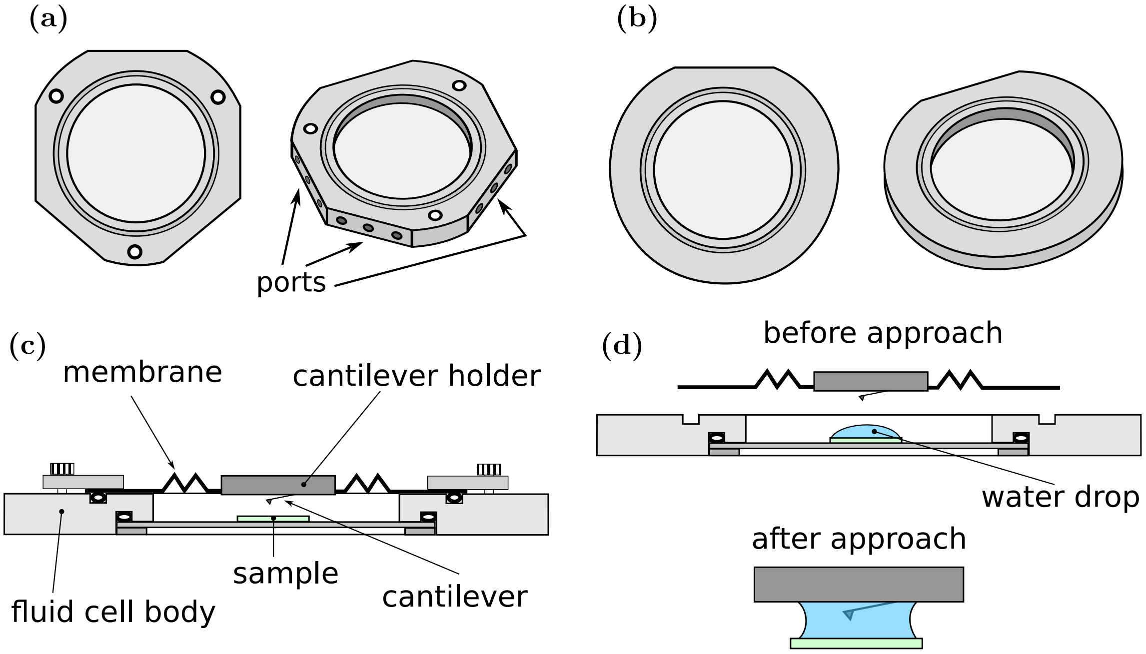

Figure 3.3.: Schematic of (a) the fluid cell body with connection ports and (b) the body without ports. Both bodies can be operated in (c) the closed and (d) the open configuration.

Samples completely submerged in water were investigated using the portless fluid cell body, presented in figure 3.3b. The reason for that is that the lack of ports and any additional openings reduces the risk of water leaking from the cell. To permit a large range of movement and to allow easy access to the sample, the open configuration of the fluid cell was chosen for experiments in water. Only a drop of water with a diameter of about 10 mm was added to the sample. After approaching with the cantilever, a water meniscus between the sample and the cantilever holder will form and produce a stable environment (see figure 3.3d).

3.2. AFM based nanoindentation

AFM based nanoindentation is carried out using the Asylum Research MFP-3D AFM. First, the surface is scanned in tapping mode to locate sufficiently flat regions. Then, P - z plots were recorded in contact mode at a desired position. For all measurements, the load schedule featured a hold time at maximum load and a second hold towards the end of the unloading segment, as is presented in figure 2.8. The parameters were $P_{max} = 10\,\mu\text{N}$, $|\dot{P}| = 10\,\frac{\mu\text{N}}{\text{s}}$, $t_{h,c} = 10\,\text{s}$, and $t_{h,t} = 30\,\text{s}$.

3.2.1. Determination of the area function

The area function $A(z)$ of an indenter describes the projected area at a certain distance z from the tip apex. $A(z)$ is an essential input parameter for calculating hardness H and reduced modulus E_r correctly, as is obvious from equations 2.4 and 2.7, respectively. In classical NI, this function is usually calibrated by indenting into a material with varying indentation depths [36]. In AFM-NI, however, a direct imaging of the indenter's geometry is easily achieved by scanning the tip across a grid with sharp spikes, a so-called tip characterizer. If the opening angle of the spikes is less than the indenter's opening angle, the indenter is imaged, as is drawn schematically in figure 3.4. This is commonly known as *tip-sample dilation* [74] and is sometimes misleadingly called *convolution*.

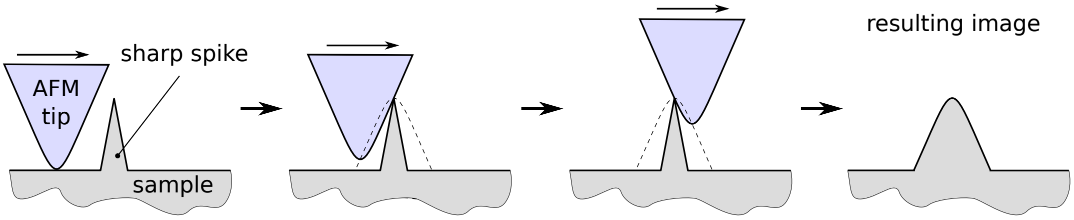

Figure 3.4.: The principle of tip-sample dilation. If the opening angle of the sharp spike is lower than the one of the tip, the resulting image will actually represent the tip.

To image the tip, the commercially available TGT01 calibration grid (NT-MDT, Moscow, Russia) was employed. On this grid, spikes with an opening angle of 30° and a tip radius of 10 nm are arranged periodically. Scanning this grid yields already good representations of the indenter. To improve the result even more, the obtained image is *eroded* with the modeled spike geometry (24-sided pyramid with an opening angle of 30° and an apex radius of 10 nm) using Gwyddion's built in functions. Erosion, in this case, denotes the inverse operation of dilation and is similarly miscalled *deconvolution*. Now, the area function is calculated by intersecting a horizontal plane with the tip geometry at any distance z from the apex (see figure 3.5a) and counting the pixels within the intersection. Since the physical dimensions of one pixel are known, $A(z)$ is the direct result and displayed in figure 3.5b. This procedure will henceforth be called the *dilation method*, according to the principle of which the tip's geometry is recorded.

A script for Gwyddion was written to extract the area function from the eroded AFM image and is presented in listing A.1 in appendix A.

In the remaining part of this subsection, the area function of an ideal pyramid is derived and compared to experimentally observed data. The purpose is to find a model that can be used to reliably fit the area function in an automated evaluation procedure.

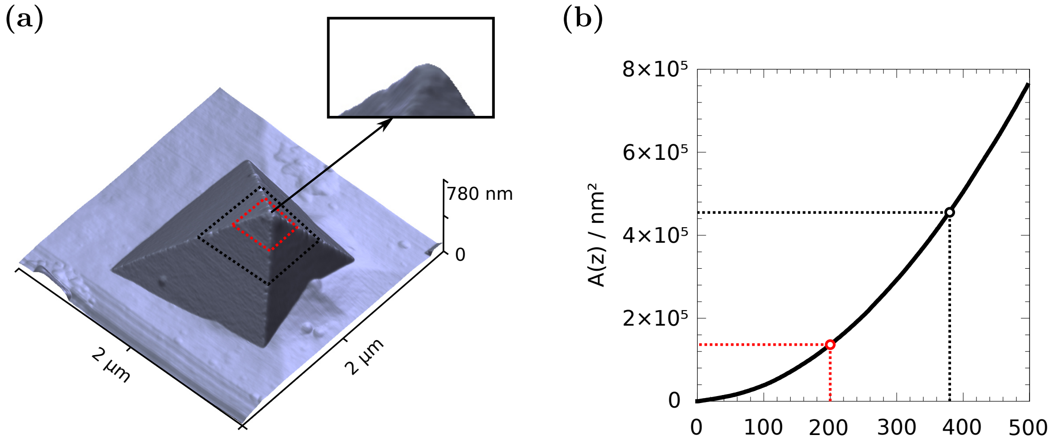

Figure 3.5.: (a) A 3D representation of the 4-sided pyramid tip (ND-DYIRS) and (b) its corresponding area function. The areas represented by quadrilaterals in (a) correspond to the circles with the respective color in (b). A finite tip apex is emphasized by the inset in (a).

Area function of a tilted ideal four-sided pyramid

By assuming that the tip is an ideal, regular four-sided pyramid with a square base, a half opening angle β and tilted by the angle γ, its area function can be calculated analytically. A sketch of such a tip at the end of a cantilever is presented in figure 3.6a. Due to the tilt, the tip becomes asymmetric (with respect to the surface) with a front opening angle of $\beta+\gamma$ and a back opening angle of $\beta-\gamma$. The area is then a trapezoid, with side lengths c, d and height e, as is drawn in figure 3.6b. Dividing the tip's side view into two regions which form right-angled triangles with the adjacent leg z. e is then equal to the sum $e = a + b$, with a, b being the respective opposite legs (see figure 3.6b). Then,

$$\begin{aligned} a &= z\tan(\beta+\gamma), \\ b &= z\tan(\beta-\gamma), \\ e &= a+b = z\left[\tan(\beta+\gamma)+\tan(\beta-\gamma)\right]. \end{aligned} \tag{3.2}$$

To obtain the side lengths c and d, one can consider them as part of squares with respective side lengths, when $\gamma = 0°$ and $z_i = s_i\cos(\beta)$, $i \in \{1,2\}$. In this case, the front, back, and side angles are all β and

$$\begin{aligned} c &= 2s_1 \sin(\beta), \\ d &= 2s_2 \sin(\beta). \end{aligned} \tag{3.3}$$

By using

$$\begin{aligned} s_1 &= \frac{z}{\cos(\beta+\gamma)}, \\ s_2 &= \frac{z}{\cos(\beta-\gamma)}, \end{aligned} \tag{3.4}$$

equations 3.3 read

$$\begin{aligned} c &= \frac{2z\sin\beta}{\cos(\beta+\gamma)}, \\ d &= \frac{2z\sin\beta}{\cos(\beta-\gamma)}. \end{aligned} \tag{3.5}$$

Then, since the area A of the trapezoid is obviously $A = \frac{1}{2}e(c+d)$ (right side of figure 3.6b), the area function is

$$A(z) = z^2 \left[\tan(\beta+\gamma) + \tan(\beta-\gamma)\right] \sin(\beta) \left[\frac{1}{\cos(\beta+\gamma)} + \frac{1}{\cos(\beta-\gamma)}\right]. \tag{3.6}$$

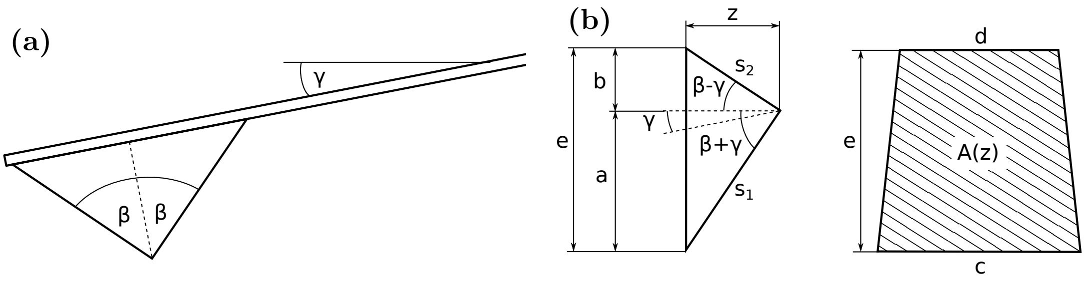

Figure 3.6.: A cantilever with a pyramidal tip. (a) The cantilever is tilted by γ in the AFM. (b) Geometry of a tilted pyramidal tip.

Evaluating equation 3.6 for $\beta = 45°$ and $\gamma = 11°$ – values specified by the manufacturers of the tip and the AFM – yields

$$A(z) = 4.5675z^2. \tag{3.7}$$

Here, it was assumed that γ, does not depend on the cantilever's deflection z_d. This is justified when the cantilever length $l \gg z_d$. In this work, the maximum load $P_{max} = 10\,\mu\mathrm{N}$ resulted in a deflection of $z_d \approx 200\,\mathrm{nm}$, by assuming a spring constant of $k \approx 50\,\frac{\mathrm{N}}{\mathrm{m}}$. For a cantilever length l of $135\,\mu\mathrm{m}$, it is true that $l \gg z_d$ and the deflection would change γ by approximately 0.1°. Thus, it is save to assume that γ is a constant.

Area function of a tilted pyramid obtained by the dilation method

According to equation 3.7, the area function is a parabola of the form $A(z) = C_2^{(t)} z^2$, with the superscript (t) referring to a theoretically obtained value. However, determining $A(z)$ of ND-DYIRS tips experimentally, using the dilation method, a function that is best fitted by the model

$$A(z) = C_1^{(e)} z + C_2^{(e)} z^2 + C_3^{(e)} z^3 \tag{3.8}$$

is obtained, with (e) marking experimentally obtained parameters. By evaluating 53 area functions of all together 14 tips of the same type, the coefficients amount to $C_1^{(e)} = (248 \pm 98)\,\text{nm}$, $C_2^{(e)} = 2.49 \pm 0.36$, and $C_3^{(e)} = (2.64 \times 10^{-4} \pm 1.02 \times 10^{-3})\,\text{nm}^{-1}$. The cubic term can be viewed as a correction for non-ideal tip geometries and is not discussed further. Nonetheless, theory and experiment do not coincide with each other. First, the theory predicts only a quadratic function, whereas in practice an additional linear term is observed. And secondly, the coefficients for the parabolic part of the theoretical and experimental area functions $C_2^{(t)}$ and $C_2^{(e)}$, respectively, differ strongly from each other.

A likely explanation for the linear term is that the pyramid is not perfect and has characteristics of a paraboloid of rotation. It is likely to be an artifact from the manufacturing process. A paraboloid of rotation has an area function of the form $A(z) = C_1^{(para)} z$ and would thus explain the linear term.

The difference in $C_2^{(t)}$ and $C_2^{(e)}$ arises from the fact that the front, back, and side angles of the pyramidal tip are not 45° as is specified. Instead, it was found that $\beta = 37.2° \pm 0.6°$. The tilt angle γ could be obtained from the tip asymmetry (compare figure 3.6b) and amounted to $\gamma = 10.8° \pm 0.5°$, which is as specified. Note that the tips were all characterized with a closed-loop scan and a calibrated z-piezo. Hence, the determined angles are expected to be correct. By using the experimentally determined β, equation 3.6 yields the coefficient $C_2^{(t)} = 2.55$, a value very close to $C_2^{(e)} = 2.49 \pm 0.36$.

In figure 3.7a, a comparison between the area functions of pyramids with 45°, 37.2°, and equation 3.8 is presented. While the measured angle of 37.2° used in equation 3.6 is closer to the experimentally obtained $A(z)$, it still deviates significantly. The model, presented in equation 3.8, fits the area function perfectly for indentation depths larger than 100 nm. However, for indentation depths lower than 100 nm, the fit deviates significantly from the experiment. To quantify this deviation, the relative fit error $e_{r,fit}$ is calculated by

$$e_{r,fit} = \frac{A_{exp} - A_{fit}}{A_{exp}} \times 100\,\%. \tag{3.9}$$

A_{exp} and A_{fit} from equation 3.9, denote the experimentally obtained and fitted area function, respectively. It is observed that an error of up to 20 % is introduced when the indentation depth is between 40 nm and 100 nm. The relative error of the fit displayed in figure 3.7a is given in figure 3.7b, where an error of approximately 13 % is present at an indentation depth of 40 nm. These deviations at low indentation depths are due to the fact that the tip apex is not pyramidal but usually rounded, as is shown in the inset of figure 3.5a.

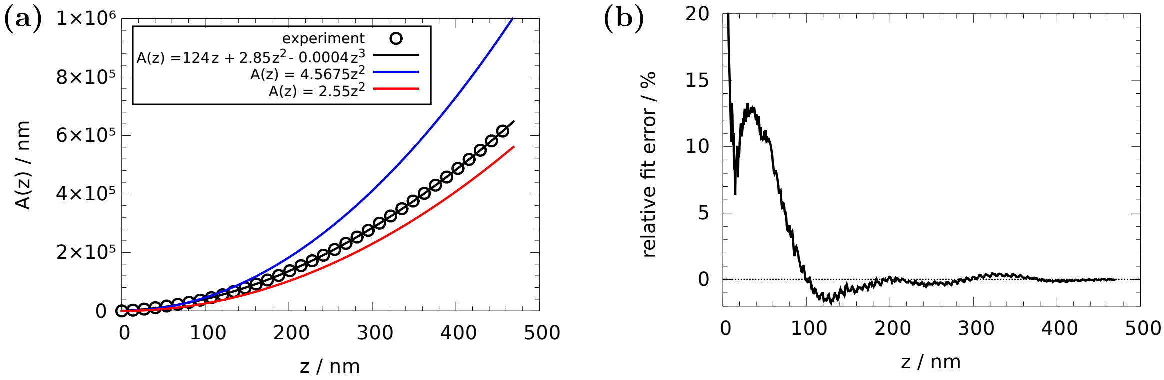

Figure 3.7.: (a) Comparison of theoretically obtained area functions (blue and red), a fit according to equation 3.8 (black line), and the experimentally obtained value (black circles). (b) Relative error of the fit according to equation 3.9.

To counter the effects of a finite tip apex, the first 100 nm are fitted separately by equation 3.8. This ensures that the fit error is kept low, even for indentation depths of only 30 nm. Large errors below that are of no concern, since the minimal indentation depth observed was around 40 nm. In figure 3.8a, a fit of the first 100 nm is compared to a fit of the whole data set. In conjunction with the respective fit errors presented in figure 3.8b, it is made clear that a separate fit of the first 100 nm yields improved results.

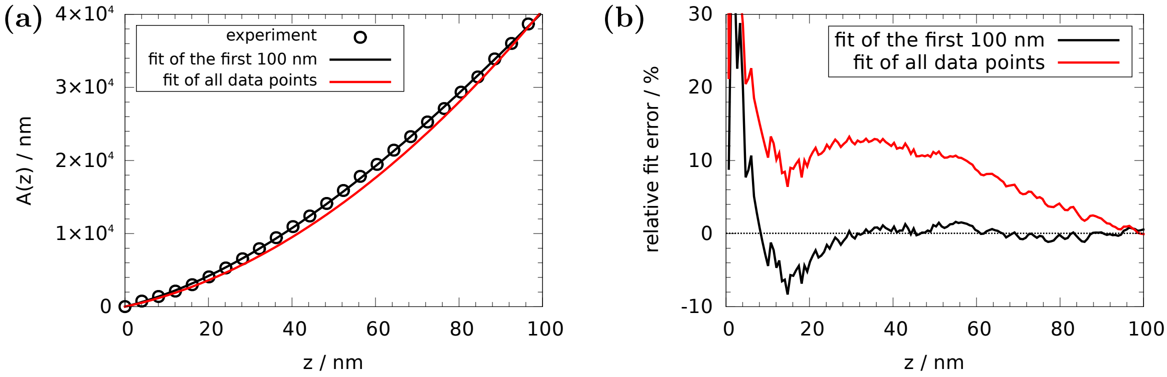

Figure 3.8.: (a) A fit of the first 100 nm (black line) is compared to a fit of the whole data set (red line). (b) The relative fit errors of the respective fits in (a).

Area function from SEM images

While it is in principle possible to image a tip with scanning electron microscopy (SEM), it is not a preferred method. One reason is that using SEM is time consuming. The tip has to be introduced into the SEM system, imaged at different angles at a high enough resolution, and then transferred back to the AFM system. Any additional step, where the AFM probe is handled manually increases the risk of breaking it. When using the dilation method, only the sample has to be replaced by a characterization grid and scanned subsequently. However, the most important reason, why the use of SEM to collect an indenter's area function is discouraged is the linear term in equation 3.8. While it is perfectly possible, it would be practically unfeasible to generate a 3D image out of a series of SEM scans. The effort of measurement and evaluation would simply be too high for a characterization which should be carried out before the start of every experiment. Additionally, there are the resolution limits of SEM which come into account when the first 100 nm of the tip are of interest. Therefore, instead of reconstructing the entire tip, one would measure the angles of the tip's side planes. From this, it is possible to derive an analytical expression for the area function by considering the tip geometry, similar to, e.g., equation 3.6. The problem of this approach was already discussed: While the theoretical area function is described by a purely parabolic relation, a linear term is introduced in the experimental area functions by imperfections such as curve side faces or a tip apex with a finite radius. Obviously, the linear term of $A(z)$ will become negligible at high indentation depths. For the four-sided pyramidal tips (ND-DYIRS) considered above, this would mean an indentation depth of approximately $1.6\,\mu$m is necessary for the linear term to be less than 5 % of the total area. Since most of the indentations were between 40 nm (dry cellulose) and 500 nm (highly swollen cellulose), the linear term of equation 3.8 could never be neglected.

Instead of measuring the angles of the tip's side planes from an SEM image, a method was proposed [37] where the widths of the side planes are measured and used to calculate the area at different heights. Then, the data are fitted with a second order polynom. This method will most likely yield better results than calculating the area function from the measured angles, however, it suffers the same shortcomings for low indentation depths. Therefore, here the dilation method was chosen to characterize the tip shape for AFM-NI.

3.2.2. Tip cleaning

While performing indentations, the tip might pick up loose nanoscale debris from the surface under investigation. In fact, this should be a dynamic process of picking up and losing contaminations during the progress of the experiment. It can hardly be avoided but seems of minor concern during indentation, since no degenerative change in hardness or reduced modulus was observed. However, if the tip is used again, the determination of its area function $A_c(x)$ (see subsection 3.2.1) will be disturbed by the debris attached to the tip. In figure 3.9a, a contaminated tip after a series of indents is displayed. The easiest way to clean such a contaminated tip is to indent it into an epoxy layer with a thickness of at least several hundred micrometer. This layer was prepared by placing a drop of two component epoxy glue (UHU Endfest 300) on a steel plate with a diameter of 18 mm, covering most of the plate's surface. The material was then cured at 100 ℃ for approximately 10 min in an oven. Performing indents on the epoxy surface while the cantilever is excited at its resonance frequency and repeating this at three to five different spots leads to a perfectly clean tip, as is presented in figure 3.9b.

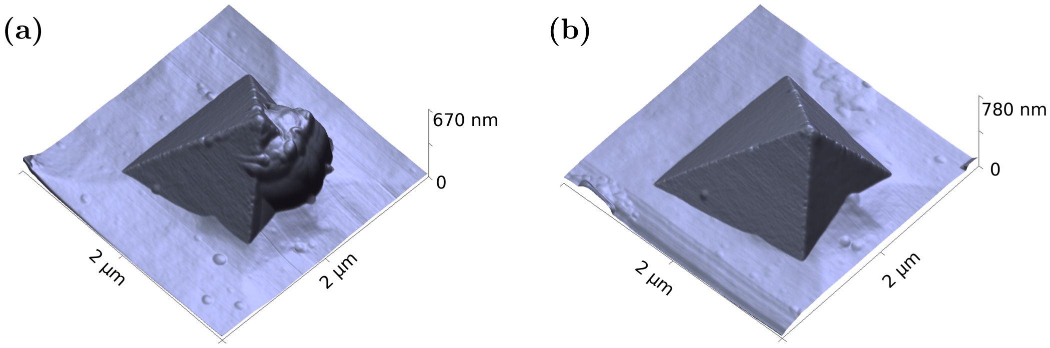

Figure 3.9.: Contaminated (a) and cleaned (b) full diamond tip.

Initially, the cleaning procedure was performed on microtome cross-sections of viscose fibers as well as of paper sheets. Viscose fiber cross-sections are approximately circular with a diameter of 20 μm to 30 μm and provide, therefore, only a very limited usable area. On paper sheet cross-sections, only the cell walls of the individual fibers can be used to clean the tip, since the gaps between the fibers as well as their lumina are either empty or filled with debris from microtome cutting. Therefore, AFM topography scans preceding the actual cleaning procedure were necessary in both cases. The epoxy surfaces, as prepared like mentioned above, on the other hand, are very smooth, homogeneous, and free of debris. No AFM scans prior to the indents are needed, which reduces the time of the cleaning procedure from typically several hours to about half of an hour.

3.2.3. Measurement and evaluation procedure

Measurement procedure

By applying the experimental methods outlined in this chapter, AFM-NI can be performed. The detailed procedure is summarized in the following.

1. Determine the spring constant of the cantilever according to subsection 3.1.1.

2. Image the tip shape using the dilation method, as described in subsection 3.2.1.

3. Clean the tip by indenting into cured epoxy resin (see subsection 3.2.2) if necessary and image the tip again. Repeat this step until the tip is completely cleaned.
4. Scan the sample's surface in intermittent contact mode and find a suitable place to indent.
5. Set up a load schedule and indent into the surface.
6. Scan the surface again to verify if residual imprints are visible.
7. Move to a different position and start again from step 4.

Evaluation procedure

After P - z plots were recorded according to the measurement procedure described above, an evaluation in compliance with the theory presented in section 2.3 is carried out. A step-by-step indication of how the mechanical parameters H and E_r are extracted follows.

1. Subtract the cantilever's deflection z_d from z to get the indentation depth z_i according to equation 2.16.
2. Determine the thermal drift rate $\dot{z}_t$ by fitting a line to the holding segment towards the end of the unloading part.
3. Subtract the thermal drift from z, according to equation 2.11.
4. Find the end of the loading segment and extract the holding part at P_{max}.
5. Identify the creep rate at the end of the holding time $t_{h,c}$ by fitting equation 2.12 to this segment.
6. Find the unloading part and fit it with the model presented in equation 2.15 and calculate S.
7. Correct S according to equation 2.13 and obtain S^*.
8. Calculate the contact depth z_c with equation 2.14.
9. Determine the area function $A(z)$ by fitting the experimentally determined data with equation 3.8.
10. Calculate the hardness H and the reduced modulus E_r according to equations 2.4 and 2.7, respectively.

All values of H and E_r presented in this work were evaluated using this procedure. To allow the analysis of a large amount of data, an Octave [75] script was designed (see listing A.2 in appendix A) which implements these steps.

3.2.4. Comparison to results of classical NI

To check if AFM-NI with the procedure outlined in this section does yield meaningful results, a comparison to literature values [76] was performed. For this purpose, viscose fibers (Kelheim Fibres GmbH, Kelheim, Germany) were embedded in epoxy resin and microtome cut to access their cross-sections. Then, H and E_r were determined by using a three-sided pyramid as well as a four-sided pyramid as indenters. The results are presented in table 3.3. Apparently the tip shape has a significant influence on H and E_r, which is true for the AFM-NI values as well as the ones obtained by NI. While the results from AFM-NI do not completely coincide with the results from NI, they are undoubtedly in a close range. Considering the difference in tip geometries and the fact that fibers investigated by NI are from a different producer, this is a remarkable finding and proves the usefulness of AFM-NI for soft materials.

Table 3.3.: Comparison of AFM-NI results obtained from viscose fiber cross-sections with literature values.

Source	Tip geometry	Fiber producer	H / MPa	E_r / GPa	indents
this work*	3-sided pyramid	Kelheim Fibres	160 ± 16	7.8 ± 1.3	24
this work	4-sided pyramid	Kelheim Fibres	239 ± 8	12.6 ± 2.1	15
[76]	Berkovich	Lenzing	≈230	≈10	3
[76]	cube-corner	Lenzing	≈350	≈6.5	5

*published in [38]

3.3. Samples

3.3.1. Amorphous cellulose films

Amorphous cellulose films were used as model systems, to simulate pure cellulose surfaces. The films were produced at Graz University of Technology by spin coating silicon wafers with a 20 $\frac{\mathrm{g}}{\ell}$ solutions of trimethylsilyl cellulose (TMSC) in toluene. Subsequently, the TMSC film was exposed to a vaporous 10 % hydrochloric acid (HCl) solution for 3 min, which transforms TMSC into cellulose [77]. This process is repeated four times to create a film with a thickness – determined by reflection-absorption infrared spectroscopy [78] – of 315 nm ± 75 nm [38,79].

The same method was used to prepare films for topographical investigations as well as AFM-NI. Additionally, cellulose films with a single top layer of xylan were created to simulate the presence of hemicelluloses. Both types of model films were investigated in air, in water, and in a 0.1 $\frac{\mathrm{mol}}{\ell}$ $CaCl_2$ solution. Those samples were allowed to swell in the respective liquid for 4 h to 6 h [38,79].

3.3.2. Pulp fibers

The investigated pulp fibers were bleached and unbleached, unrefined, industrial kraft pulp fibers. This pulp is a mixture of spruce and pine fibers with a diameter between 20 μm and 30 μm and a length of approximately 3 mm to 5 mm. All samples arrived as never-dried pulp and were stored in a refrigerator to keep them in their initial state and to inhibit the growth of mold on the samples. For topographical investigations, the fibers were placed on a piece of a silicon (001) wafer on top of a steel sample holder and glued at their ends with nail polish. The silicon substrate was scratched randomly to provide an orientation aid (see figure 3.10a). Nail polish was favored before adhesive tape, since measurements were carried out also at high relative humidities of up to 80 %. At such high humidities it is likely that the tape would lose its adhesive power and the fiber would not be fixed securely.

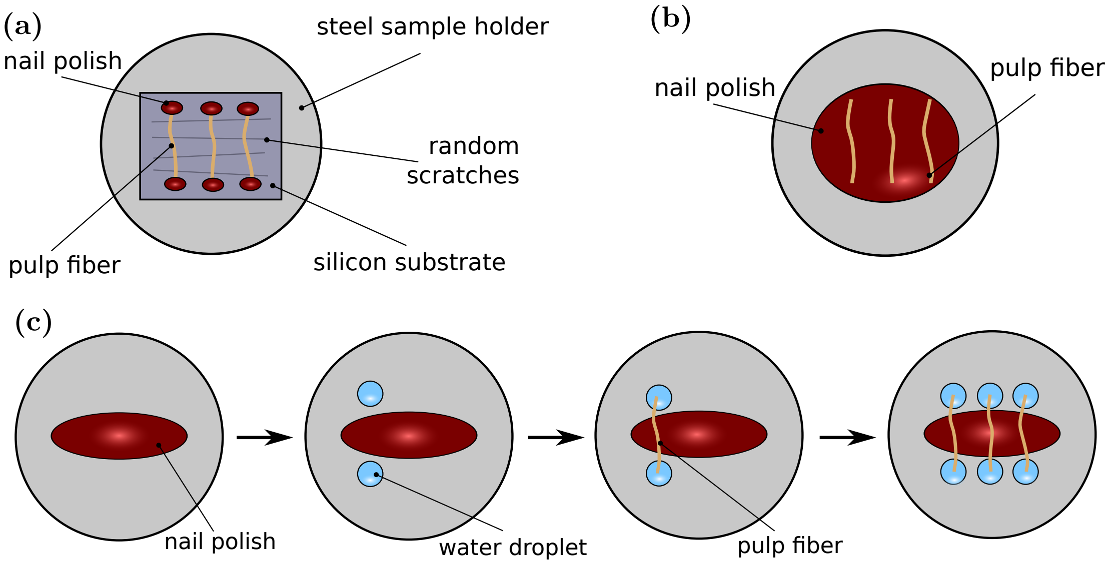

Figure 3.10.: Schematical illustration of the preparation of (a) pulp fibers for topographical investigations, (b) dried pulp fibers for AFM-NI, and (c) never-dried pulp fibers for AFM-NI.

Pulp fibers for AFM-NI measurements were placed on top of a drop of uncured nail polish to ensure that the fibers cannot move vertically during indentation, as is presented schematically in figure 3.10b. Then the nail polish was left to cure at room temperature for at least 12 h. If a fiber had to be investigated in its never-dried state, a sequence of preparation steps as indicated in figure 3.10c was employed. First, small water droplets were placed outside the nail polish, without touching it. The pulp fiber was then placed on the nail polish in such a way that its ends were sticking into the water droplets, as drawn in figure 3.10c. It was found that the best fixation of the fibers is achieved when the nail polish could cure for several minutes in air before placing the whole sample in distilled water. Nail polish will then also cure in water within 12 h, which was the time the fibers were stored in the water to ensure complete swelling.

3.3.3. Viscose fibers

Two different types of viscose fibers were investigated: classical or regular viscose with a typical diameter of 20 μm and fibers with a rectangular cross-section, 200 μm wide and 5 μm thick. All fibers had been already cut to a length of 4 mm by the supplier, Kelheim Fibres GmbH (Kelheim, Germany). The samples are sketched in figure 3.11. Classical viscose fibers feature a cross-section which can be described as cloud-shaped (figure 3.11a). The flat rectangular viscose fibers exhibit smooth surfaces with shallow trenches running along their longitudinal direction (figure 3.11b). In order to study the tunability of the fibers' swelling behavior, modified samples of each fiber type were prepared by Kelheim Fibres GmbH. Two common additives were chosen, and directly added to the viscose dope. Carboxymethyl cellulose (CMC) was used to obtain anionic fibers and cationic starch (CS) yielded cationic fibers. A complete list of samples including the amount of additives is presented in table 3.4.

Table 3.4.: Sample designations and amount of modifications present in the viscose fiber samples. The amounts of COOH- and N-groups correlate to the amount of CMC and CS, respectively. The values were determined by titration [23].

sample designation	fiber type	modification type	COOH % w/w	N % w/w
cRF	classical	none	0.77	-
cAF1		anionic	2.60	-
cAF2			3.78	-
cCF1		cationic	-	0.26
cCF2			-	0.13
rRF	rectangular	none	0.52	-
rAF		anionic	2.54	-
rCF		cationic	-	0.25
rACF		an./cat.	1.42	0.31

For AFM-NI investigations in air or in a controlled humidity environment, viscose fiber samples were prepared in the same way as dried pulp fibers. Classical viscose samples could also be prepared in this way for characterization in their fully swollen state in water. However, the rectangular fibers had to be prepared in compliance with the method developed for never-dried pulp fiber samples. When the fibers with rectangular cross-sections were glued in their dry state and then placed in water to swell, they would always detach from the nail polish surface. It is possible that due to their large width, they do not sink into the nail polish but merely adhere to its surface.

During swelling, they expand laterally and shear off from the nail polish and detach. All samples characterized in their fully swollen state were stored in distilled water for at least 12 h before AFM-NI characterization.

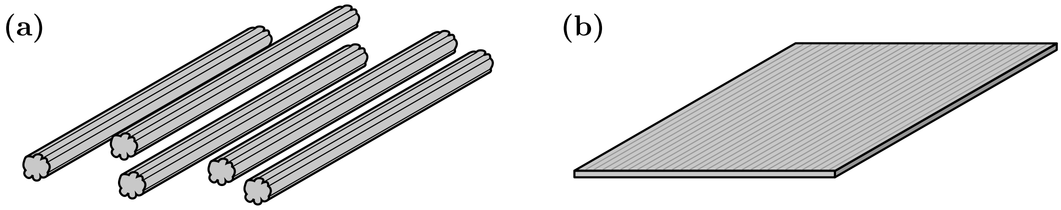

Figure 3.11.: Schematic representation of (a) classical viscose fibers and (b) flat and rectangular viscose fibers.

4. Results

4.1. Roughness characterization of cellulose films

Two amorphous cellulose films were prepared as model systems for fiber-fiber bonds. Both films were first investigated in their pristine state by AFM topography scans, then they were swollen in distilled water and pressed together at a pressure of 10 kPa to form a bond. After that, the films were glued to the upper and lower cylinder of a tensile tester with double-sided adhesive tape. By moving one of the cylinders, a load was applied until the bond was ruptured. Subsequently, another characterization of the films' surfaces by AFM was carried out. The preparation of the cellulose films as well as their bonding and rupturing were performed by S. Rohm at the Institute of Solid State Physics of Graz University of Technology [79].

In both cases, a comprehensive roughness analysis was performed to describe the samples' morphology and is the subject of the present work. To extract σ, ξ, and α from the HHCFs, equation 2.46 was fitted to the experimental data using a Levenberg-Marquardt algorithm [80,81].

4.1.1. Pristine films

Pristine amorphous cellulose films were prepared according to subsection 3.3.1 and investigated directly after their production. In the optical microscope attached to the AFM, the films appear to have thickness fluctuations on a large lateral scale of several hundred micrometers as is displayed in figure 4.1. These thickness fluctuations lead to different colors due to interference of the white light used for illumination.

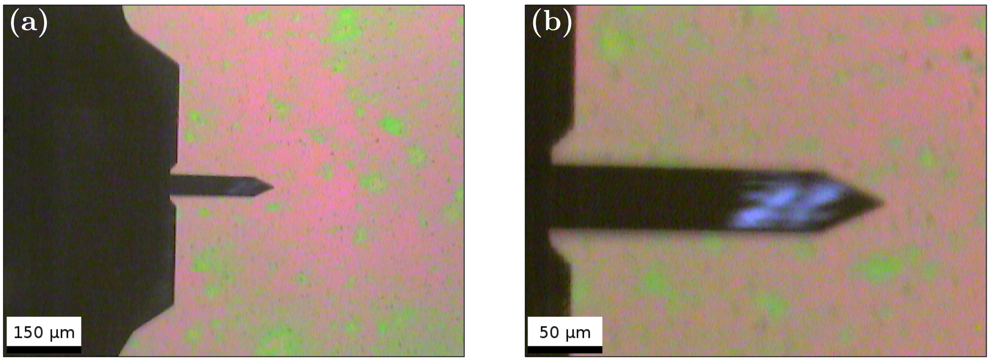

Figure 4.1.: Optical image of the cellulose film during AFM imaging with (a) width of approximately 1 mm and (b) 300 μm.

Figure 4.1b reveals that even the smaller patches of different height extend laterally for several tens of micrometers. Since the maximum scan size of the AFM is $90\,\mu\text{m} \times 90\,\mu\text{m}$, the larger patches cannot be fully analyzed using HHCF. Therefore, the focus is on smaller features which are around $10\,\mu\text{m}$, at largest. Such structures are revealed by AFM topography scans recorded in tapping mode and are observed on both cellulose films. $60\,\mu\text{m} \times 60\,\mu\text{m}$ images of cellulose films one and two are presented in figures 4.2a and 4.2c.

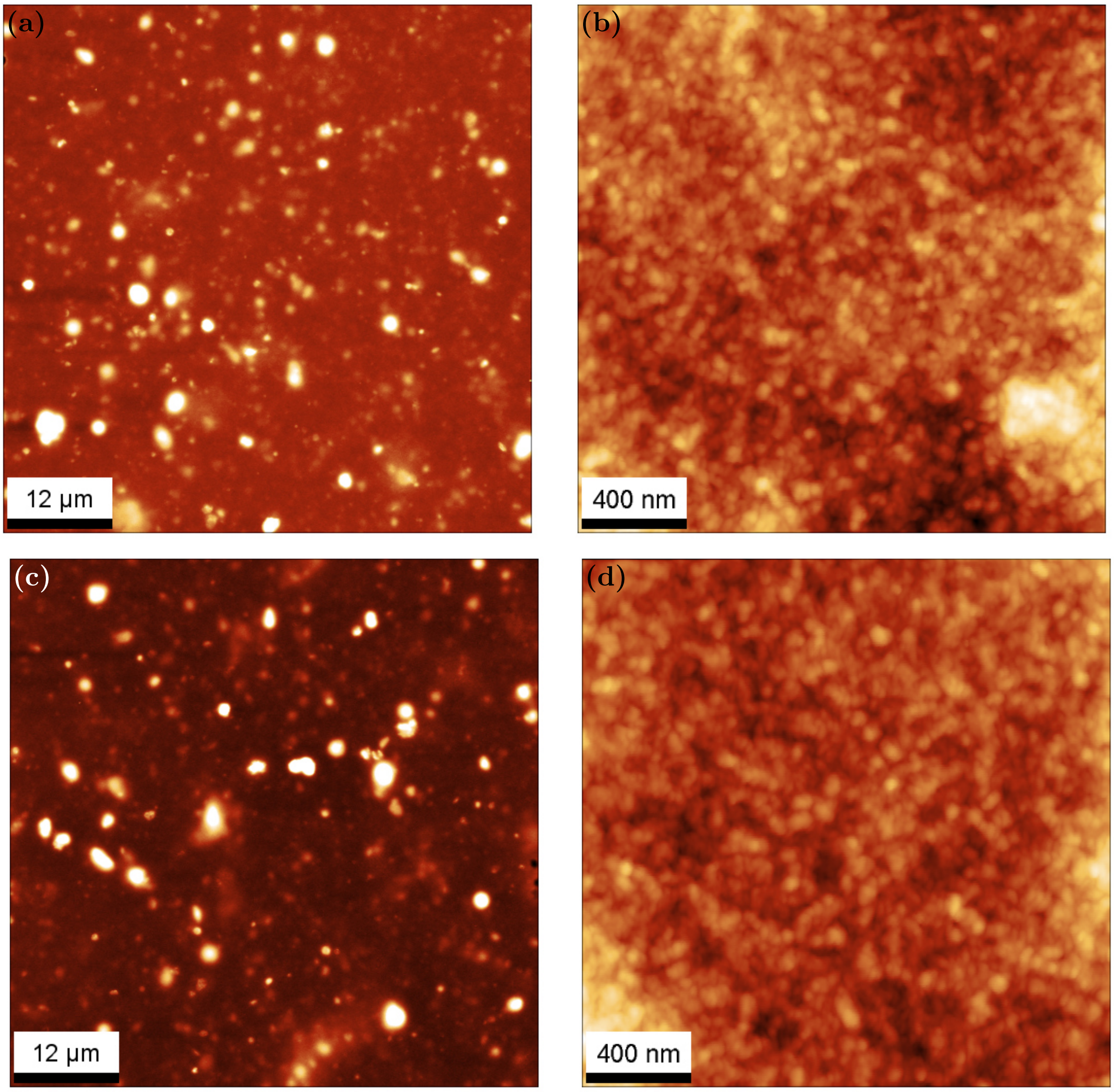

Figure 4.2.: AFM topography of cellulose film 1 (a) $60\,\mu\text{m} \times 60\,\mu\text{m}$ image, z-scale: 250 nm and (b) $2\,\mu\text{m} \times 2\,\mu\text{m}$ image, z-scale: 35 nm as well as of cellulose film 2 (c) $60\,\mu\text{m} \times 60\,\mu\text{m}$, z-scale: 250 nm and (d) $2\,\mu\text{m} \times 2\,\mu\text{m}$, z-scale: 35 nm.

Obviously, both samples exhibit a very similar surface morphology down to $2\,\mu\text{m} \times 2\,\mu\text{m}$, as is seen by comparing figures 4.2b and 4.2d. The most noticeable features on the large scale scans are round hills with a diameter of several micrometers and a height between 200 nm and 500 nm.

Before applying the theory of self-affine random rough surfaces – outlined in subsection 2.5.3 – to analyze the films' surfaces, the scaling behavior of the RMS roughness σ was investigated. If σ is related to the observation length L according to equation 2.43, self-affinity can be assumed. The randomness of the surface is already visible from figure 4.2, where no periodic features are observed. Figure 4.3 displays the scaling of σ in a linear and a logarithmic scale. From figure 4.3a, the cut-off length ξ_c is identified at around 30 μm, whereas the Hurst parameter α is extracted from the slope of the linear part from figure 4.3b by a linear least squares fit. It was found that $\alpha = 0.82 \pm 0.07$.

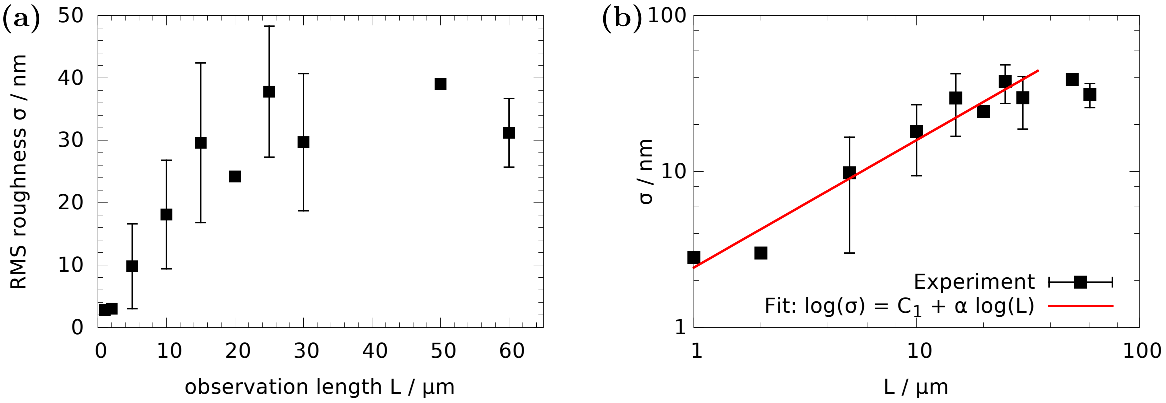

Figure 4.3.: The scaling behavior of cellulose film 1 visualized with (a) a linear scale and (b) a logarithmic scale. The fit in (b) determines C_1 to be 0.88 ± 0.18 and α as 0.82 ± 0.07.

The 1D-HHCF of 60 μm × 60 μm AFM topography images, calculated according to equation 2.25, were found to be in good agreement with the model for self-affine random rough surfaces from equation 2.46. This is visualized in figures 4.4a and 4.4b for cellulose film number one and two, respectively.

The resulting σ, ξ, and α data obtained from analyzing AFM scans on several length scales are listed in table 4.1. At scan sizes above 30 μm × 30 μm, all parameters become approximately constant. The RMS roughness σ is around 30 nm, the lateral correlation length ξ is approximately 1 μm, and the Hurst parameter α is about 0.85. Note that α from the RMS scaling (figure 4.3) is 0.82, which is in good agreement and further supports the assumption of the cellulose films being self-affine random rough surfaces with a cut-off.

It is noteworthy that figure 4.3 features further scan sizes besides the ones listed in table 4.1. In order to increase the number of data points, all images were divided into four quarters and σ was calculated for these images, too. Table 4.1 does not include these values, since they would be obtained from images with a resolution of only 512 × 512 px.

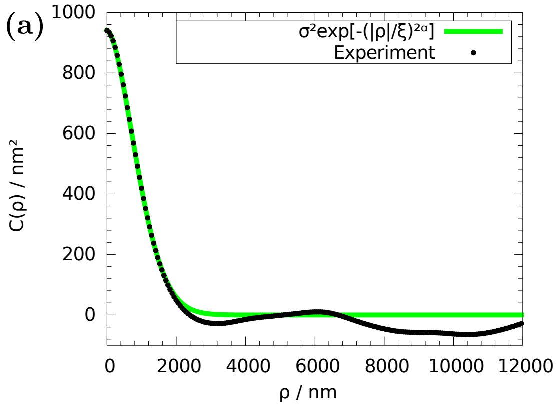

Figure 4.4.: Height-height correlation functions and their fits obtained from $60\,\mu\mathrm{m} \times 60\,\mu\mathrm{m}$ AFM topography images recorded on (a) cellulose film 1 and (b) cellulose film 2.

Table 4.1.: Roughness parameters σ, ξ, and α of pristine cellulose films from different scan sizes. All analyzed images were recorded with a resolution of $1024 \times 1024\,\mathrm{px}$.

scan side	film 1			film 2		
length	σ / nm	ξ / nm	α / 1	σ / nm	ξ / nm	α / 1
$60\,\mu$m	31.2 ± 5.5	1130 ± 200	0.90 ± 0.05	31.3 ± 4.2	1130 ± 60	0.90 ± 0.05
$50\,\mu$m	39.0	1500	0.80	-	-	-
$30\,\mu$m	32.2 ± 0.8	1040 ± 70	0.85 ± 0.05	-	-	-
$20\,\mu$m	24.2	920	0.85	-	-	-
$10\,\mu$m	11.0 ± 3.6	620 ± 100	0.80 ± 0.15	-	-	-
$2\,\mu$m	4.5 ± 2.1	160 ± 130	0.60 ± 0.15	4.0 ± 0.8	90 ± 20	0.75 ± 0.05
$1\,\mu$m	2.8 ± 0.1	50 ± 5	0.80 ± 0.05	-	-	-

At length scales between $2\,\mu$m and $10\,\mu$m, the surfaces of amorphous cellulose films appear to deviate from self-affine random rough surfaces with a cut-off. In figure 4.5, a $10\,\mu\mathrm{m} \times 10\,\mu\mathrm{m}$ and a $2\,\mu\mathrm{m} \times 2\,\mu\mathrm{m}$ AFM topography scan are displayed with their respective HHCFs. Both HHCF plots feature a distinctive kink, which is marked in figures 4.5c and 4.5d by arrows. Obviously, this fact does not hinder the determination of σ, whereas ξ and α can only be approximated. A possible explanation of the kink could be that the surface is a superposition of two uncorrelated random rough surfaces with different parameters. This seems likely when observing figure 4.5a. There, a fine-grained sub-structure is visible that resembles noise. A zoom of the surface is presented in figure 4.5b, where the small features – which lead to the noise-like appearance on larger length scales – are resolved. In the following, a model based on equation 2.46 will be developed that allows the description of these surfaces.

Suppose $z(x) = z_1(x) + z_2(x)$ with $z_1, z_2 \in \mathbb{R}$ then, according to equation 2.20

$$C(\rho) = \int_{-\infty}^{\infty} z(x) \cdot z(x+\rho)dx = \int_{-\infty}^{\infty} [z_1(x) + z_2(x)] \cdot [z_1(x+\rho) + z_2(x+\rho)]dx. \tag{4.1}$$

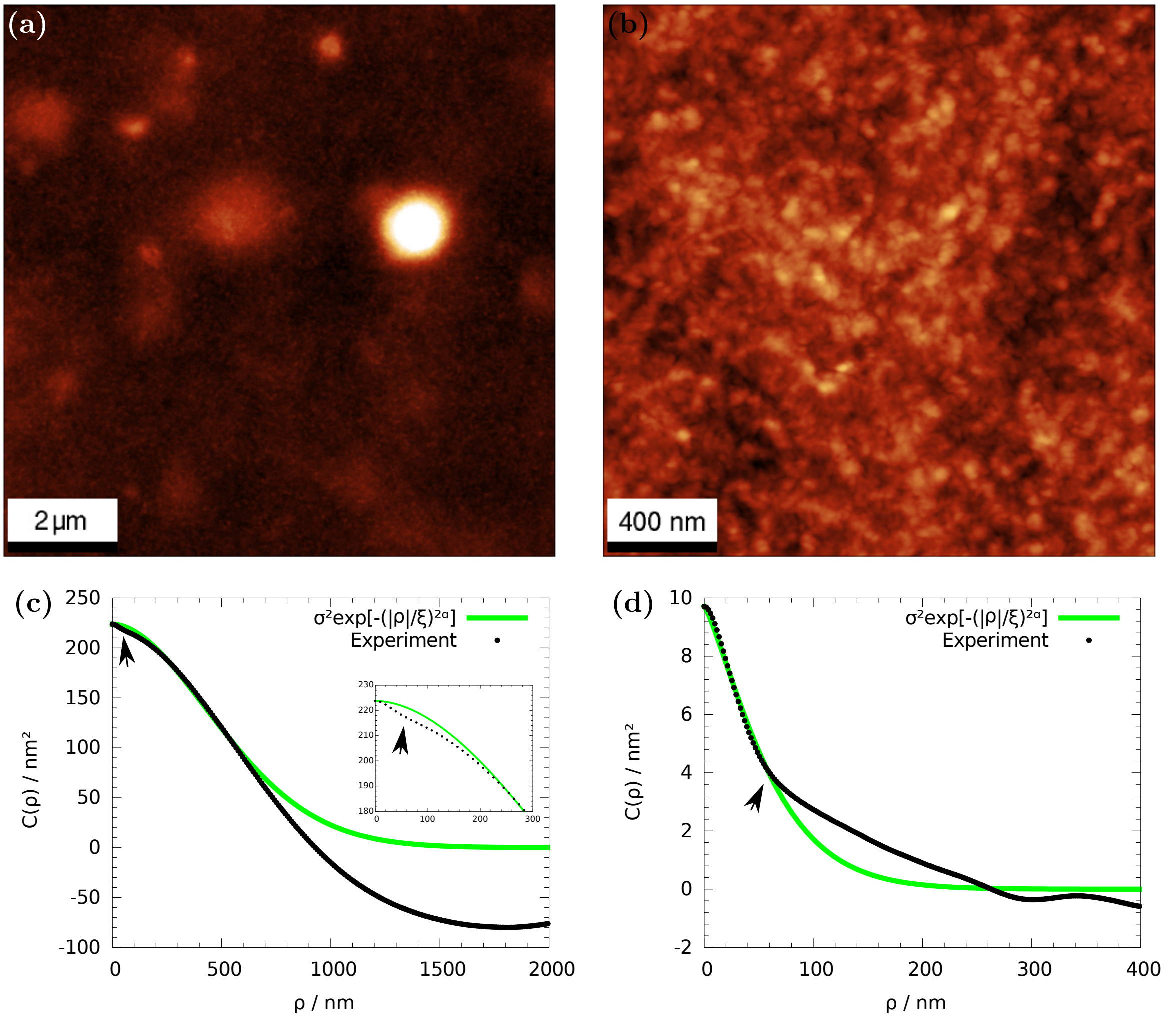

Figure 4.5.: $10\,\mu\text{m} \times 10\,\mu\text{m}$ AFM topography image (a) z-scale: 150 nm and (b) $2\,\mu\text{m} \times 2\,\mu\text{m}$, z-scale: 35 nm and (c), (d) the respective HHCFs. The inset in (c) is a magnification of the region where $\rho \leq 300\,\text{nm}$.

By expanding $[z_1(x) + z_2(x)] \cdot [z_1(x+\rho) + z_2(x+\rho)]$, the HHCF becomes a sum of four integrals

$$\begin{aligned} C(\rho) = & \int_{-\infty}^{\infty} z_1(x) \cdot z_1(x+\rho)dx + \int_{-\infty}^{\infty} z_1(x) \cdot z_2(x+\rho)dx + \\ & + \int_{-\infty}^{\infty} z_2(x) \cdot z_1(x+\rho)dx + \int_{-\infty}^{\infty} z_2(x) \cdot z_2(x+\rho)dx \end{aligned} \tag{4.2}$$

which represent, according to equations 2.19 and 2.20 HHCFs (ACovFs) and CCovFs

$$C(\rho) = C_1(\rho) + C_{12}(\rho) + C_{21}(\rho) + C_2(\rho). \tag{4.3}$$

If $z_1(x)$ and $z_2(x)$ are uncorrelated, then $C_{12}(\rho) = C_{21}(\rho) = 0$ and $C(\rho)$ is a superposition of the individual HHCFs

$$C(\rho) = C_1(\rho) + C_2(\rho). \tag{4.4}$$

An appropriate description of the surface could then be obtained by

$$C(\rho) = \sigma_1^2 e^{-\left(\frac{|\rho|}{\xi_1}\right)^{2\alpha_1}} + \sigma_2^2 e^{-\left(\frac{|\rho|}{\xi_2}\right)^{2\alpha_2}} \tag{4.5}$$

if $z_1(x)$ and $z_2(x)$ are self-affine and random rough with a cut-off. The square of the overall RMS roughness is obviously $\sigma^2 = C(0) = C_1(0) + C_2(0) = \sigma_1^2 + \sigma_2^2$. Note that this would be a non-linear fit with six parameters, which is not guaranteed to converge. By expressing, e.g., σ_2^2 as $\sigma_2^2 = \sigma^2 - \sigma_1^2$ and fixating $\sigma^2 = C(0)$, the fit parameters are reduced to five. If further the initial parameters are chosen correctly, it is most likely that a good fit is achieved.

Equation 4.4 was used by M. Tolan et al. as an ansatz to explain the combined roughness of polymer islands with capillary waves [82]. There, the surface was also considered to be a superposition of two uncorrelated surface profiles. However, it could not be described as a self-affine random rough surface, hence, the reported correlation function is different from equation 4.5.

For comparison, the HHCF plots from figure 4.5 are fitted with equation 4.5 and presented in figure 4.6. Evidently, equation 4.5 describes these HHCFs much better than the usual approach for self-affine random rough surfaces (equation 2.46).

Evaluating all $10\,\mu\text{m} \times 10\,\mu\text{m}$ and $2\,\mu\text{m} \times 2\,\mu\text{m}$ images using equation 4.5, yields the results presented in table 4.2. The overall RMS roughness σ is similar to the one listed in table 4.1, which is as expected. Splitting σ, ξ, and α into two sets for each surface, reveals that parameters with index $i = 1$ compare well for $10\,\mu\text{m} \times 10\,\mu\text{m}$ and $2\,\mu\text{m} \times 2\,\mu\text{m}$ images, whereas the parameters with $i = 2$ differ between scan sizes. In other words, σ_2 and ξ_2 scale with the scan size, whereas σ_1 and ξ_1 do not. Additionally, σ_1 and ξ_1 are always smaller than σ_2 and ξ_2. This leads to the conclusion that the parameters with $i = 1$ describe the fine-grained, noise-like structures observed in figure 4.5a, whereas the parameters with $i = 2$ correspond to the smooth large scale background.

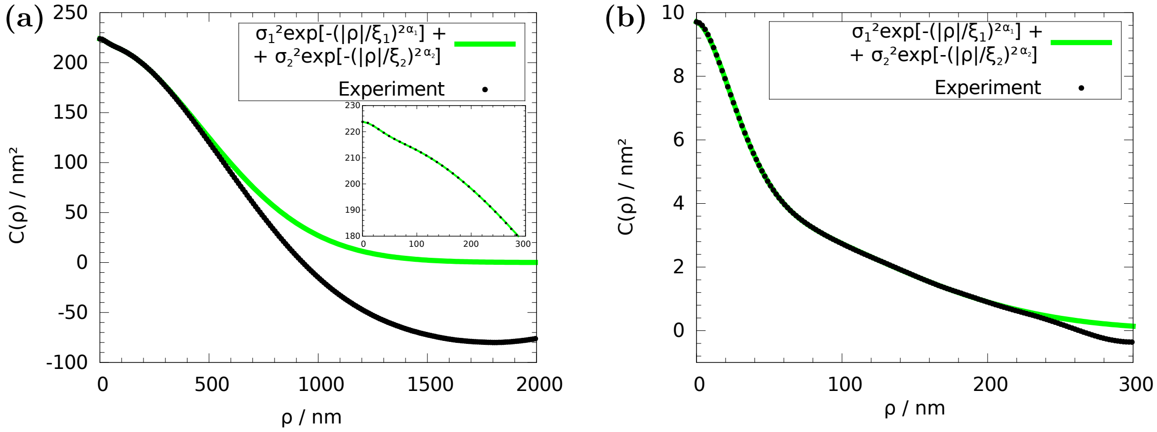

Figure 4.6.: HHCF plots of the (a) $10\,\mu\text{m} \times 10\,\mu\text{m}$ and (b) $2\,\mu\text{m} \times 2\,\mu\text{m}$ AFM topography scans, presented in figure 4.5 and fitted with equation 4.5. The inset in (a) is a magnification of the region where $\rho \leq 300\,\text{nm}$.

A likely explanation for this kind of surface structures is that the background is defined by the substrate's properties and/or defects induced during the spin-coating process. Such defects could be air bubbles or dust particles incorporated at the interface between the substrate and the cellulose film. The fine-grained structures would then be a result of the actual conformation of the cellulose surface.

Table 4.2.: Results of a roughness analysis of both cellulose films according to equation 4.5, presented as average values with standard deviations.

scan side length	σ nm	i	σ_i nm	ξ_i nm	α_i 1
$10\,\mu\text{m}$	11.0 ± 3.6	1	2.5 ± 0.3	50 ± 10	0.80 ± 0.10
		2	10.7 ± 3.7	660 ± 140	0.90 ± 0.05
$2\,\mu\text{m}$	4.4 ± 1.6	1	2.6 ± 0.1	40 ± 5	0.80 ± 0.05
		2	3.4 ± 1.9	260 ± 60	0.95 ± 0.05

4.1.2. Films after rupture

After the films were ruptured, a change in morphology was observed, see figure 4.7a for comparison. Now, holes dominate the surface instead of hills, and the overall appearance is more smooth. A possible explanation for this change in morphology is that the hills were actually bubbles which imploded while pressing the two films together. On $2\,\mu\text{m} \times 2\,\mu\text{m}$ AFM topography images, a fine structure of worm-like features is observed, as is displayed in figure 4.7b. This is similar to the pristine films, however the features on the ruptured films are finer and the surface is much smoother.

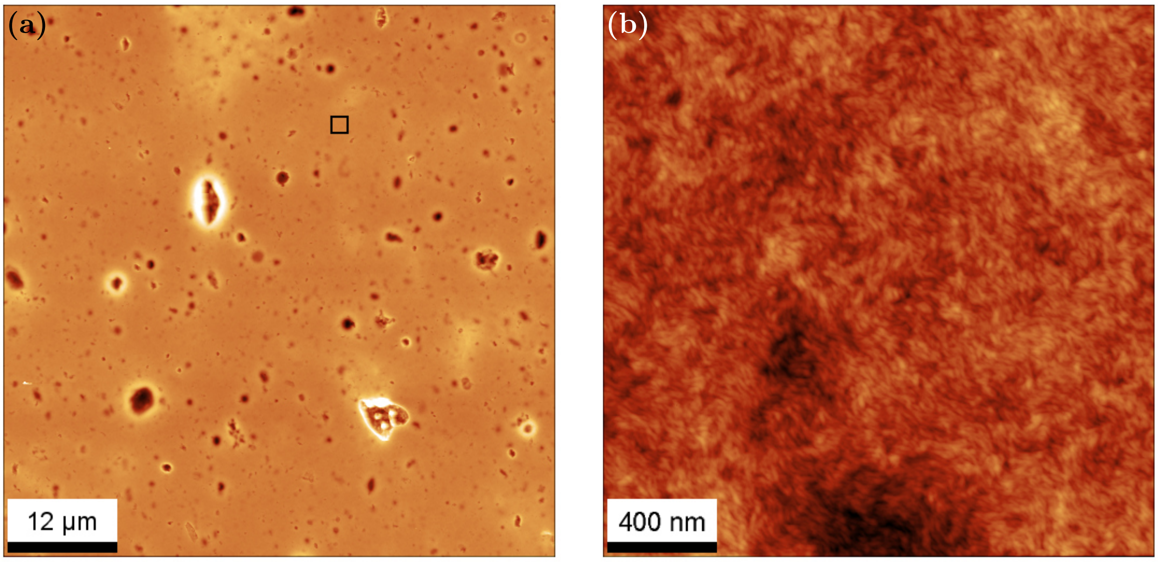

Figure 4.7.: AFM topography of a cellulose film after it has been ruptured (a) $60\,\mu\text{m} \times 60\,\mu\text{m}$, z-scale: 250 nm and (b) $2\,\mu\text{m} \times 2\,\mu\text{m}$, z-scale: 20 nm. The square in (a) indicates the position, where (b) was recorded.

From the pristine films, it could be concluded that both surfaces are identical. The same is true for the ruptured films which are, therefore, not distinguished from each other in the presentation of the results. The roughness analysis revealed that the ruptured films' surfaces are best described by two parameter sets of σ, ξ, and α, according to equation 4.5 even at an image size of $60\,\mu\text{m} \times 60\,\mu\text{m}$. In table 4.3, the results of the roughness analysis obtained on $60\,\mu\text{m} \times 60\,\mu\text{m}$ and $2\,\mu\text{m} \times 2\,\mu\text{m}$ images are listed. Compared to the pristine films, the overall RMS roughness σ on images with $60\,\mu\text{m}$ side length is smaller by a factor of more than 2. The lateral correlation lengths ξ_1 and ξ_2 are respectively smaller and larger than the single ξ of the pristine films, whereas the α_i are approximately the same as α.

Table 4.3.: Results of the roughness analysis of both cellulose films after rupture, presented as average values with standard deviations.

scan side length	σ nm	i	σ_i nm	ξ_i nm	α_i 1
$60\,\mu\text{m}$	13.2 ± 2.1	1	11.3 ± 1.2	550 ± 60	0.80 ± 0.05
		2	6.7 ± 2.4	3560 ± 570	0.95 ± 0.05
$2\,\mu\text{m}$	2.3 ± 0.6	1	1.0 ± 0.4	30 ± 20	0.70 ± 0.10
		2	2.0 ± 0.7	190 ± 60	0.80 ± 0.15

How can one interpret these results: The fact that the surface of the ruptured films is isotropic and smoother than the pristine films suggests that the whole surface except the holes was in molecular contact. It implies further that during bond formation – which is performed after swelling the films in water – the surfaces become soft enough to gain almost full contact when pressing the films together.

4.2. Mechanical properties of cellulose films

In the previous section, it was found that amorphous cellulose films possibly form a high area in molecular contact when pressed together in the swollen state and dried subsequently. Two rough surfaces can only conform to each other by deforming plastically and elastically – either due to the mechanical pressure or capillary pressure [83]. Both cases imply that the material's mechanical properties allow such deformations. To determine how much cellulose films soften when they are swollen, AFM-NI was employed and the hardness H as well as the reduced modulus E_r were detected. Moreover, possibilities to tune mechanical properties of swollen cellulose – by either modifying the material or the swelling solution – were investigated.

Coating the cellulose film with xylan was used to change the material itself. Since hemicelluloses are present on paper fibers as well, this modification is a step towards a more complex system. Furthermore, it was found that dimethyl sulfoxide (DMSO) – a solvent for xylan, which is used to spin coat xylan on the cellulose film – can be kept incorporated into the material [84]. This turned out to be an additional possibility to change the material's properties and to influence the mechanical properties of the swollen film.

The addition of salt to the swelling medium – distilled water – was investigated as a way to influence the swelling behavior of cellulose films externally. It has been known for a long time that salts provide this possibility for cellulosic materials [85]. The effect of swelling on the mechanical parameters of cellulose, however, has only been investigated by quartz crystal microbalance and not by direct means, such as NI [86]. Common salts to be used for these studies are NaCl and $CaCl_2$. Here, an aqueous $CaCl_2$ solution with a concentration of $0.1\,\frac{\text{mol}}{\ell}$ was selected.

Figure 4.8 summarizes the results of AFM-NI on pure cellulose films in dry and swollen states and presents exemplary P - z_i plots. AFM-NI performed on dry cellulose films ($\varphi_r = 0.45$, $\vartheta = 24\,℃$) with three-sided pyramidal tips (ND-DTIRS) yielded a hardness $H = 190\,\text{MPa}$ and a reduced modulus $E_r = 6.3\,\text{GPa}$. The AFM topography image displayed in figure 4.8a shows residual imprints on a dry cellulose film surface. In comparison, figure 4.8b presents residual imprints on a fully swollen cellulose film. Both images feature the same lateral scale. Hardness and reduced modulus of the swollen film decreased to $6\,\text{MPa}$ and $56 \times 10^{-3}\,\text{GPa}$, respectively.

Apparently, swelling of cellulose in distilled water leads to a decrease of H by a factor of 30 and E_r by a factor of 100. This fact is emphasized by comparing the residual imprints in figures 4.8a and 4.8b, created with the same load schedule. Exemplary P - z_i plots of dry and swollen films are presented in figure 4.8c. They clearly show that swelling leads to an increase in indentation depth and a decrease in stiffness, as is

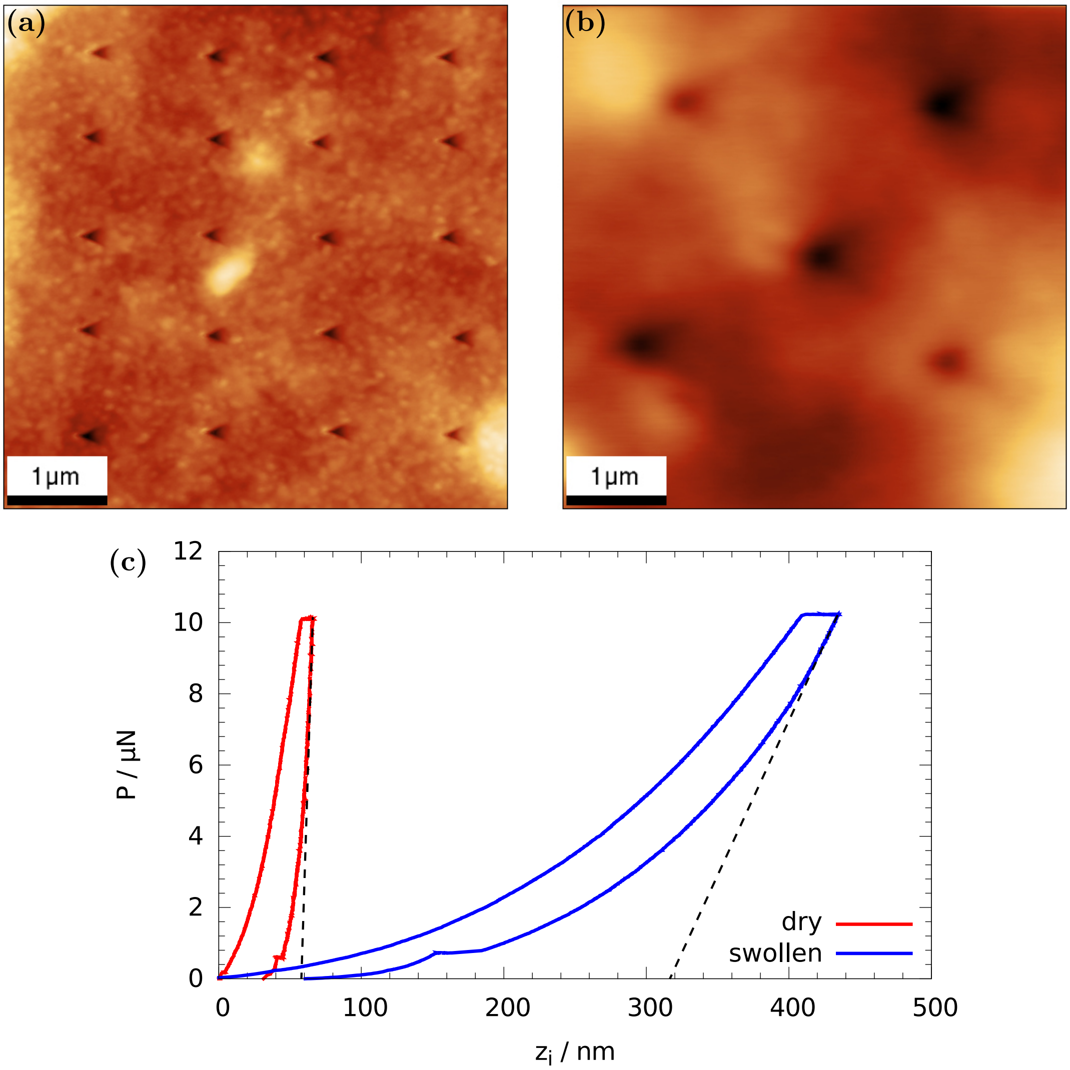

Figure 4.8.: $5\,\mu\text{m} \times 5\,\mu\text{m}$ AFM topography of a (a) dry and (b) fully swollen cellulose film after AFM-NI was performed. The z-scales are (a) 75 nm and (b) 50 nm. (c) Exemplary P - z_i plots of a dry (red) and a swollen (blue) cellulose film.

expected.

A summary of H and E_r from cellulose and xylan/cellulose films is listed in table 4.4 and visualized in figure 4.9. Before interpreting these results, it should be noted that the film thickness in the dry state is only ≈300 nm. This low thickness has the effect that the mechanical properties of the film might be influenced by the underlying hard substrate. Pelegri and Huang performed finite element simulations of soft thin films on hard substrates and concluded that the hardness is not affected by the substrate. However, the reduced modulus was found to be overestimated in such a system [87]. Since all films have approximately the same thickness, this overestimation of E_r would be the same for all films and is hence of no concern. Only when comparing the values to other materials, it is important to note that E_r values are higher than they would be in a bulk material.

The addition of xylan to the cellulose film leads to a decrease of the dry film properties as well as the ones of the swollen film. If $CaCl_2$ is present in the swelling solution, pure cellulose films will become harder and stiffer, whereas xylan/cellulose films will become softer and more compliant compared to the ones swollen in pure, distilled water. The largest decrease of H (by a factor of 56) and E_r (by a factor of 190) was found when DMSO is still present in the film. Each of the differences in table 4.4 and figure 4.9 are significant according to a Welch test [88] at a significance level of 0.05. The Welch test was preferred over the t-test since not all samples were from populations with equal variances.

Table 4.4.: H and E_r of cellulose films determined by AFM-NI. The last two columns (r_H and r_E) are the ratios of H and E_r with respect to the first line (pure cellulose in air). These data were published in [38,79].

film type	medium	H MPa	E_r GPa	r_H 1	r_E 1	Nr. of indents
cellulose	air, $\varphi_r = 0.45$	190 ± 24	6.3 ± 1.0	1.0	1.0	10
	H_2O (dist.)	6.0 ± 0.3	$(56 \pm 2) \times 10^{-3}$	32	113	9
	H_2O (dist.) + $CaCl_2$	7.7 ± 0.5	$(63 \pm 3) \times 10^{-3}$	25	100	20
cellulose +xylan	air, $\varphi_r = 0.49$	150 ± 15	4.7 ± 1.0	1.3	1.3	29
	H_2O (dist.)	3.9 ± 0.1	$(46 \pm 1) \times 10^{-3}$	49	137	10
	H_2O (dist.) + $CaCl_2$	3.5 ± 0.1	$(42 \pm 1) \times 10^{-3}$	54	150	9
	H_2O (dist.) + DMSO	3.4 ± 0.2	$(33 \pm 1) \times 10^{-3}$	56	191	10

The presence of pure water in cellulose and xylan/cellulose films always leads to a reduction of H and E_r compared to the dried state (see table 4.4). During swelling, water will bind to the cellulose or hemicellulose and increase the mobility of the molecule chains, yielding an easily deformable material [89]. Xylan/cellulose films are inherently softer than cellulose films and it is, therefore, no surprise that the same is also true for fully swollen films.

To explain the behavior of cellulose and xylan in the presence of $CaCl_2$, a model developed by F. G. Donnan in 1911 to describe the swelling of hydrogels is applied. This model views the hydrogel and the salt solution as two liquids separated by a semi-permeable membrane. Charged groups of the hydrogel cannot penetrate the membrane – since they are fixed to the bulk – whereas small ions are able to move freely. This theory is known as the Donnan theory [90] and was successfully applied to pulp fibers [85]. In this model, the increased swelling of xylan/cellulose films in a salt solution is then caused by osmotic pressure. Xylan exhibits acidic (COOH) groups which attract the metallic salt ions (Ca^{2+}) and lead to an increased salt concentration inside the gel. To equilibrate the concentration difference, a net flow of water into the xylan bulk is generated due to osmotic pressure. Pure cellulose, on the other hand, has no acidic groups and the concentration of salt in the bulk is lower than in the solution. Again, a net movement of water caused by osmotic pressure is the result, however, in this case water will flow out of the bulk and the cellulose will deswell [38].

The effect of DMSO on H and E_r is also not surprising. DMSO is a solvent for xylan that breaks the hydrogen bonds apart and, therefore, weakens the structure of the film [84].

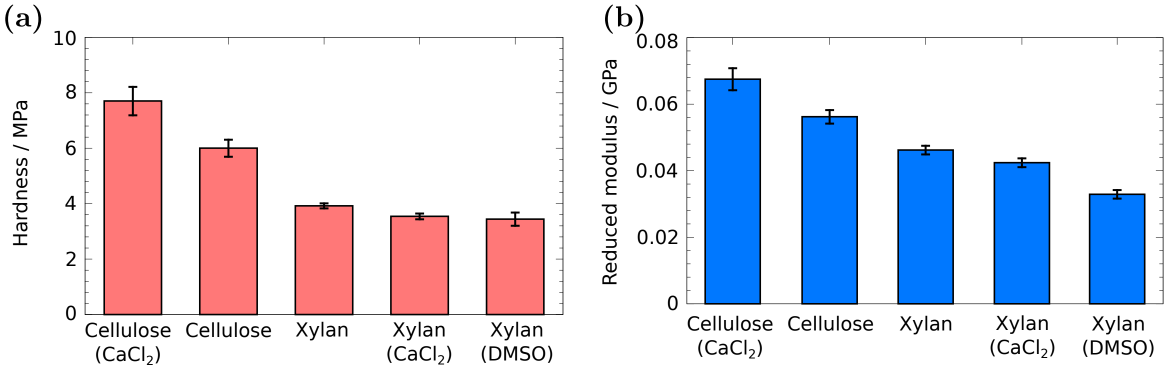

Figure 4.9.: Mechanical properties of swollen cellulose and xylan/cellulose films presented as (a) hardness H and (b) reduced modulus E_r determined by AFM-NI.

To test the effect of swelling on bond formation, cellulose films prepared the same way as the ones listed in table 4.4 were made to form bonds. Subsequently, the bonds were ruptured and the bond strength was detected. Again, the preparation, bonding, and tensile testing of the cellulose films was performed at the Institute of Solid State Physics of Graz University of Technology [79,84]. Hardness respectively reduced modulus seem to correlate to the bond strength of cellulose films in such a way that low H and low E_r lead to a high bond strength. Figure 4.10 presents the measured bond strength plotted versus H and E_r to emphasize this correlation.

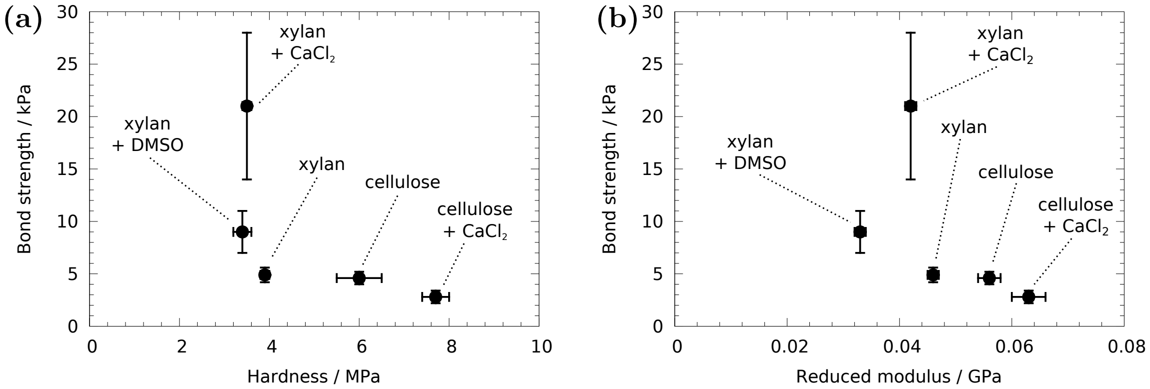

Figure 4.10.: Bond strength of cellulose films plotted versus their (a) hardness and (b) reduced modulus. The bond strength data are taken from [79].

The average bond strength of xylan/cellulose films swollen in $CaCl_2$ is by far the highest of all samples, even though the films with DMSO are supposed to be softer and more compliant. This large increase in bond strength is an indication of Coulomb interactions, which are enabled by the Ca^{2+} ions from the swelling liquid. The fact that pure cellulose films swollen in $CaCl_2$ have the lowest bond strength, indicates that in this case no Coulomb interactions are present, which apparently need xylan to establish [79].

4.3. Mechanical properties of viscose fibers

The description of mechanical properties of viscose fibers will start with the fully swollen state in accordance with cellulose films from the previous section. A focus will be set on possibilities to tune the swelling capability of viscose fibers by modifying the raw material with additives. Furthermore, a clear relation between swelling as an increase of physical dimensions and a decrease of H and E_r will be pointed out. Then, a comprehensive study of the effect of relative humidity on viscose fibers' hardness and modulus will be presented. For this purpose, classical viscose fibers without any additives are used.

Both investigations aim to deepen the understanding of water uptake of cellulose and its implications on mechanical properties and bond formation between two fibers. The application of the results presented in the following are twofold. First, viscose fibers are viewed as sophisticated model systems for paper fibers, allowing insights into bonding mechanisms such as hydrogen bonding and Coulomb interactions. Second, also industrial applications of viscose fibers – such as additives to paper – could profit from these investigations.

4.3.1. Tuning hardness in the wet state

Classical viscose fibers as well as viscose fibers with a rectangular cross-section were investigated by AFM-NI. The fibers were modified by the supplier, Kelheim Fibres GmbH, with additives (see table 3.4) to influence their swelling behavior, which was characterized in a preceding study [23]. Two types of additives were used: CMC and CS, which are anionic and cationic modifications, respectively. By producing single viscose fiber-fiber bonds, it was found by F. Weber et al. that increased swelling is indeed beneficial and leads to stronger bonds [23]. Since the modifications change the surface charge of the fibers, Coulomb interactions are also likely to influence the bond strength between two fibers.

Topography

An AFM topography scan of a classical viscose fiber is presented together with a typical line profile in figure 4.11. Due to the fibers' large curvature, $8\,\mu\text{m} \times 8\,\mu\text{m}$ was the maximum possible scan size. The surface is dominated by bulges, which are aligned parallel to the fiber's long axis. These bulges vary in width between $1\,\mu$m and $3\,\mu$m, as is visible from the line profile in figure 4.11b. The height of these structures is locally only several hundred nanometers, but due to the curvature caused by the approximately circular cross-section the surface appears much rougher. Indents can only be performed on a local maximum, i.e., on the top of a bulge. Otherwise, H and E_r would be affected too much. For AFM-NI, a scan size of $5\,\mu\text{m} \times 5\,\mu\text{m}$ was used to minimize the effect of surface curvature. The disadvantage of such a small scan size is that the number of indents per scan is also small.

Viscose fibers with a rectangular cross-section are much smoother and thus provide access to large surface areas. Therefore, the AFM topography scans displayed in figure 4.12 could all be recorded with a scan size of $20\,\mu\text{m} \times 20\,\mu\text{m}$. Note that in figure 4.11 a z-scale of $2\,\mu\text{m}$ was used, whereas in figure 4.12 300 nm is sufficient. Both fibers feature the aforementioned bulges and large trenches parallel to the main axis of the fiber. Rectangular viscose fibers, however, lack the surface curvature which defines the morphology of classical viscose fibers and, hence, appear more smooth in the AFM scans. Because of this smooth surface, it is much easier to collect a large amount of indents in one region of the fibers. Still, indents have to be placed on locally flat positions or at a local maximum, but wide scan sizes can be used which include a high amount of suitable positions.

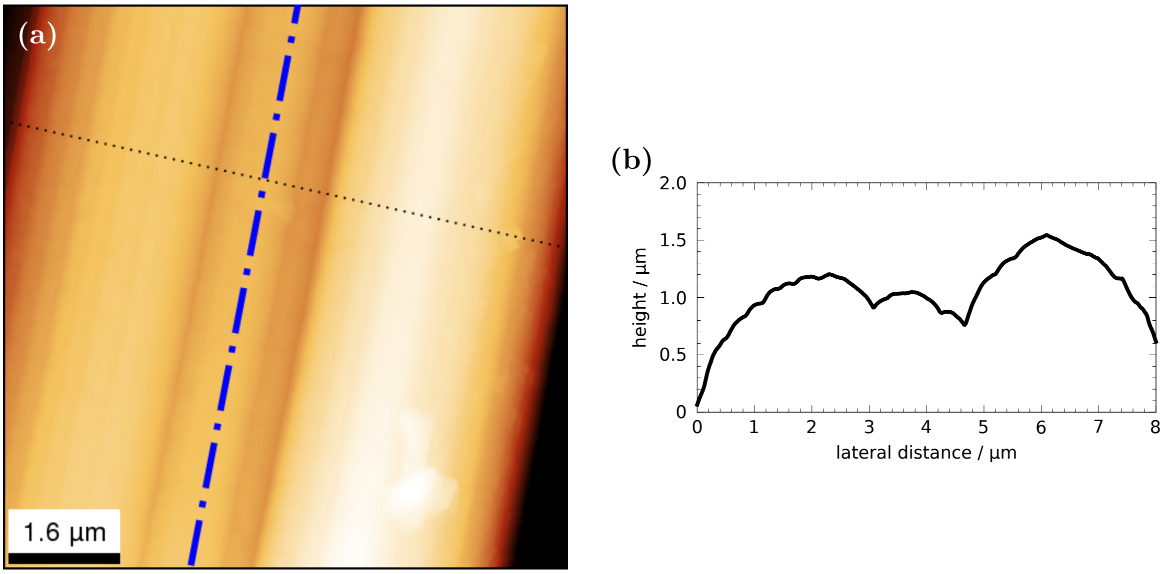

Figure 4.11.: The surface of a classical viscose fiber without additives. (a) $8\,\mu\text{m} \times 8\,\mu\text{m}$ AFM topography image, z-scale: $2\,\mu\text{m}$. The main fiber axis is parallel to the straight, almost vertical trenches as is indicated by the blue dot and dash line. (b) Line profile extracted from (a) at the position indicated by a dashed line. (Modified from [50].)

Since the flat, rectangular viscose fibers provide a well accessible surface morphology, with the possibility of large scan sizes, they were used to examine if there is a relation between surface morphology and the presence of additives. The 1D-HHCF was calculated from $20\,\mu\text{m} \times 20\,\mu\text{m}$ images along the horizontal direction and fitted with equation 2.46 to obtain σ, ξ, and α. Inspecting figure 4.12 reveals that the surfaces of the flat viscose fibers are not random rough, but anisotropic in the fibers longitudinal direction. However, σ and ξ still carry some information for characterizing the surface. Obviously, σ describes the vertical roughness as on any surface. The lateral correlation length ξ is here a measure for the width of the longitudinal bulges or wrinkles. α is likely to be the least significant parameter.

The results of the roughness analysis are listed in table 4.5. The anionic fibers rAF exhibit the lowest RMS roughness, while the cationic fiber rCF has the highest σ. Considering the large standard deviations, no significant difference is present. A similar argument can be made for ξ: While the average lateral correlation lengths differ, a significant distinction is not permitted due to the large standard deviations.

It is apparent from figure 4.12 that the fibers' main axes are not perfectly parallel to the y-axes of the images. Thus, the determined values for ξ are overestimated compared to parallel aligned fibers. A geometrical consideration immediately yields that the corrected lateral correlation length ξ' would be $\xi' = \xi \cos(\beta)$, with β denoting the tilt angle of the fiber with respect to the y-axis. The maximum observed tilt angle was 10°, which would result in $\xi' = 0.985\,\xi$. This means that in the worst case, the values of ξ are overestimated by 1.5 %. Considering the already discussed large standard deviations of ξ (see table 4.5), the correction was not applied, since it would not lead to a significant change of neither the results nor their interpretation.

Table 4.5.: Roughness parameters obtained from 20 μm × 20 μm AFM topography images of flat, rectangular viscose fibers. All values are obtained from eight positions on two fibers, except the values for rRF, which are from four positions on one fiber.

	rRF	rAF	rCF	rACF
σ / nm	44.2 ±24.0	28.6 ±6.8	69.1 ±28.4	49.7 ±33.9
ξ / nm	980 ±130	920 ±410	720 ±160	850 ±240
α / 1	0.8 ±0.1	0.7 ±0.1	0.8 ±0.1	0.7 ±0.1

A qualitative observation from figure 4.12 is that all surfaces feature trenches with a fractal appearance which are aligned approximately perpendicular to the fibers' main axes. These fractal trenches seem to be most pronounced on the reference fiber rRF (figure 4.12a) and the cationic fiber rCF (figure 4.12e). On both of these samples, trenches with a length of more than 20 μm are observed. The three arrows in figure 4.12c, e.g., indicate most likely segments of one and the same trench. An exact length can, therefore, not be given. The depth of these trenches is approximately 100 nm at the deepest positions. The other two fiber types, rAF and rACF (figure 4.12b and f, respectively), feature only faintly visible trenches which appear much shorter. However, it is possible that also these small trenches are connected to form large ones, but with connections so shallow that they cannot be properly identified. The depth of these shallow trenches is 15 nm at maximum. Note that these faintly visible trenches are present on all fiber types. Only on rRF and rCF the pronounced, large trenches are dominating the surface.

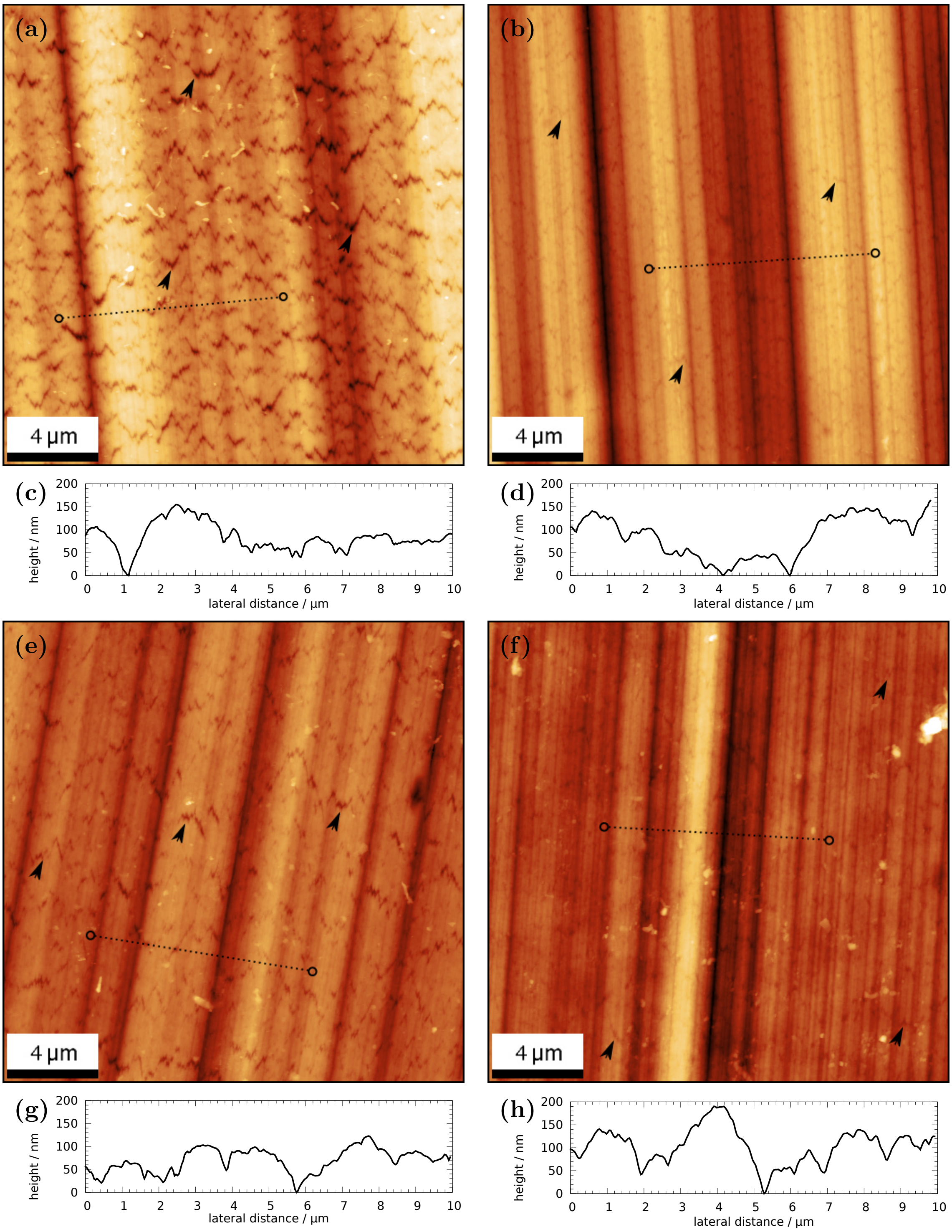

Figure 4.12.: $20\,\mu\text{m} \times 20\,\mu\text{m}$ AFM topography images of flat, rectangular viscose fibers: (a) rRF, (b) rAF, (e) rCF, and (f) rACF. All z-scales are 300 nm. The black arrows mark exemplary fractal-like trenches. The main fiber axes are in all cases parallel to the straight, almost vertical trenches. (c),(d),(g), and (h) are line profiles extracted from the images directly above them, the exact positions are indicated with dashed lines.

AFM-NI

All AFM-NI experiments here were performed using the four-sided pyramidal tips ND-DYIRS. It is, therefore, not easy to compare with results from the swollen cellulose films discussed earlier. The benchmark experiments carried out on viscose fiber cross-sections (table 3.3), however, suggest that H and E_r obtained by four-sided tips are 50 % to 60 % higher than H and E_r measured by three-sided tips. The viscose fibers were embedded in nail polish in the fully swollen state, according to subsection 3.3.3. In order to exclude an influence of the substrate on the measured properties, a model developed for classical NI on coated substrates was applied [91]. The hardness and reduced modulus of the nail polish in the dried state were measured with a three-sided pyramid and found to be 100 MPa and 1.5 GPa, respectively. By assuming a fiber thickness of 4 μm, no significant influence on H and E_r was detectable [38]. Since no swelling of nail polish in water was observed, this fact is also true for investigations of fully swollen materials in water.

In figure 4.13, P - z_i plots of the modified fibers are compared. Classical viscose fibers (figure 4.13a) and flat viscose fibers (figure 4.13b) respond in a similar manner to the additives. It is clearly visible that all modifications have a significant effect on the fibers' mechanical properties.

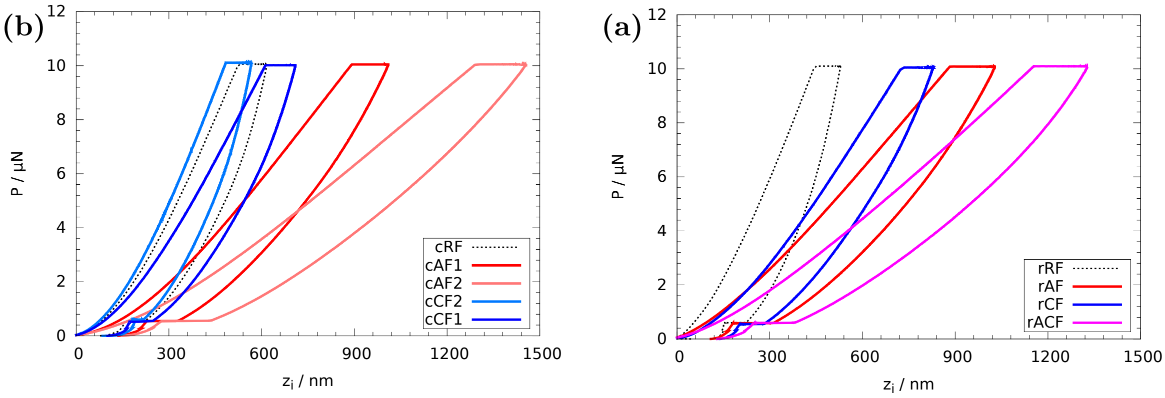

Figure 4.13.: Exemplary P - z_i plots recorded on (a) classical and (b) flat, rectangular viscose fibers with different modifications incorporated.

Hardness and reduced modulus obtained from all samples are summarized in table 4.6 and visualized for classical and rectangular fibers in figures 4.14 and 4.15, respectively. Unmodified classical fibers exhibit a hardness of about 14 MPa with a reduced modulus of 51×10^{-3} GPa. The addition of CMC to the fiber (cAF1) leads to a decrease of H by a factor of 2 and a reduction of E_r by a factor of almost 3. If more CMC is added (cAF2), the hardness is decreased by a factor of 3 and the reduced modulus by a factor of 6 compared to cRF. cAF2 exhibits the lowest values for hardness and reduced modulus of all the viscose fibers investigated. The incorporation of CMC into the fiber is, therefore, decreasing both parameters drastically. CS, on the other hand leads to a slight increase in H and E_r at low concentrations (cCF2) and to a decrease for higher concentrations (cCF1). All differences are significant under a Welch test at a significance level of 0.05.

Table 4.6.: Hardness and reduced modulus of swollen viscose fibers. The last column represents the number of indents as well as the number of fibers (in brackets) investigated. These values have been published in [50].

fiber type	sample designation	H MPa	E_r GPa	Nr. indents (Nr. fibers)
classical viscose	cRF	14 ± 1.0	$(51 \pm 11) \times 10^{-3}$	37 (3)
	cAF1	6.9 ± 1.3	$(18 \pm 4.2) \times 10^{-3}$	50 (5)
	cAF2	4.4 ± 0.9	$(8.3 \pm 1.9) \times 10^{-3}$	40 (3)
	cCF1	13 ± 2.0	$(44 \pm 3.4) \times 10^{-3}$	46 (3)
	cCF2	16 ± 0.9	$(64 \pm 4.8) \times 10^{-3}$	58 (4)
rectangular fibers	rRF	16 ± 2.3	$(54 \pm 16) \times 10^{-3}$	124 (4)
	rAF	7.2 ± 0.9	$(17 \pm 3.4) \times 10^{-3}$	91 (3)
	rCF	10 ± 1.1	$(27 \pm 4.8) \times 10^{-3}$	85 (4)
	rACF	4.6 ± 0.5	$(10 \pm 0.8) \times 10^{-3}$	101 (4)

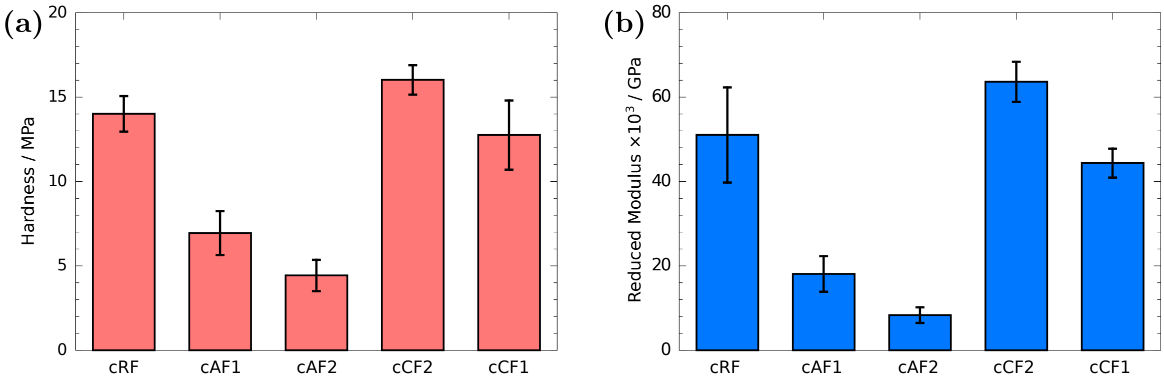

Figure 4.14.: AFM-NI results of swollen classical viscose fibers as (a) hardness and (b) reduced modulus.

The values of H and E_r of the flat reference fiber (rRF) are similar to the ones observed for the classical fiber without modifications (see table 4.6). rAF, which contains an amount of CMC comparable to that of cAF1, exhibits a hardness and reduced modulus which are almost identical to the values found for cAF1. Only the cationic fiber rCF differs significantly from its counterpart cCF1. However, H and E_r of rCF are ranged between these values from rRF and rAF, which is also the case for cCF1 and, hence, leads to the conclusion that rCF fits in principle into the series. Slight variations during the production process could explain the discrepancy between cCF1 and rCF, however, the amount of CS in both fibers is approximately the same (see table 3.4).

An influence of incorrect sample preparation – i.e., gluing the fibers on the nail polish – is unlikely. H and E_r of both samples are averages of at least three different fibers and feature only a slow standard deviation and are, therefore, well reproducible. The mechanical properties of rACF are similar to those of rAF1, but there is no direct comparison for rACF possible, since no classical viscose fibers with both anionic and cationic additives were prepared.

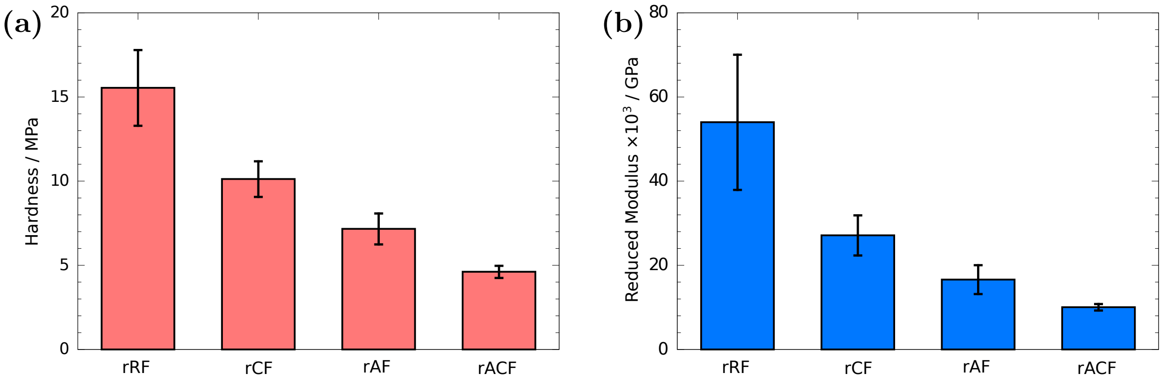

Figure 4.15.: AFM-NI results of swollen rectangular viscose fibers as (a) hardness and (b) reduced modulus.

A different study by F. Weber et al. dealt with the swelling behavior of the classical viscose fibers listed in table 4.6 [23]. There, the geometric swelling was measured by employing an optical microscope and quantified as the swelling ratio s_r:

$$s_r = \frac{d_s}{d_0}, \tag{4.6}$$

with d_s and d_0 denoting the diameter – or width for rectangular fibers – of the swollen and dried fiber, respectively. In figure 4.16, H and E_r of classical viscose fibers are plotted against the swelling ratio. Apparently, cRF, cCF1, and cCF2 swell by approximately the same amount, but differ significantly in their mechanical properties. Both anionic fibers cAF1 and cAF2 clearly swell more than the reference fibers, which is in good agreement with their decreased H and E_r values. It seems that there is a definite relation between the geometrical swelling and the mechanical properties, when inspecting figure 4.16. Such a behavior is to be expected, since geometrical swelling is nothing more than an increase in volume by the uptake of water. This – as discussed in section 4.2 – induces a higher mobility of the cellulose chains and results in a softer material. The effect on the mechanical properties seems to be large for small increases of s_r from the initial value. Increasing s_r further, seems to affect the mechanical properties less and less.

To prove the effectiveness of the additives further, also the swelling of flat, rectangular viscose fibers was characterized [50]. Also these swelling experiments were performed by F. Weber at Graz University of Technology. The results are presented in figure 4.17 and follow in principle the trend observed for classical viscose fibers. A first finding is

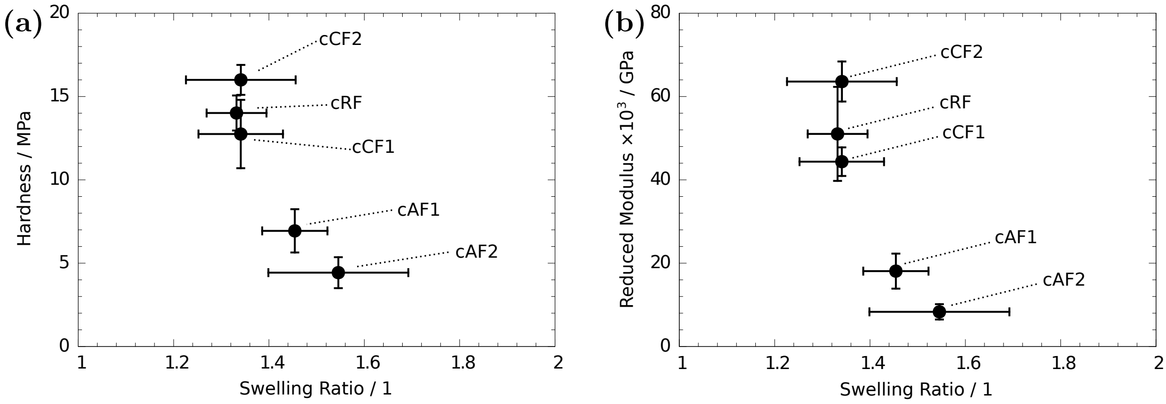

Figure 4.16.: Relation of geometrical swelling to (a) hardness and (b) reduced modulus of classical viscose fibers.

that the unmodified reference rRF as well as the cationic fiber rCF swell less than their classical viscose counterparts. Only rAF is comparable to its classical equivalent. This discrepancy might be caused by the method of detecting the fibers' widths. Flat fibers have a width to thickness ratio of about 40, enabling them to twist easily. Such twists cannot always be detected during the swelling experiment via the optical microscope and will lead to a corruption of the measured widths. Additionally, an anisotropy in swelling might be present, causing the fibers to swell differently in thickness and width. This, however, cannot be detected by the method used here.

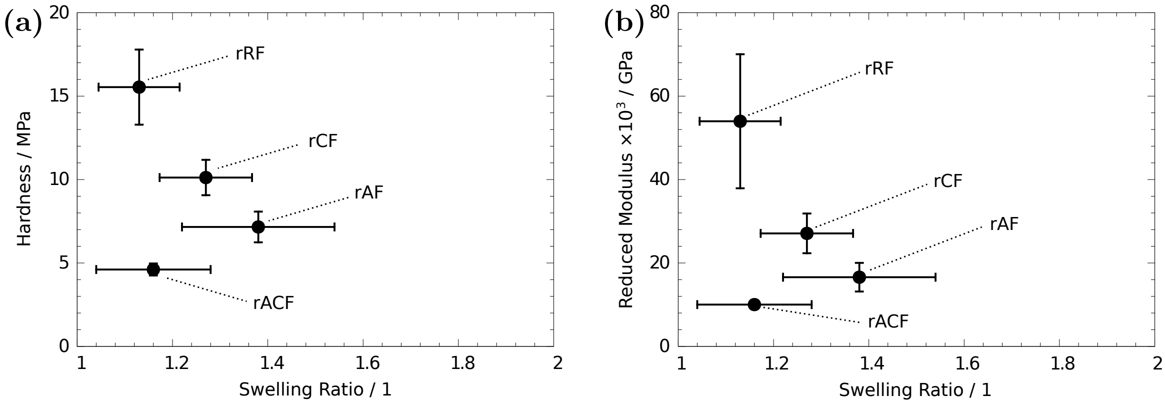

Figure 4.17.: Relation of geometrical swelling to (a) hardness and (b) reduced modulus of rectangular viscose fibers.

Another interesting observation is that rACF swells approximately by the same amount as the unmodified fibers, while being the softest and most compliant rectangular fiber. To compare rACF with the other fibers, the amounts of incorporated CMC and CS have to be considered (see table 3.4). In rACF, less CMC than in rAF is present, whereas the amount of CS is larger than in rCF. If the additives would act synergetically, one would expect a slight increase in swelling accompanied by a moderate reduction in H and E_r. Obviously, this is not the case. There is no information available on how exactly CMC and CS will interact in the cellulose matrix, but it can be expected that both will attract each other and agglomerate due to their opposite charges. This would lead to an effective charge compensation leaving only a small net charge – positive or negative, depending on the absolute amounts – which will naturally have a low effect on the geometrical swelling. The large decrease in H and E_r could be caused by the agglomerated additives which act as impurities and disrupt the cellulose-cellulose interactions locally. To some extent, this effect is expected to be present in all samples.

By combining the samples' morphologies, mechanical properties, and swelling behavior another observation arises. All rectangular viscose fibers exhibited fractal-like trenches, aligned approximately perpendicular to the fibers' main axes. It turns out that these trenches are most pronounced on the hardest fiber rRF and only faintly visible on the softest fiber rACF (compare figures 4.12 and 4.15). A qualitative correlation between the number of pronounced trenches and the fibers' mechanical properties is observed. The swelling, on the other hand, seems to be not correlated to the trenches, since rACF swells by the same amount as rRF while exhibiting no distinctive trenches. A more quantitative investigation of the relation between water uptake, number of trenches, and mechanical properties is currently in progress [92]. Nonetheless, a tentative explanation for the trenches can already be given. During the first drying of the fiber, directly after its production, it will shrink geometrically. The outermost regions will dry faster than the core of the fiber, hence, stresses on the surface are created. Additionally, a longitudinal strain is applied to the fibers during spinning. These stresses could exceed the material's strength and induce localized cracks on the surface. This would explain also the fractal appearance of the trenches, since many fracture surfaces have a fractal character [93,94]. If a fiber is softer and more compliant, it can sustain a larger deformation before breaking and hence less cracks – or trenches – are observed on its surface.

4.3.2. Humidity dependence of mechanical properties

The investigations of cellulose model films revealed that fully swollen films are about 30 times softer and 110 times more compliant than a film at a relative humidity of 0.45 (see table 4.4). To understand the mechanics of bond formation, knowledge of the transition between the dried and fully swollen state of a fiber is needed. In order to record the mechanical properties of viscose fibers as a function of the surrounding air's relative humidity, the setup presented in subsection 3.1.2 was employed. The viscose fibers were embedded in nail-polish in the dried state, as is described in subsection 3.3.3.

The relative humidity φ_r is first decreased to a value between 0.05 and 0.10 as a starting point and then increased step wise. A typical schedule of φ_r is presented in figure 4.18a. To verify if a fiber has reached its equilibrium in swelling, consecutive AFM scans were performed. If the fiber is still taking up water and changing its geometry, a drift will be present in the AFM image. Only when the equilibrium state is reached, no drift is observed and two consecutive AFM scans will be congruent. In figure 4.18b, the temperature evolution during the experiment is shown. An increase from the initial temperature of 28 °C to 34 °C is observed. It has been reported that the temperature has only a minor effect on the ability of cellulosic materials to take up water at constant relative humidity [95–98]. Classical viscose at $\varphi_r = 0.6$, e.g., exhibits a decrease in equilibrium water content by mass from 10 % to 9.7 % when increasing the temperature from 20 °C to 36 °C [97]. A rise in temperature by 6 °C during a 22 h long experiment is, therefore, unproblematic.

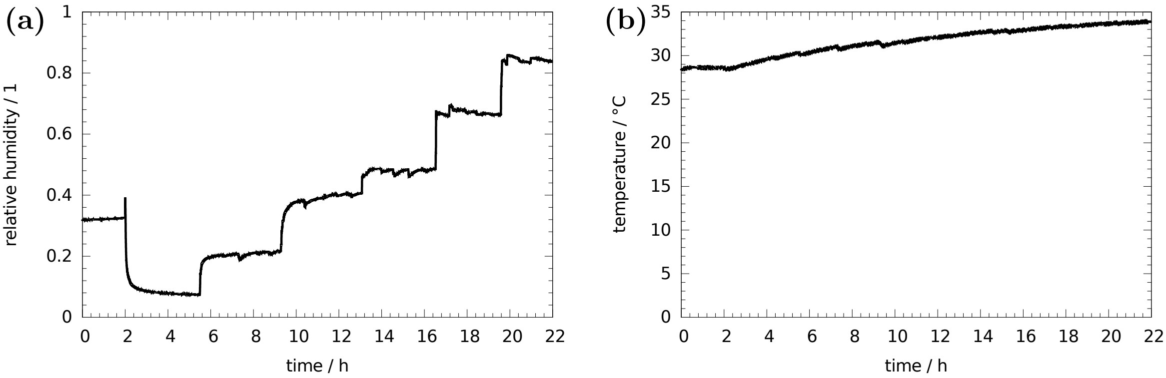

Figure 4.18.: A typical schedule of relative humidity (a) and the temperature change (b) over time in an AFM-NI experiment with controlled relative humidity.

AFM topography images were recorded after AFM-NI, and are presented for single indents at various relative humidities in figure 4.19a. Vertical line profiles, as indicated by the dashed line in the leftmost image of figure 4.19a, are displayed in figure 4.19b. The vertical orientation of the line profiles was chosen for better representation of the indent, which is affected by fiber curvature and the *pile-up* effect discussed below. An example of a horizontal profile is given in figure 4.20. By comparing the depths of the residual indents in figure 4.19, an increase of the depth from around 30 nm to about 50 nm with increasing humidity is found. A similar observation can be made for the widths of the indents, which are approximately 150 nm at $\varphi_r = 0.10$ and which rise to 400 nm at $\varphi_r = 0.94$. Both, depth and width evolution of the indents, indicate a softening of the material with increased φ_r. All indents performed at $\varphi_r < 0.9$ feature a pile-up of material on the left and right sides, as indicated on the second image in figure 4.19a. One possible reason for the occurrence of pile-up only on these two sides, is a lateral force component induced by the bending of the cantilever (and therefore a tilting of the indenter tip) during loading. Another reason could be that the anisotropy of the fibers leads to an aniostropic pile-up effect. The last hypothesis could be verified by indenting a fiber turned by 90° with respect to the cantilever or indenting amorphous cellulose films. If the pile-ups would then be still at the same positions, the influence of the anisotropy can be excluded. This verification, however, was not performed yet, but it is planned to do so.

Pile-up is not accounted for in equation 2.14 and leads to an underestimation of the contact depth z_c and thereby also $A(z_c)$. According to equations 2.4 and 2.7, this will cause an overestimation of H and E_r [99].

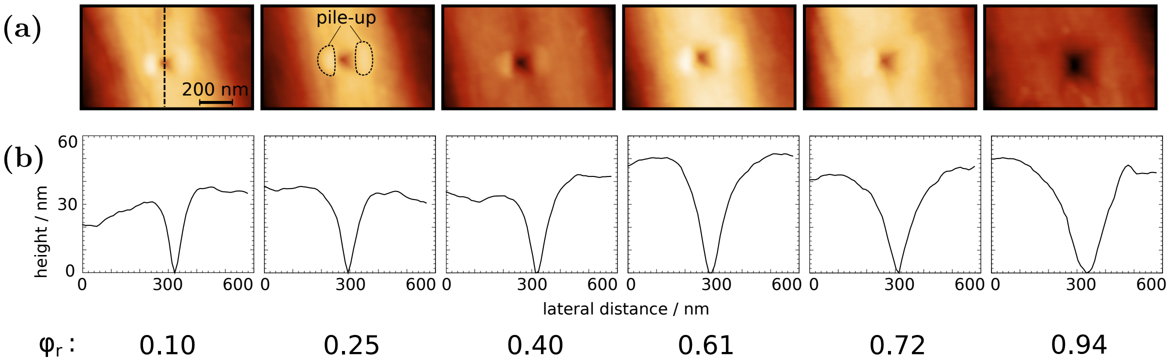

Figure 4.19.: $1\,\mu\text{m} \times 0.6\,\mu\text{m}$ AFM topography images after AFM-NI (a) and vertical line-profiles across the residual indent (b) at various relative humidities, increasing from left to right. The vertical dashed line in (a) denotes the position of the line profiles. The z-scales in (a) are all 120 nm.

In order to correct the measured properties for pile-ups, each indent has to be analyzed individually. The projected pile-up area was approximated as two semi-ellipses, one on both sides of the indents [100]. From line profiles across the indent, the dimensions a, b, and c are extracted as shown in figure 4.20, with a and b denoting the minor radii of the two ellipses and c the common major radius. The minor radii are determined by superimposing a line profile of the indent with one just outside of the indent (blue dashed line in figure 4.20a). When the fiber does not change much, a and b are then given as the difference between the intersection of the two profiles and the maximum of the respective pile-up. To determine c, a profile along the long axis of one of the pile-up regions is extracted (green dashed line in figure 4.20a) and the length of the pile-up is measured according to figure 4.20c. The additional projected area caused by the pile-up, A_{pu}, is then calculated as

$$A_{pu} = \frac{\pi c}{4}(a + b). \tag{4.7}$$

It was found that at low relative humidities, the hardness is overestimated by up to 73 % and the reduced modulus by 32 % when using equation 2.14. At $\varphi_r = 0.84$, the error in H and E_r was 17 % and 8 %, respectively.

The pile-up corrected values for hardness and reduced modulus of four classical viscose fibers (cRF) are presented as a function of relative humidity in figure 4.21. A total of 25 measurements on four different fibers was performed. To illustrate the reproducibility, data points are grouped with respect to the individual fibers by different colors. Surprisingly, both quantities exhibit approximately a linear dependence on φ_r, H much stronger so than E_r. Therefore, by using a linear least squares approach, hardness and reduced modulus were fitted with the models

$$\begin{aligned} H(\varphi_r) &= H_0 + h\varphi_r, \\ E_r(\varphi_r) &= E_{r,0} + e_r\varphi_r. \end{aligned} \tag{4.8}$$

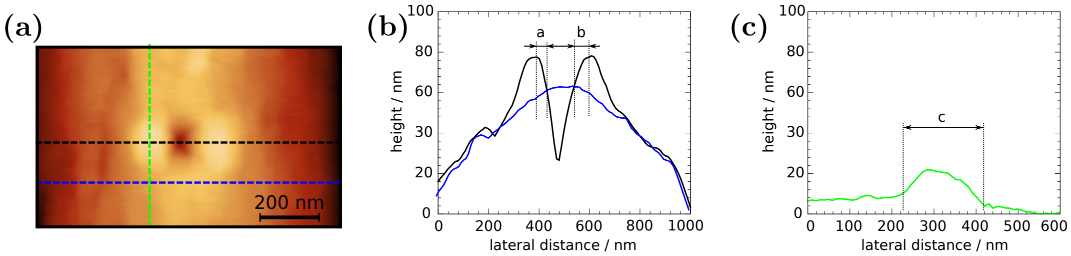

Figure 4.20.: Procedure of pile-up correction in AFM-NI according to [100]. (a) $1\,\mu\text{m} \times 0.6\,\mu\text{m}$ AFM topography image with a z-scale of 100 nm. (b) and (c) are line profiles at positions indicated by the dashed lines with the respective colors in (a).

H_0 and E_0 denote the respective properties at $\varphi_r = 0$, whereas h and e_r describe by how much H and E_r will change from $\varphi_r = 0$ to $\varphi_r = 1$.

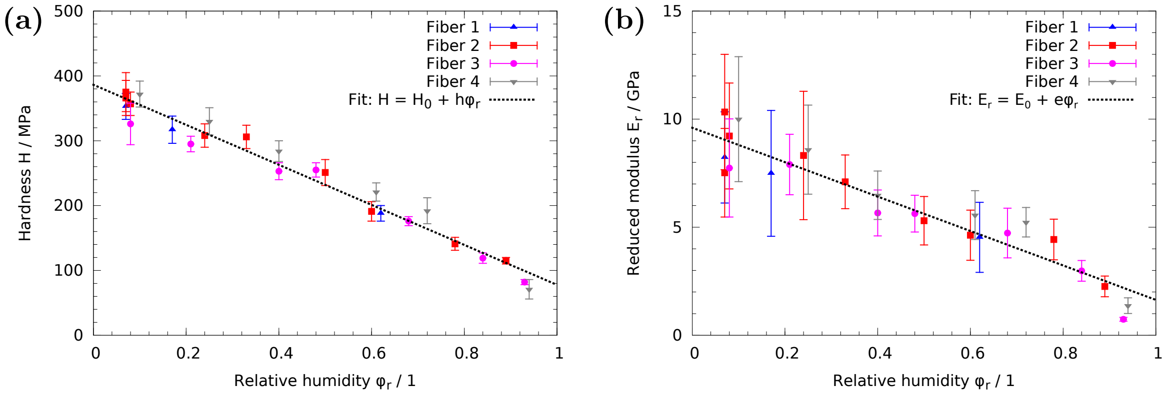

Figure 4.21.: Hardness (a) and reduced modulus (b) of classical viscose fibers as a function of φ_r. All values have been corrected for pile-up.

Fitting equations 4.8 to the data yields

$$\begin{aligned} H(\varphi_r) &= (386 \pm 1)\,\text{MPa} - (309 \pm 1)\,\text{MPa} \cdot \varphi_r, \\ E_r(\varphi_r) &= (9.6 \pm 1.2)\,\text{GPa} - (8.0 \pm 2.3)\,\text{GPa} \cdot \varphi_r. \end{aligned} \tag{4.9}$$

Extrapolating to $\varphi_r = 1$ using the relations 4.9, yields $H(\varphi_r = 1) = (79 \pm 1)\,\text{MPa}$ and $E_r(\varphi_r = 1) = (1.6 \pm 1.5)\,\text{GPa}$. In comparison, the quantities of fully swollen fibers measured in water – according to table 4.6 – are $H_{wet} = (14 \pm 1.0)\,\text{MPa}$ and $E_{r,wet} = (51 \pm 11) \times 10^{-3}\,\text{GPa}$. It appears that compared to the extrapolated values at $\varphi_r = 1$, H and E_r in water are decreased by a factor of 5.5 and 32, respectively. There are in principle three explanations for this. First, the models in equation 4.8 could be physically incorrect. In such a case, extrapolations are likely to fail. Second, H and E_r could jump to lower values when the material is swelling in water. In this case, the prediction for $\varphi_r = 1$ would be correct, but additional effects – only present when the fiber is subjected to bulk water – cause the mechanical properties to decrease further.

The third option would be that both of the cases mentioned above are present at the same time.

The hardness H fits the linear model much better than E_r. Apparently, E_r exhibits a kink at $\varphi_r \approx 0.75$, after which it decreases stronger. When considering the large standard deviations in E_r, it is unclear if the kink is a real phenomenon or caused by random fluctuations. Also, H deviates slightly from the linear behavior at $\varphi \approx 0.95$, but to a lesser extent than the reduced modulus. Both observations could be an indication for a non-linear relation of H respectively E_r with φ_r. Another consideration to take into account arises from water sorption isotherms of cellulosic materials. For this, the relative water content w of a material shall be defined as $w = m_w/m_{dry}$, with m_w denoting the mass of a material with sorbed water and m_{dry} the dry mass. At a given temperature, w is non-linear with regard to φ_r. In figure 4.22, a sorption isotherm of cationic classical viscose fibers is displayed. The curve was recorded with a sorption microbalance, details of the setup are given elsewhere [101,102]. A least squares fit using the Guggenheim-Anderson-de Boer (GAB) [103–105] model is also included in figure 4.22. The GAB model is frequently applied to cellulose materials and other polysaccharides [106] and provides a good fit to the present data.

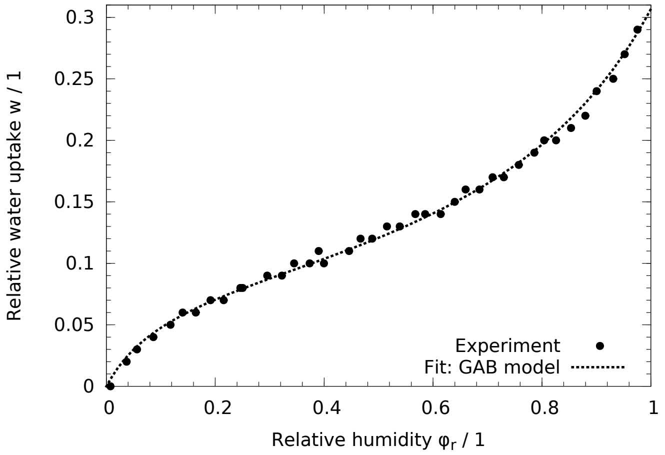

Figure 4.22.: Sorption isotherm of cationic classical viscose fibers. From [107].

In the literature, experimental evidence has been reported that the Young's modulus is proportional to the water content in cellulosic materials [108]. Moreover, an approximately linear relation between the Young's modulus and the water content w for gelatin and starch films [109] as well as for cellulose films [110] had been found. Theoretical considerations, however, state that the Young's modulus E of hydrogen bond dominated solids follows the exponential relation

$$\frac{E(w)}{E_0} = e^{A-Bw}, \tag{4.10}$$

with E_0, A and B being material constants [111]. To check if this relation holds for the data presented in figure 4.21, the relative humidity φ_r was transformed to the water content w using the GAB fit of the isotherm in figure 4.22. Then, H and E_r were fitted with equation 4.10 as well as with a linear model for comparison. The results are presented in figure 4.23. A visual inspection immediately leads to the conclusion that both H and E_r follow a linear behavior rather than equation 4.10. Especially $E_r(w)$ deviates strongly from the exponential fit. Although equation 4.10 was developed to work for any solids which are dominated by hydrogen bonds, an actual verification was only presented for paper sheets, where a good agreement with experimental results was found. For regenerated fibers, a fit with equation 4.10 was performed but not displayed [111].

It has to be considered, however, that in figure 4.23 the reduced modulus is plotted and not the Young's modulus, which might be a cause for the deviation from the theory. Additionally, the sorption isotherm was measured with cationic fibers, whereas the mechanical properties were determined from unmodified fibers. In the previous subsection, however, it was found that cationic fibers swell approximately the same amount as unmodified fibers. Therefore, the influence of using the sorption isotherm from cationic fibers should be minimal.

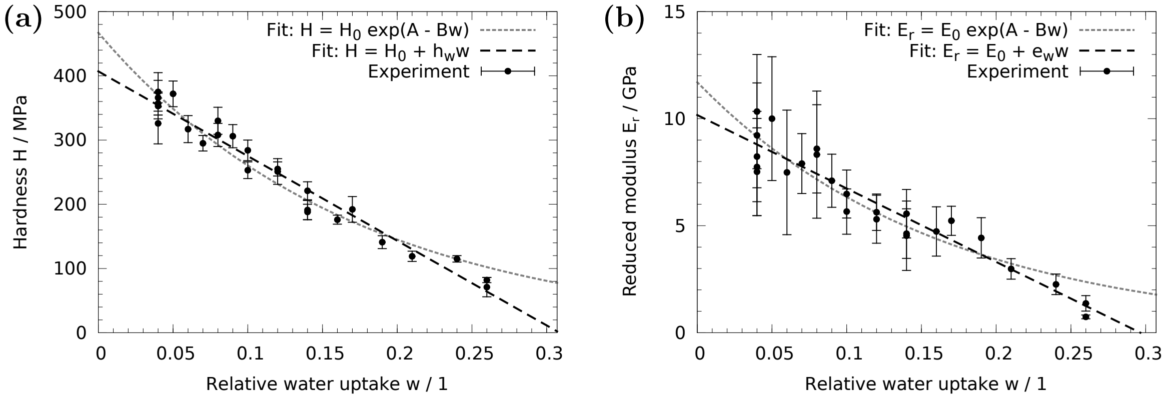

Figure 4.23.: Hardness (a) and reduced modulus (b) as a function of the fibers' water content.

The linear fits in figure 4.23 result in

$$\begin{aligned} H(w) &= (407 \pm 1)\,\mathrm{MPa} - (1319 \pm 5)\,\mathrm{MPa} \cdot w, \\ E_r(w) &= (11.0 \pm 0.5)\,\mathrm{GPa} - (34.3 \pm 3.8)\,\mathrm{GPa} \cdot w. \end{aligned} \tag{4.11}$$

The water content at $\varphi_r = 1$ is $w = 0.307$, which leads to the extrapolations according to equations 4.11: $H(w = 0.307) = (2 \pm 1)\,\mathrm{MPa}$ and $E_r(w = 0.307) = (-0.4 \pm 0.8)\,\mathrm{GPa}$. These results might not seem as good as predictions from equation 4.9, since the reduced modulus at $\varphi_r = 1$ would be negative. However, it can also be interpreted in such a way that H and E_r become very soft at high humidities and only due to statistical errors, a negative modulus is predicted. This is supported by the large error, which is twice the actual value for $E_r(w = 0.307)$.

Another interesting observation is that the ratio $\lambda = \frac{E_r}{H}$ is mostly independent of φ_r, as is demonstrated in figure 4.24. It was found that λ obeys the value of 23.8 ± 4.2, when H and E_r are measured in humid air. Fully swollen fibers in water exhibit a ratio λ_{H_2O} of only 3.64 ± 0.85. This means that the reduced modulus is decreasing in water by an order of magnitude more than the hardness. At high humidities, λ seems to decrease slightly, which is a natural effect of the kink in E_r that is observed at $\varphi_r \approx 0.75$ in figure 4.21b. One data point at $\varphi_r = 0.93$ is 9 ± 1, which is the lowest value observed in air. This could be a hint that the reduced modulus in humid air is already directed towards very low values, which it will finally achieve in the fibers' fully swollen state.

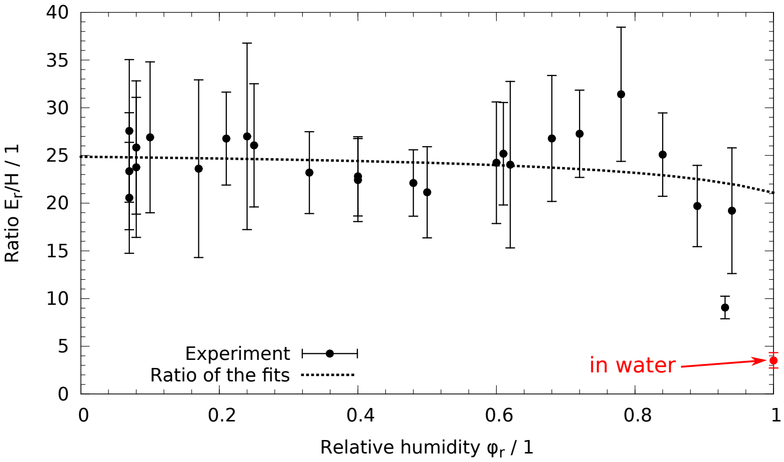

Figure 4.24.: The ratio between reduced modulus E_r and hardness H plotted vs. the relative humidity φ_r. The dashed line is the ratio of the line fits according to equation 4.9.

Hardness and reduced modulus of viscose fibers are strongly affected by the relative humidity of the surrounding medium. An approximately linear relationship with φ_r was found for H and E_r. Surprisingly, both quantities seem also to depend linearly on the relative water content w, although, φ_r and w are not linearly related. The reason for this is that due to the scattering of the data – even if it is low for H – a non-linearity is not detectable. To compare both models (equations 4.11 and 4.9), the corresponding results of the fits are displayed in table 4.7.

Table 4.7.: Comparison of the fits in equations 4.9 and 4.11.

Eq.	$H_1^{\dagger}$ MPa	$E_{r,1}^{\dagger}$ GPa	$\frac{H_0}{H_1}$ 1	$\frac{E_{r,0}}{E_{r,1}}$ 1	$\frac{H_0}{H_{wet}}$ 1	$\frac{E_{r,0}}{E_{r,wet}}$ 1
4.9	79 ± 1	1.6 ± 1.5	4.9 ± 0.1	6.0 ± 5.7	28 ± 2.0	190 ± 47
4.11	2 ± 1	-0.4 ± 0.8	200 ± 100	-28 ± 55	29 ± 2.0	220 ± 48

† The index "1" is shorthand for $\varphi_r = 1$ or $w = 0.307$, respectively.

To approximate the fully dried state, equation 4.9 will be used from now on, since this fit yields slightly lower and thus more conservative values than equation 4.11. For fully swollen fibers, no approximations are needed, because their mechanical properties were directly determined by AFM-NI. Apparently none of the two presented models yield good predictions for fully wet fibers. However, equation 4.11 describes H and E_r at high water contents at least qualitatively, provided that $w = 0.307$ and the presence of bulk water are comparable states. Due to the negative values, however, an interpretation is rendered difficult and for further comparison, equation 4.9 will be used also in this case.

4.3.3. Creep behavior

During the holding time at the maximum load P_{max} in an AFM-NI experiment, a continuous increase of the indentation depth z_i is noticed. This is represented by the horizontal lines at the highest points in, e.g., figure 4.13. This effect is caused by creeping, a typical behavior for viscoelastic materials. Due to the fact that the indenter's area function $A(z_i)$ is increasing with z_i but P_{max} is held constant, the applied stress will decrease. Such a behavior is different from the classical creep effect, where the stress is constant. Nonetheless, a quantitative evaluation of nanoindentation creep would be possible if P - z_i would have been recorded with varying P_{max} [112]. This quantitative investigation of creep effects, however, has not been performed in the present work.

In figure 4.25, the change of z_i due to creep is plotted as a function of φ_r. While no material parameters can be extracted from such a plot, it is an indication for the change in viscoelastic properties of cellulose fibers with relative humidity.

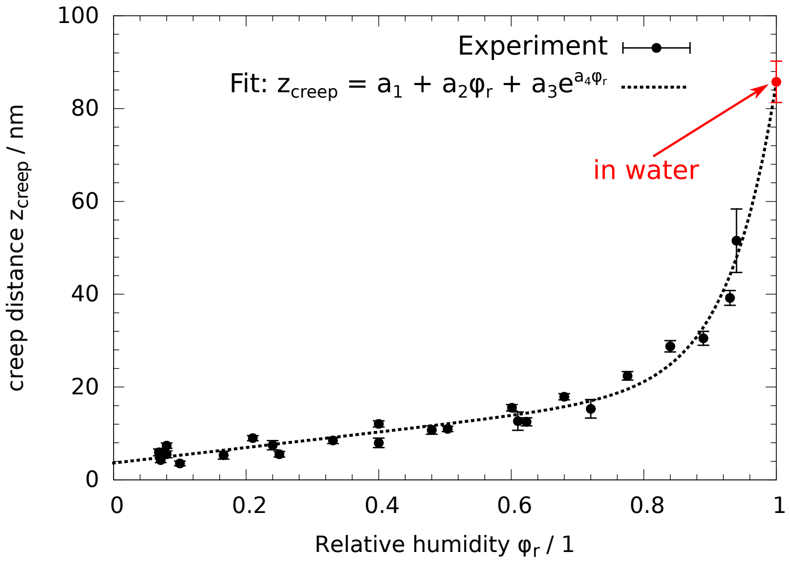

Figure 4.25.: Viscoelastic creep of classical viscose as a function of relative humidity, obtained by AFM-NI with a constant load of $P_{max} = 10\,\mu$N.

The creep distance z_{creep} follows an empirical relation with the relative humidity:

$$z_{creep}(\varphi_r) = a_1 + a_2\varphi_r + a_3 e^{a_4\varphi_r}, \tag{4.12}$$

with $a_1 = 3.63\,\text{nm}$, $a_2 = 16.7\,\text{nm}$, $a_3 = 7.09 \times 10^{-5}\,\text{nm}$, and $a_4 = 13.7$, determined by a non-linear Levenberg-Marquardt least squares fit.

Also, a value extracted from fibers fully swollen and measured in water was added in figure 4.25 and included in the fit. The creep distance of fully swollen fibers matches the other data quite well. Apparently, no additional creep effects take place when a viscose fiber is placed in water for swelling and equation 4.12 is valid for humid materials as well as those subjected to bulk water. This would support the hypothesis that mechanical properties of cellulosic materials decrease with a smooth transition from the humid to the fully wet state. However, the strongest decrease might take place between $0.95 < \varphi_r < 1.0$, an interval which is not accessible using the humidity controlled AFM-NI setup.

4.4. Pulp fiber swelling

Never dried pulp fibers are known to exhibit a very smooth surface [25]. Only when the fibers dry, the surface becomes wrinkled and rough. This is demonstrated in figure 4.26. An AFM topography image of a pulp fiber, recorded in water, is presented in figure 4.26a. Single microfibrils are clearly visible. In figure 4.26b, an AFM scan of a fiber that has been dried is shown. Wrinkles, aligned approximately parallel to the fibers main axis dominate the surface morphology.

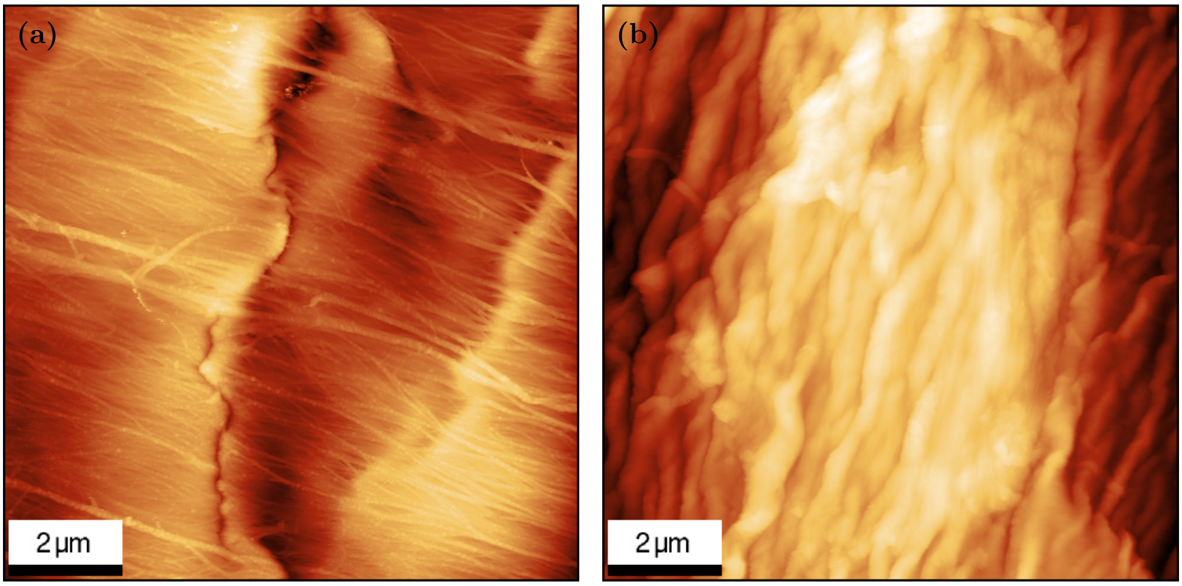

Figure 4.26.: $10\,\mu\text{m}\times 10\,\mu\text{m}$ AFM topography scans of (a) a never dried pulp fiber in water, z-scale: 500 nm and (b) a different pulp fiber after drying, z-scale: $1\,\mu\text{m}$. The fibers' long axes are approximately vertically aligned. From [83].

It is possible that when a pulp fiber is swelling, water will incorporate between the microfibrils and increase the fibril-fibril separation. Additionally, the fibrils' diameter will rise due to water uptake. Both effects would then lead to an enhanced visibility of microfibrils on swollen pulp fibers.

Utilizing the setup to control relative humidity, the surface topography of pulp fibers at varying humidities was recorded by AFM. This investigation allowed to monitor the evolution of the fibers' surface structures with relative humidity. Such changes in surface morphology are directly related to the swelling of the fibers. The study was carried out on three unbleached softwood kraft pulp fibers which were prepared according to subsection 3.3.2. One fiber was glued in its never dried state and dried only after the fixation, while the other two were glued after having been dried without restrictions. Optical microscopy images of these fibers are displayed in figure 4.27. The fiber prepared in the never dried state – figure 4.27a – is perfectly straight and appears macroscopically uniform. If a pulp fiber is allowed to dry freely, it will twist and take a typical shape that is presented in figure 4.27b.

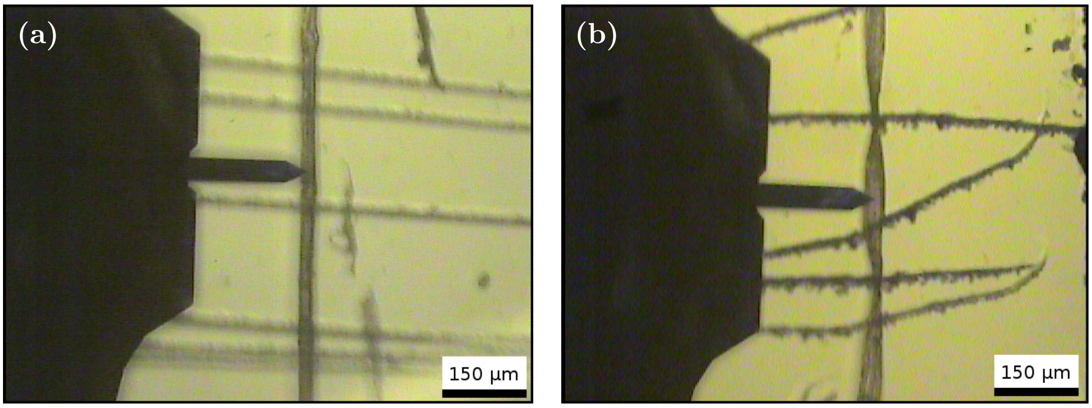

Figure 4.27.: Optical microscopy image of (a) a pulp fiber fixed in the never dried state and (b) one that was dried before fixation. The random scratches on the substrate were used as an orientation guide.

The swelling behavior was characterized by recording AFM images at various relative humidities $0.04 < \varphi_r < 0.84$ and measuring the distance between two surface wrinkles as well as their heights. In figure 4.28, AFM topography images which were recorded on a fiber that had been prepared in its never dried state are shown. The scans were performed at $\varphi_r = 0.06$ and $\varphi_r = 0.82$. It is apparent that at higher humidities (figure 4.28b), the surface wrinkle's separation is increased compared to the dried state (figure 4.28a).

The wrinkle distance $d(\varphi_r)$ is determined by extracting two to five line profiles from an AFM topography image and measuring the distance between the maxima of two – not necessarily adjacent – wrinkles, as is illustrated in figure 4.29. A wrinkle's height is gained by averaging the wrinkle height on both sides, i.e., $h(\varphi_r) = \frac{1}{2}[h_1(\varphi_r) + h_2(\varphi_r)]$. According to figure 4.29, $h_1(\varphi_r)$ and $h_2(\varphi_r)$ denote the height at a certain relative humidity φ_r on the left and right side of the wrinkle, respectively.

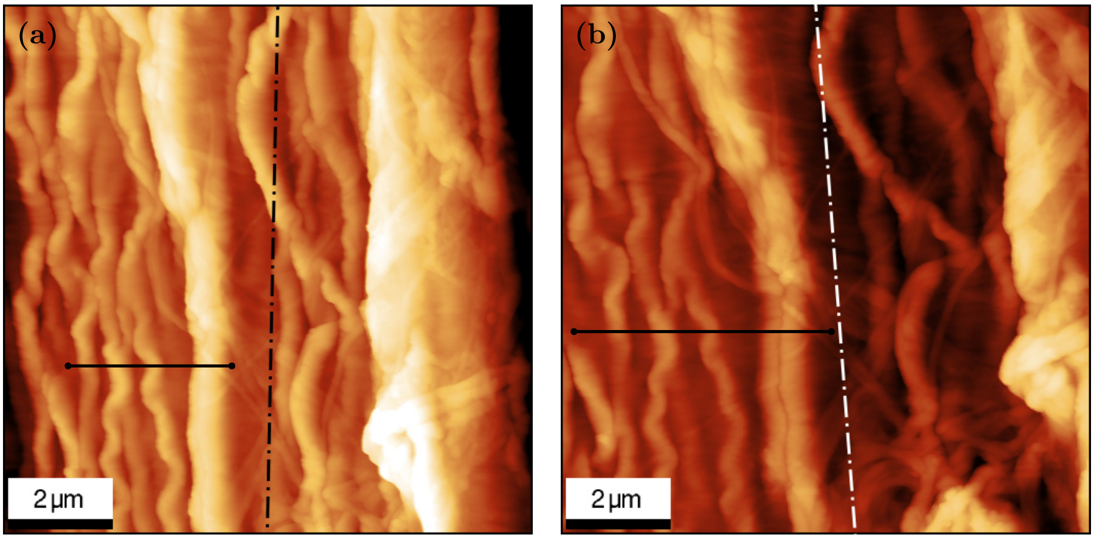

Figure 4.28.: 10 μm×10 μm AFM topography image of a pulp fiber that was fixed in its never dried state at (a) $\varphi_r = 0.06$ and (b) $\varphi_r = 0.82$. The z-scale is 1 μm for both images. The dot and dash lines indicate the fiber's long axis and the horizontal solid lines mark the position of the profiles presented in figure 4.29.

To compare the change in wrinkle distance and height between independent profiles, the relative changes with respect to the initial values are calculated:

$$\begin{aligned} r_d(\varphi_r) &= \frac{d(\varphi_r) - d(0)}{d(0)}, \\ r_h(\varphi_r) &= \frac{h(\varphi_r) - h(0)}{h(0)}. \end{aligned} \tag{4.13}$$

The initial values $d(0)$ and $h(0)$ were approximated by the values measured at the lowest reachable humidity, i.e., $\varphi_r \approx 0.06$, as is indicated in figure 4.29a.

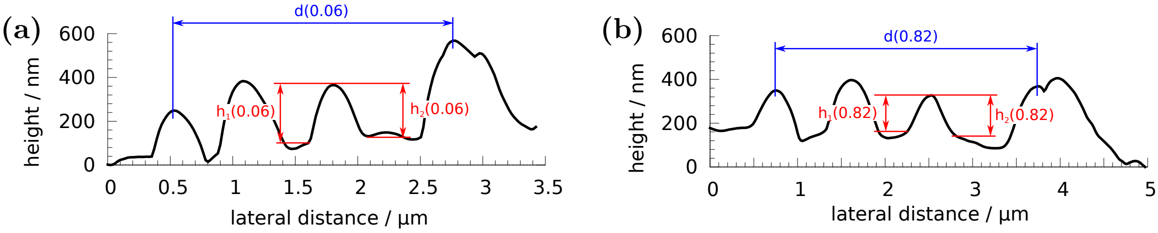

Figure 4.29.: Line profiles extracted from figure 4.28 at (a) $\varphi_r = 0.06$ and (b) $\varphi_r = 0.82$. Exemplary wrinkle distances and wrinkle heights are indicated by the blue and red lines, respectively.

Plots of the relative change in wrinkle distance and height versus relative humidity are presented in figure 4.30. The presented data were obtained from two independent positions of the pulp fiber. As expected, the wrinkle distance increases with increasing φ_r while the wrinkle height decreases.

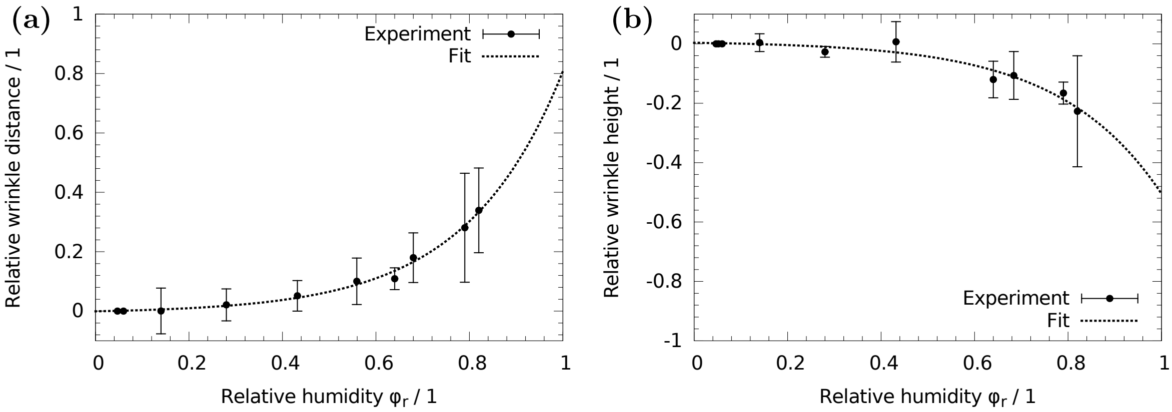

Figure 4.30.: Relative change of (a) wrinkle distance and (b) wrinkle height with relative humidity of a pulp fiber prepared in its never dried state.

Both quantities seem to follow an exponential relation of the form

$$r(\varphi_r) = a_1 + a_2 e^{a_3 \varphi_r}, \tag{4.14}$$

which provided a good fit, as is illustrated by the dashed lines in figure 4.30. This fit would predict a change in wrinkle distance of approximately 80 % at $\varphi_r = 1$ and a decrease in wrinkle height by 50 %.

An unexpected result was found for pulp fibers which were dried before gluing them to the sample holder. Almost no change in wrinkle distance and wrinkle height could be detected. AFM topography images obtained on such fibers are presented in figure 4.31.

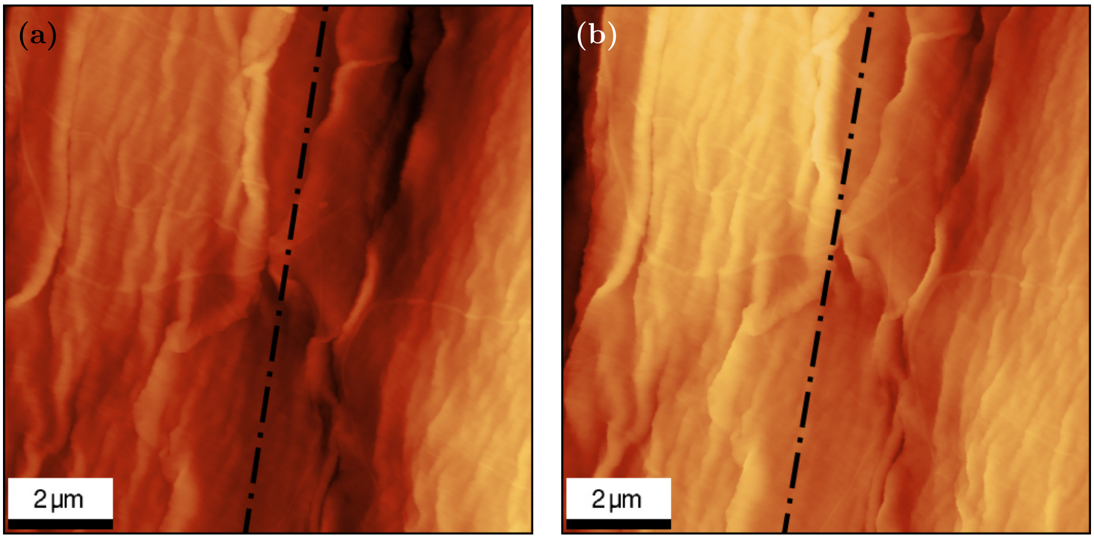

Figure 4.31.: $10\,\mu$m×$10\,\mu$m AFM topography of a pulp fiber that was fixed after drying freely at (a) $\varphi_r = 0.05$ and (b) $\varphi_r = 0.80$. The z-scale in both images is $1.5\,\mu$m. The dot and dash lines indicate the fiber's long axis.

The relative humidity in figure 4.31a was $\varphi_r = 0.05$ and in figure 4.31b $\varphi_r = 0.80$. Except a slight shift of the images' positions, no change in the morphology is apparent. The relative change in wrinkle distance was measured on both fibers at altogether six positions, the change in wrinkle height only at one position. Both quantities are plotted in figure 4.32 and confirm that on these fibers the wrinkles appear to be not influenced by φ_r. Even at high humidities of $\varphi > 0.8$, no significant increase of r_d or decrease of r_h is detected.

A hypothesis for this behavior is that the method of sample preparation has an influence. Due to the twisting of the fiber during drying, large scale plastic deformations could occur which hinder the dewrinkling of the fibers. It is an experimental fact that non-reversible deformations occur when a fiber is drying, i.e., if a fiber has twisted, it will not untwist, even when it is placed in water. However, the plastic deformation could be a localized effect, meaning that it should be possible to find positions on a fiber which exhibit significant dewrinkling upon water uptake. Indications for this are two data points in figure 4.32a, which have a value of about 0.07 – or 7 % – at humidities of $\varphi_r = 0.55$ and $\varphi_r = 0.80$. This is by far not a prove for localized dewrinkling, a more thorough investigation would have to be conducted to ascertain such a behavior.

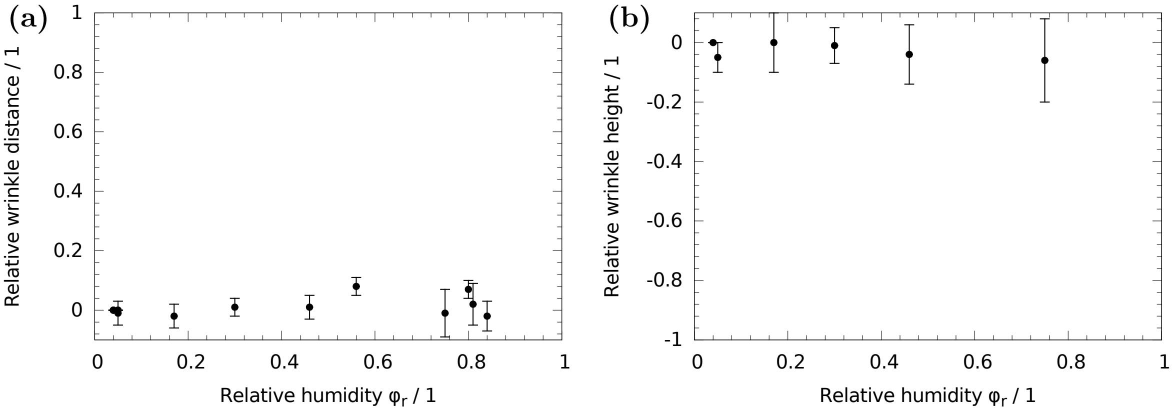

Figure 4.32.: Wrinkle distance (a) and wrinkle height (b) dependence on relative humidity of freely dried fibers.

4.5. Mechanical properties of pulp fibers

The mechanical properties of pulp fibers were characterized as humidity dependent H and E_r, using AFM-NI and the setup to control relative humidity inside the AFM's fluid cell. In accordance with the previously described investigation of viscose fibers, hardness and reduced modulus are presented as a function of relative humidity φ_r, including the fully wet state. Additionally, the creep behavior at varying φ_r will be given as the increase of indentation depth at a constant applied force.

4.5.1. Humidity dependence

For these AFM-NI investigations, softwood kraft pulp fibers were glued on a drop of nail polish after they were dried in air, as is described in subsection 3.3.2.

As was seen in the previous section, pulp fiber surfaces exhibit a rough and wrinkled surface topography. It is, therefore, possible that tip-sample dilation will obscure parts of the surface which are then also not accessible for AFM-NI. Figure 4.33 depicts this effect. In an area such as region I in figure 4.33a, no AFM-NI can be performed. Only areas such as region II will be flat enough to place indents and extract useful nanomechanical information. An actual AFM topography image with severe dilation effects at the left border is presented in figure 4.33b. The upper right region of the image, however, was flat enough to place indents.

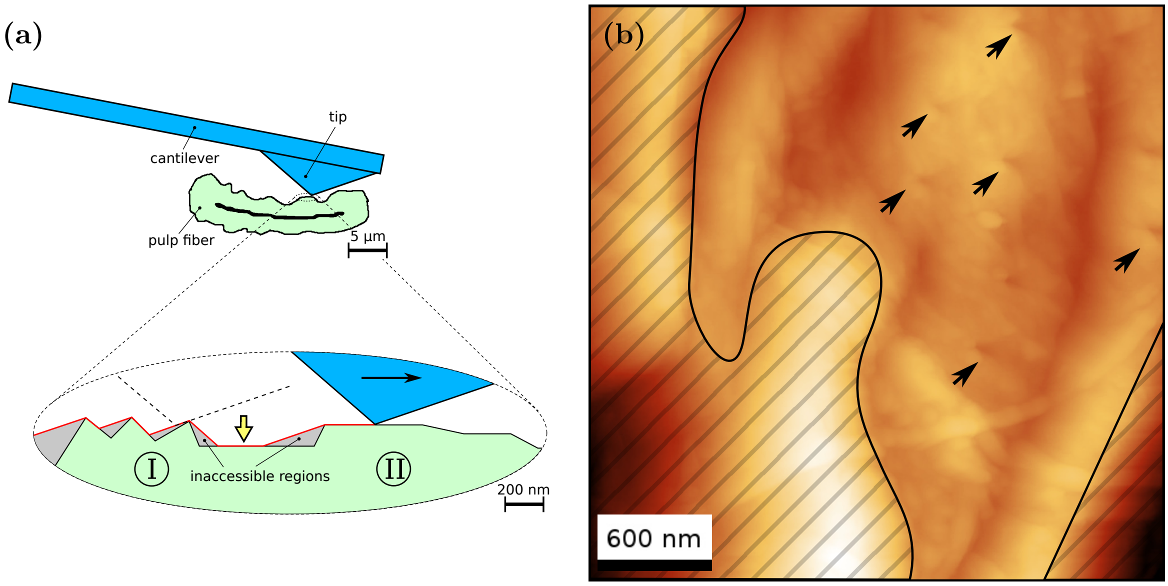

Figure 4.33.: The effect of tip-sample dilation on topography images recorded on pulp fiber surfaces with AFM-NI probes. (a) Schematic illustration and (b) dilation (marked by the shaded areas) on an actual AFM topography image. Arrows indicate residual AFM-NI imprints. (Modified from [38].)

Initial AFM-NI investigations on kraft pulp fibers – as well as cellulose films, see section 4.2 – were performed by using three-sided pyramidal tips (ND-DTIRS) as indenters. Later, these tips were no longer produced by the manufacturer and four-sided pyramidal tips (ND-DYIRS) were used as a replacement. To allow a comparison of pulp fibers with viscose fibers, H and E_r were also determined by using the four-sided tips. The four-sided tips lead to pile-up also on pulp fiber surfaces, hence a correction [100] of the values was necessary. Unfortunately, due to the rough structure of the pulp fiber surfaces, the pile-up could not be determined directly with the method used for viscose fibers. Therefore, the average of the pile-up area determined on viscose fibers was used to correct the values of pulp fibers. Taking the average pile-up area is justified since the area did not depend strongly on φ_r.

AFM-NI revealed that H and E_r of pulp fibers were decreasing with increasing relative humidity, in a similar manner as was observed for viscose fibers. The results are visualized in figure 4.34. The hardness seems again to follow a linear trend, whereas the reduced modulus seems to decrease faster at higher humidities. It is apparent that the tip shape has a significant influence on H and E_r, with E_r being affected the strongest.

Again, a linear fit for H and E_r with the model in equation 4.8 was performed for results obtained with four-sided tips as well as those obtained by three-sided tips. The hardness is then

$$\begin{aligned} H^{(3)}(\varphi_r) &= (270 \pm 1)\,\mathrm{MPa} - (243 \pm 1)\,\mathrm{MPa} \cdot \varphi_r, \\ H^{(4)}(\varphi_r) &= (350 \pm 1)\,\mathrm{MPa} - (276 \pm 1)\,\mathrm{MPa} \cdot \varphi_r, \end{aligned} \tag{4.15}$$

with $H^{(3)}$ and $H^{(4)}$ describing the fits for three-sided and four-sided tips, respectively. Similarly, the fits for the reduced moduli resulted in

$$\begin{aligned} E_r^{(3)}(\varphi_r) &= (3.2 \pm 1.4)\,\mathrm{GPa} - (3.0 \pm 2.4)\,\mathrm{GPa} \cdot \varphi_r, \\ E_r^{(4)}(\varphi_r) &= (6.9 \pm 2.2)\,\mathrm{GPa} - (5.2 \pm 3.8)\,\mathrm{GPa} \cdot \varphi_r. \end{aligned} \tag{4.16}$$

According to the errors of the parameters in equations 4.15 and 4.16 it is confirmed that the hardness follows the linear model to a higher extent than the reduced modulus. This seems true for both tip shapes.

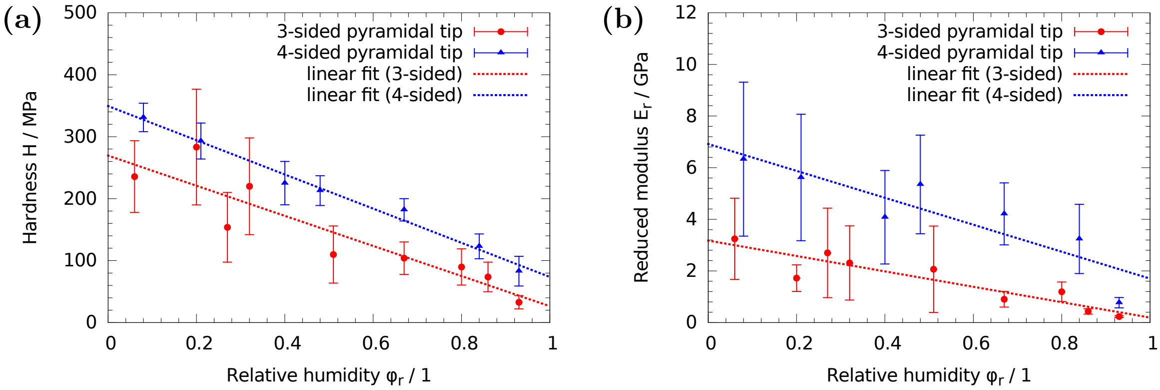

Figure 4.34.: Hardness (a) and reduced modulus (b) of pulp fibers as a function of relative humidity. Values determined by using a three-sided pyramidal tip are plotted as red circles and those obtained by four-sided tips as blue triangles.

Also, the mechanical properties of fully swollen fibers were determined using both tip shapes and are presented in table 4.8, for easy comparison. While the determined moduli are similar between the three- and four-sided tips, the hardness values are different. However, the large standard deviation of $H_{wet}^{(4)}$ decreases the significance a bit. This is emphasized with the ratios $H_{wet}^{(4)}/H_{wet}^{(3)}$ and $E_{r,wet}^{(4)}/E_{r,wet}^{(3)}$, also listed in table 4.8.

Table 4.8.: Hardness and reduced modulus of kraft pulp fibers determined on fully swollen fibers in water.

tip shape	H_{wet} MPa	$E_{r,wet}$ GPa	$H^{(4)}_{wet}/H^{(3)}_{wet}$ 1	$E^{(4)}_{r,wet}/E^{(3)}_{r,wet}$ 1
3-sided	2.7 ± 0.7	$(32 \pm 6) \times 10^{-3}$	2.6 ± 1.2	1.4 ± 0.6
4-sided	6.9 ± 2.8	$(46 \pm 17) \times 10^{-3}$		

In analogy with viscose fibers, the ratio $\lambda = \frac{E_r}{H}$ was calculated from the results obtained with four-sided tips and plotted in figure 4.35 against the relative humidity. The average value for λ is 20.1 ± 5.7 and seems to decrease for higher humidities. In water, $\lambda_{H_2O} = 6.7 \pm 3.7$ which is similarly low as the value for viscose fibers. Interestingly, the ratio at $\varphi_r = 0.93$ is almost as low as the one of the fully swollen fiber.

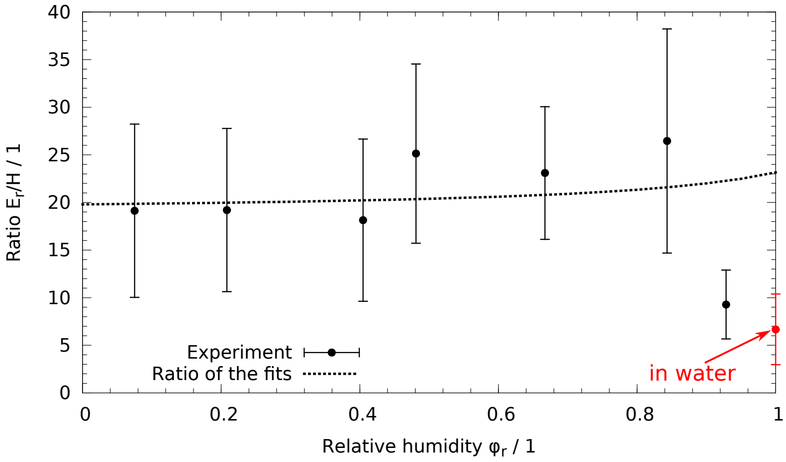

Figure 4.35.: The ratio $\lambda = E_r/H$ as a function of relative humidity, obtained by four-sided pyramidal tips. The dashed line indicates the ratio of the linear fits.

The elastic modulus of softwood pulp fibers in the fully wet state using AFM based methods, has been reported several times in the literature. By applying loads in the order of approximately 50 nN, values for E_r of $\approx 10 \times 10^{-3}$ GPa [47] and $\approx 5 \times 10^{-3}$ GPa, with a maximum value of 50×10^{-3} GPa [48] were determined. In both cases, fully elastic behavior was assumed. More recently, an AFM-NI approach similar to the one presented in this work was also applied to investigate softwood pulp in the wet state, where a reduced modulus of $E_r = (182 \pm 50) \times 10^{-3}$ GPa and a hardness of $H = (140 \pm 38)$ MPa was found [37]. In all three works, standard AFM tips – designed for topography measurements – were used. The first of the listed works relied on an estimation of the tip radius [47], the second assumed a perfectly conical indenter [48] and the third reports a tip characterization using SEM [37]. In summary, literature values for E_r of wet kraft pulp fibers are reported to be several times lower or higher as the values presented here. These discrepancies could be caused by the different ways of taking the tip geometry into account and also by the applied evaluation procedures, which assumed either elastic or elastic-plastic behavior. Additionally, there is an effect of the tip shape itself, as was discussed above and is clearly visible in figure 4.34.

4.5.2. Creep behavior

Nanoindentation creep was determined in the same way as for viscose fibers, by extracting the change of the indentation depth between the start and the end of the holding time at P_{max}. The results – obtained by four-sided pyramidal tips – are presented in figure 4.36. Equation 4.12 was again used to fit the data by a Levenberg-Marquardt least squares fit, which is also plotted in figure 4.36. The fit coefficients resulted in $a_1 = 3.28\,\mathrm{nm}$, $a_2 = 24.1\,\mathrm{nm}$, $a_3 = 9.50 \times 10^{-12}\,\mathrm{nm}$, and $a_4 = 29.3$.

These values for z_{creep} recorded on pulp fibers seem to increase linearly in the humidity range $0.05 < \varphi_r < 0.93$. Only in the fully swollen state a stronger increase is observed. It is possible that pulp fibers behave in this regard differently from viscose fibers and do not change the mechanical properties continuously from the humid to the fully wet state. On the other hand, only seven data points were recorded for pulp fibers, whereas 25 data points were obtained on viscose fibers. Additional measurements, performed at higher humidities ($\varphi_r > 0.7$) would clarify the exact creep behavior of pulp fibers.

This evaluation was also applied to P - z_i plots obtained by three-sided pyramidal tips, but the results are not shown here. There, a similar relation as the one presented in figure 4.36 is observed. Only the scattering of the data is much higher, leading to a less clear trend.

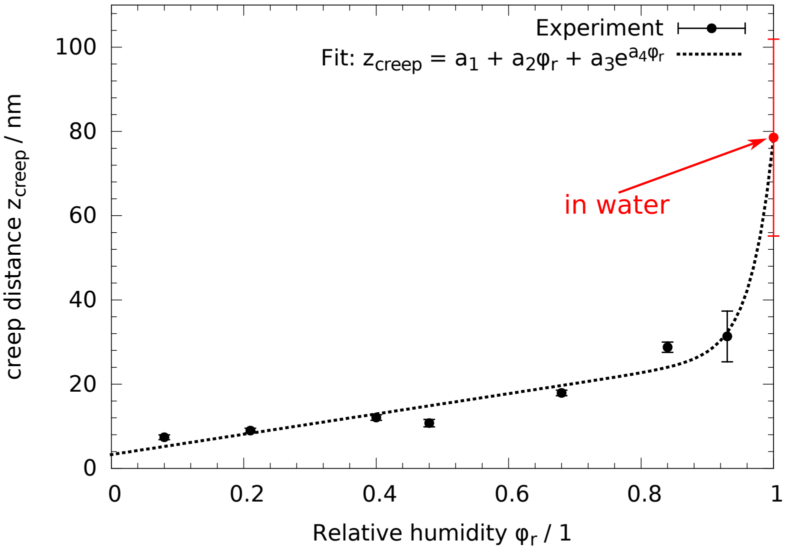

Figure 4.36.: AFM-NI creep as a function of relative humidity at a constant load $P_{max} = 10\,\mu\mathrm{N}$. The red data point at $\varphi_r = 1$ was obtained on a fully swollen fiber in water, using a four-sided pyramidal tip.

4.6. Comparison

In this section, a comparison between the mechanical properties of cellulose films, viscose fibers, and kraft pulp fibers is presented. A summary of all data for H and E_r is compiled in tables 4.9 and 4.10, respectively. The common fact for all materials investigated in this work is that their mechanical properties depend strongly on the relative humidity of the surrounding environment. All materials, however, have inherent traits which will be discussed in the following by comparing them with pulp fibers. The reason for choosing pulp fibers as the reference is twofold. First, pulp fibers were the driving force that initiated this work and are industrially the most important ones. Second, only pulp fibers were thoroughly characterized using both, three-sided and four-sided tips.

Table 4.9.: Comparison of characteristic hardness values for all materials investigated in this work. Only unmodified materials are listed.

material	tip shape†	H_0 MPa	$H_{0.5}{}^{\ddagger}$ MPa	H_{wet} MPa	H_0/H_1 1	H_0/H_{wet} 1
Cellulose films	(3)	-	190 ± 24	6.0 ± 0.3	-	$32 \pm 4.3^{*}$
Viscose fibers	(4)	386 ± 1	250 ± 20	14 ± 1.0	4.9 ± 0.1	28 ± 2.0
pulp fibers	(3)	270 ± 1	110 ± 46	2.7 ± 0.7	10 ± 0.2	100 ± 25
	(4)	350 ± 1	213 ± 24	6.9 ± 2.8	4.7 ± 0.1	51 ± 21

† (3) ... three-sided pyramid, (4) ... four-sided pyramid

‡ Obtained from a single data point measured at $\varphi_r = 0.5 \pm 0.05$.

* The ratio is in this case $H_{0.5}/H_{wet}$, since H_0 is not available.

Table 4.10.: Comparison of characteristic reduced modulus values for all materials investigated in this work. Only unmodified materials are listed.

material	tip shape†	$E_{r,0}$ GPa	$E_{r,0.5}{}^{\ddagger}$ GPa	$E_{r,wet}$ GPa	$E_{r,0}/E_{r,1}$ 1	$E_{r,0}/E_{r,wet}$ 1
Cellulose films	(3)	-	6.3 ± 1.0	$(56 \pm 2) \times 10^{-3}$	-	$113 \pm 18^{*}$
Viscose fibers	(4)	9.6 ± 1.2	5.3 ± 1.1	$(51 \pm 11) \times 10^{-3}$	6.0 ± 5.7	190 ± 47
Pulp fibers	(3)	3.2 ± 1.4	2.1 ± 1.7	$(32 \pm 6) \times 10^{-3}$	17 ± 118	100 ± 48
	(4)	6.9 ± 2.2	5.4 ± 1.9	$(46 \pm 17) \times 10^{-3}$	4.1 ± 5.3	150 ± 73

† (3) ... three-sided pyramid, (4) ... four-sided pyramid

‡ Obtained from a single data point measured at $\varphi_r = 0.5 \pm 0.05$.

* The ratio is in this case $E_{0.5}/E_{wet}$, since E_0 is not available.

A direct comparison of cellulose films and viscose fibers is omitted, since these two materials were characterized using tips with a different shape. However, it should be noted that viscose fibers and amorphous cellulose films are expected to be very similar. Mainly, because both are regenerated cellulose, with viscose fibers exhibiting a large amorphous fraction of about 70 %.

4.6.1. Viscose fibers vs. pulp fibers

Viscose fibers are harder than pulp fibers, especially in the fully swollen state. The reduced moduli, however, seem to be quite comparable and deviate only at low humidities. The reason for this could be explained by the structural differences of both materials. Wood fibers are composed of cellulose microfibrils which are held together by hemicelluloses and lignin [14]. During pulping, the latter two components are extracted from the fibers, leaving cellulose fibrils which are weaker bound than before. If water is added to the fibers, the bonds between the fibrils are weakened even more, which results in an increase of the fibril-fibril separation (see figure 4.26). Indenting into the fiber will lead to plastic deformation, which is enhanced by the ability of the microfibrils to rearrange easier due to weakened fibril-fibril bonds. Viscose fibers also exhibit fibrils which are, however, embedded in a matrix of amorphous cellulose [113]. When adding water to a viscose fiber, the material will swell, but there is no reason for the fibrils to detach from the matrix. An applied load will also lead to plastic deformation, if it is high enough, but due to the fact that the material is more or less homogeneous there is no enhancement of plastic deformation other than swelling. Since hardness is a measure for tensile strength, it is to some extent influenced by plasticity. Hence, in comparison to pulp fibers a higher hardness is observed for viscose fibers.

The reduced modulus is related to the Young's modulus and is a purely elastic property. Moreover, E_r is determined from the unloading part of an AFM-NI experiment. In this state, the material has already been deformed plastically and the initial response upon unloading is elastic [36]. Since both, viscose and pulp fibers, are mainly composed of cellulose the elastic response should be similar, as is observed.

4.6.2. Cellulose films vs. pulp fibers

Cellulose films are harder and less compliant than pulp fibers, in water as well as in ambient conditions. To some extent, a similar argument that was used to explain the higher hardness of viscose fibers, can also be applied here. However, it cannot explain why cellulose films exhibit also a reduced modulus which is higher than that of pulp fibers. For this, it should be considered that the cellulose films investigated are only $\approx 400\,\text{nm}$ thick and have been spin coated onto a silicon wafer. An influence of the substrate cannot be entirely excluded and is the most likely explanation. This effect of the substrate would not affect the comparison of the cellulose films with each other, since all have approximately the same thickness and the influence of the underlying silicon would be the same for all measurements.

5. Conclusions and Outlook

In the present work, three types of cellulosic materials were studied: cellulose model films, viscose fibers, and kraft pulp fibers. The purpose was to investigate the effect that water has on these materials' mechanical properties and on their surface morphologies. Such information is important when considering the bond formation in paper, which takes place initially with fully swollen, wet pulp fibers. Cellulose model films and viscose fibers acted here as model systems for pulp fibers and offered homogeneous compositions with well-defined surfaces. The detailed conclusions will be made for each material individually, for clarity's sake.

5.1. Cellulose model films

The surface morphology of cellulose model films was investigated under ambient conditions before and after a bond was formed between two films. Before bond formation, the surfaces could be regarded as self-affine and random rough at high length scales ($30\,\mu\text{m} \times 30\,\mu\text{m}$ and above). At smaller length scales ($10\,\mu\text{m} \times 10\,\mu\text{m}$ and below) it became apparent that the surface topography is in fact a superposition of two uncorrelated random rough surfaces. To describe such surfaces, the standard theory was extended to quantify the observed morphology using two parameter sets of σ, ξ, and α.

After the formation and the subsequent rupture of the bond between the two characterized films, the surface became much smoother. An RMS roughness σ three times lower compared to that of the unbonded film was determined. Moreover, the surfaces were found to be homogeneous, indicating a high area in molecular contact when a bond had still been present. Interestingly, the surface morphology of the ruptured films was best described by two superimposed self-affine random rough surfaces even at a scan size of $60\,\mu\text{m} \times 60\,\mu\text{m}$.

The mechanical properties of cellulose model films were investigated at relative humidities $\varphi_r \approx 0.5$ and in the fully swollen state. Between these two conditions, a decrease in hardness H by a factor of about 30 and a decrease in reduced modulus E_r by a factor of about 115 was found. For cellulose films with an additional layer of xylan added, a further decrease of H and E_r in water by approximately 50 % and 20 %, respectively, could be determined. Replacing distilled water as the swelling liquid with an aqueous $0.1\,\frac{\text{mol}}{\ell}$ CaCl_2 solution decreases the swelling of pure cellulose films but enhances the swelling of cellulose/xylan films. The highest decrease of H and E_r was discovered for cellulose/xylan films with DMSO – a solvent for xylan – still incorporated into the film.

It can be concluded that due to their initially smooth surfaces, pure cellulose films become soft and compliant enough to form full – or almost full – area in molecular contact. The roughness is a crucial parameter, since smooth and flat surfaces do not need a large deformation to conform to each other during bond formation and subsequent drying. This is a knowledge that can also be applied to pulp fiber-fiber bonds: The smoother and softer the pulp fiber surfaces are, the higher is the area in molecular contact and the higher the strength of the bond will be.

A further use of cellulose model films is demonstrated in an ongoing study of the adsorption behavior of xylan particles on cellulose surfaces, where cellulose films are used as substrates [114,115]. By employing AFM force mapping [116] with functionalized tips [117,118], it is possible to obtain chemical information on the nanometer scale. A differentiation between xylan and cellulose is achieved by using tips functionalized with OH- and CH_3-groups. The OH-groups lead to hydrophilic tips, whereas the CH_3-groups, on the other hand, provide hydrophobic tips and are less affected by water adsorbed on the surface. Both functionalizations result in an adhesion force to xylan which is lower than that to cellulose. In figure 5.1, a topography and phase image as well as an adhesion force map recorded with an OH-functionalized tip are presented. A lower phase shift as well as a lower adhesion force are found on elongated and round features, which correspond to xylan precipitates [115].

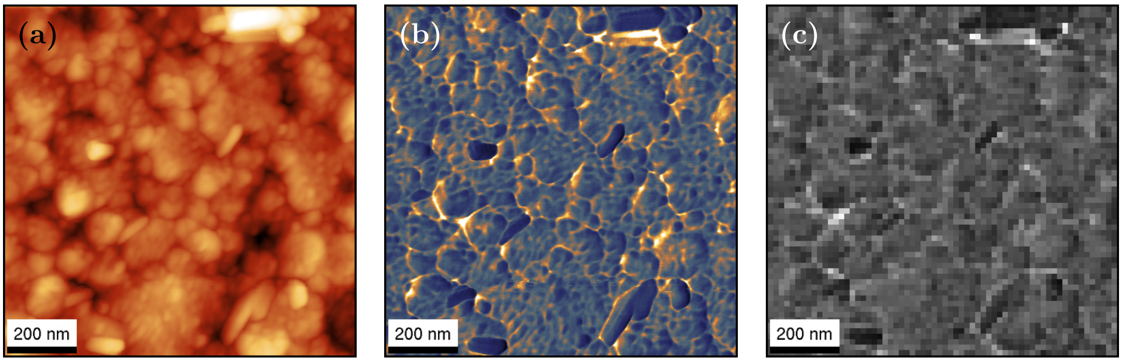

Figure 5.1.: $1\,\mu m \times 1\,\mu m$ AFM images of cellulose films with xylan precipitates. (a) Topography recorded in intermittent contact mode, z-scale: 30 nm, (b) phase image, recorded at the same time as (a), phase scale: 20° and (c) adhesion force map (64×64 pixel) obtained with OH-functionalized tips, force scale: 30 nN. (From [115].)

It is furthermore possible to extract the reduced modulus E_r from such force maps, which would allow the characterization of elastic properties on the nanometer scale [119]. In this case, unmodified silicon tips would be the preferred choice. The functionalization would introduce ambiguity in quantifying E_r, since it is a layer with unknown mechanical properties coating the tip. Also, the functionalization will increase the effective tip radius and thus reduce the resolution. The ultimate goal, of course, is the application of AFM force mapping to pulp fibers. A preliminary result of a force map recorded on a pulp fiber surface is presented in figure 5.2. Topography, adhesion force, and reduced modulus were all acquired using an AC240TS silicon probe without functionalization. It is obvious that both, adhesion force and reduced modulus, are strongly distorted by the topography. Also when employing functionalized tips to study the chemical composition of pulp fiber surfaces, a negative influence of the topography is to be expected. The smooth and homogeneous cellulose model films are, therefore, an ideal system to assess the topographical influence on the adhesion force and on E_r.

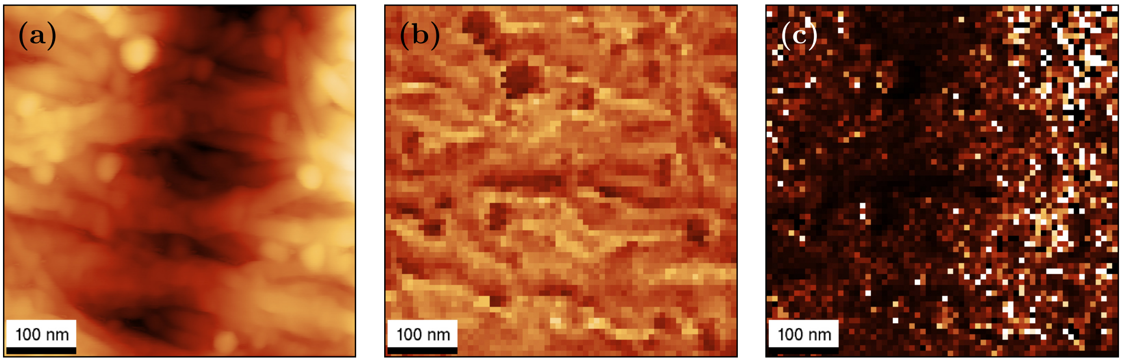

Figure 5.2.: 500 nm × 500 nm AFM images of pulp fiber surfaces. (a) Topography recorded in intermittent contact mode, z-scale: 50 nm, (b) adhesion force map (64 × 64 pixel), force scale: 15 nN, and (c) reduced modulus map (64 × 64 pixel), modulus scale: 15 GPa. The fiber axis is approximately vertically aligned.

5.2. Viscose fibers

Two types of viscose fibers were investigated: classical viscose with a highly curved surface and flat, rectangular fibers. The flat viscose fibers exhibited a surface roughness comparable to unbonded cellulose films. Classical viscose fibers were not characterized regarding their surface roughness, but a preceding study [25] revealed an RMS roughness that is five to ten times higher than the one of flat, rectangular fibers. This is one reason why unmodified classical viscose fibers cannot form bonds between them while flat rectangular fibers can [23,50,120].

Employing AFM-NI, the possibility to tune mechanical properties of swollen viscose fibers was demonstrated using cationically and anionically modified viscose fibers of both types. It could be confirmed that an increase in geometrical swelling leads to a decrease in H and E_r. Furthermore, it was found that viscose fibers which are softer and more compliant allow the production of sheets which are stronger than those formed from harder and stiffer fibers [23,50,120]. It is reasonable that besides an effect of the mechanical properties, also Coulomb interactions contribute to the fiber-fiber bond formation. This is supported by the fact that the cationic fibers cCF1 – which are only slightly softer than the reference fibers cRF – allowed already the formation of sheets, whereas cRF did not.

For unmodified, classical viscose fibers a full characterization of the dependence of H and E_r on φ_r was performed. Both quantities decreased almost in a linear manner with increasing relative humidity φ_r. At $\varphi_r \approx 0.75$, E_r decreased stronger than before that, whereas the hardness appeared to follow a linear relation until $\varphi_r \approx 0.95$. Using water sorption data of viscose fibers, it was possible to plot H and E_r as a function of the fibers' approximate water content w. Also here, a linear decrease of both properties was found, mainly because the scattering of the data did not permit a different interpretation in both cases. Comparing the extrapolated values of H and E_r at $\varphi_r = 0$ with results from fully swollen viscose fibers in water yielded that H decreases in water by a factor of about 30 and E_r by a factor of 190. This decrease of E_r in water was the highest decrease measured for all materials investigated here.

Comparing classical viscose fibers with pulp fibers leads to the observation that in the fully swollen state, E_r of both materials is approximately the same, however, the hardness of viscose fibers is at least twice the value of that for pulp fibers. This fact together with the high surface roughness of classical viscose fibers hinders the formation of interfiber bonds between them. By modifying the fibers with additives, the formation of bonds is enhanced by softer surfaces and the possibility of Coulomb interactions when a net charge is present. Tuning the swelling – and thereby the softening – of fibers could open a novel path of bond engineering. When two fibers with different swelling behaviors are bonded, stress could be introduced systematically into a bond and enhance the bond strength by this way.

5.3. Kraft pulp fibers

Kraft pulp fibers exhibit a wrinkled surface after being dried the first time. In the never dried state, a very smooth surface is observed with microfibrils clearly visible in AFM topography images. It could be shown that the wrinkles move apart from each other and decrease in height when the surrounding relative humidity is increased. This phenomenon is due to the fiber swelling during uptake of water from the atmosphere. However, not all fibers exhibited a distinct de-wrinkling, possibly because this effect is localized.

AFM-NI investigations at varying relative humidity revealed a behavior similar to that of viscose fibers. The hardness H and the reduced modulus E_r decrease almost linearly with increasing φ_r. Only at high humidities $\varphi_r > 0.8$, a stronger decrease of E_r is observed, while H still follows a linear trend. Fully swollen in water, the pulp fibers' hardness is decreased by a factor of 50 to 100, which is the largest decrease in H found in this work. E_r in water is about 100 to 150 times lower than in the dried state, a decrease which is in magnitude slightly below that of viscose fibers.

A simulation of the drying procedure taking only the decline of the fibers' elastic properties – which were determined in the present work – into account was conducted by B. N. J. Persson [83]. It yielded that upon drying almost a full area in molecular contact in fiber-fiber bonds is possible. Due to the gradual removal of water during the formation of interfiber bonds, capillary bridges between the surfaces will form and pull the fibers in even closer contact. Furthermore, the smoother a surface is, the higher the area in molecular contact will be after drying [83]. The bottom line is that reaching a full area in molecular contact is facilitated by even softer and smoother surfaces. The roughness of kraft pulp cannot be influenced much and is already very low for never dried fibers in water. However, the mechanical properties of swollen cellulosic materials can be tuned, as was shown in this work. Incorporating additives such as CMC could yield softer and more compliant pulp fibers. A similar effect was found to take place when the ionic strength of the swelling solution is increased by using salts like $CaCl_2$. In addition to obtaining preferable mechanical properties, also the formation of Coulomb interactions is enabled by these methods. Thus, the bond strength could be enhanced by stimulating two bonding mechanisms simultaneously [23,50,120].

Due to the pulp fibers' fibrillar structure, so called mechanical interlocking of fibrils and fibril bundles has been found of having an enhancing effect to fiber-fiber bonds [17]. Further insight into this mechanism could be obtained by combining the setup for controlling relative humidity with a setup to test fiber-fiber bonds in the AFM [121]. Such mechanical interlocking is usually activated by refining kraft pulp fiber to increase the number of dangling fibrils. Comparing the bond strength of refined interfiber bonds with unrefined bonds – or viscose fiber bonds – at high relative humidities ($\varphi_r > 0.9$) should result in a decreased strength of bonds between unrefined fibers. Refined fibers, on the other hand, should retain some strength if indeed mechanical interlocking is a dominating mechanism [121]. Preliminary experiments were conducted by applying a drop of water in close vicinity of a fiber-fiber bond, in such a way that at least one fiber was in contact with the water. However, these experiments were inconclusive due to the fact that the water droplet could not be applied to a stable position. Hence, controlling the humidity to increase the water uptake of the interfiber bond in a defined way is the most promising way to conduct such experiments. A possible realization of humidity controlled bond strength tests on the basis of the available AFM based fiber-fiber bond tester [121] is presented in figure 5.3.

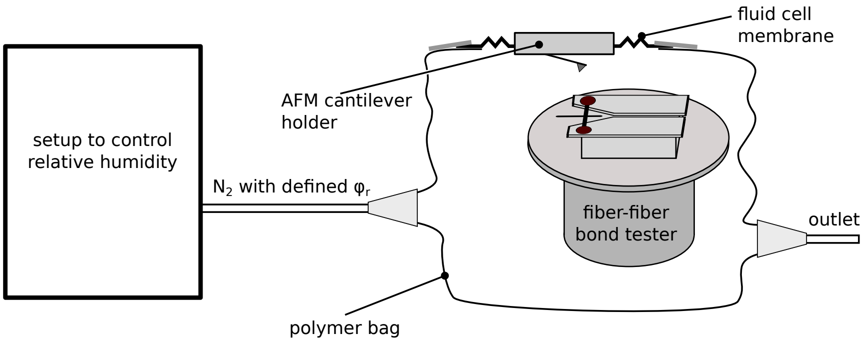

Figure 5.3.: Sketch of the planned realization of bond strength testing in controlled relative humidity.

A different way to assess the importance of water to pulp fibers and interfiber bonds is to quantify the fibers' surface energy by contact angle measurements. With this method, direct information on the tendency of water to wet the pulp fibers' surface is obtained. By employing a so-called picoliter contact angle system it is possible to deposit droplets with a volume of 80 pℓ [122]. It could be demonstrated that such droplets can be placed on single pulp fibers, using water and methylene iodide (CH_2I_2) as deposition liquids [123]. Determining the surface energies of modified fibers – i.e., different grades of refining, incorporation of additives, and swelling the fibers in aqueous solutions of salts – could yield information on how large the influence of water to the final fiber-fiber bond will be.

5.4. General conclusions

AFM based nanoindentation has been employed as a novel and strong method to reveal mechanical properties of cellulosic materials on the nanometer scale under controlled relative humidity. Using AFM-NI, the mechanical properties of cellulose based materials were studied under the influence of varying relative humidity and in water. All the materials under consideration exhibited a decrease in hardness and reduced modulus by up to two orders of magnitude only due to their uptake of water. This behavior distinguishes cellulosics from classical engineering materials such as metals, ceramics, and many synthetic polymers. However, a bond between two cellulose fibers can only be established due to this unique property. A property, which has been exploited by mankind since ancient times to produce paper.

Appendix A.

Program code

Area function plugin

The following Python script in listing A.1 is to be used with Gwyddion and extracts the area function of an AFM tip, which has been imaged according to the dilation method described in section 3.2. In order for this script to be detected by Gwyddion, it has to be placed to the location `~/.gwyddion/pygwy/`. Note that this script was tested so far only on Linux operating systems. The 32 bit Microsoft Windows port of Gwyddion should also provide support for user-made Python scripts, but requires the manual installation of additional software.

Listing A.1: Python script for Gwyddion to calculate the area function of an indenter.

```
import gwy
import pygtk
pygtk.require(’2.0’)
import gtk, gobject

# Generate a new item ”Data Evaluation” and subitem ”Area Function”
# in the menu, which is used to call the script.
plugin_menu = ”/Data Evaluation/Area Function”
plugin_type = ”PROCESS”

class InterfaceWindow:
  progress_value = 0.0

  def delete_event(self, widget, event, data=None):
    return False

  def destroy(self, widget, data=None):
    gtk.main_quit()

  # Update function to allow progress bars to move and show the progress
  def update(self):
    self.pbar.set_fraction(self.progress_value)

    percent = self.progress_value * 100
    percent = str(int(percent))
    self.pbar.set_text(percent + ”%”)
    return True
```

```
  def get_spin_button(self):
    return self.spin_button.get_value_as_int()

  def run(self):
    gobject.timeout_add(100, self.update)

  # Here, the GUI, such as buttons and text/number entry fields are
  # defined and initialized.
  def __init__(self):
    self.window = gtk.Window(gtk.WINDOW_TOPLEVEL)
    self.window.set_resizable(True)
    self.window.set_title("Area Function")

    self.window.connect("delete_event", self.delete_event)

    self.window.connect("destroy", self.destroy)

    self.window.set_border_width(10)

    vbox = gtk.VBox(False, 5)
    vbox.set_border_width(10)
    self.window.add(vbox)
    vbox.show()

    align = gtk.Alignment(0.5, 0.5, 0, 0)
    vbox.pack_start(align, False, False, 5)
    align.show()

    self.pbar = gtk.ProgressBar()
    align.add(self.pbar)
    self.pbar.show()

    separator = gtk.HSeparator()
    vbox.pack_start(separator, False, False, 0)
    separator.show()

    table = gtk.Table(1, 2, False)
    vbox.pack_start(table, False, True, 0)
    table.show()

    label = gtk.Label("Range (%): ")
    table.attach(label, 0, 1, 0, 1)
    label.show()

    adjustment = gtk.Adjustment(50, lower=0, upper=100, step_incr=1,
   page_incr=5, page_size=0)
    self.spin_button = gtk.SpinButton(adjustment, 0.0, 0)
    table.attach(self.spin_button, 1, 2, 0, 1)
    self.spin_button.show()

    separator = gtk.HSeparator()
```

```
    vbox.pack_start(separator, False, False, 0)
    separator.show()

    table = gtk.Table(2, 1, False)
    vbox.pack_start(table, False, True, 0)
    table.show()

    button = gtk.Button("Start Calculation")
    button.connect("clicked", self.Calculation)
    table.attach(button, 0, 1, 0, 1)
    button.show()

    button = gtk.Button("Close")
    button.connect_object("clicked", gtk.Widget.destroy, self.window)
    table.attach(button, 0, 1, 1, 2)
    button.show()

    self.run()
    self.window.show()

  # This is the actual calculation of the area function, the heart of the
  # script.
  def Calculation(self, widget, data=None):
    c = gwy.gwy_app_data_browser_get_current(gwy.APP_CONTAINER)

    # Get the filename...
    filename = c.get_string_by_name("/filename")
    # ... and remove ".gwy" (the last four characters).
    filebase = filename[0:-4]

    # Store (a pointer to) the currently active channel
    # (topography, hopefully) in the variable 'd'
    d = gwy.gwy_app_data_browser_get_current(gwy.APP_DATA_FIELD)
    # Get the maximum height value. Minimum should be 0!
    z_max = d.get_max()

    # Get resolution and physical dimensions of the topography map.
    xres = d.get_xres()
    yres = d.get_yres()
    xreal = d.get_xreal()
    yreal = d.get_yreal()

    # Make a DataField with the same properties as 'd', the currently
    # active channel.
    grains = gwy.DataField(xres,yres,xreal,yreal,True)

    # Initialize 'area' to 0.
    area = 0
    # Multiply the input for how many percent of the MaxHeight the
    # areafunction should be calculated
    # by 10, so the resolution is then 0.1%. (The FOR-Loop can only
    # increase the variable by integers.)
```

```
    max_pzt10 = 10*self.get_spin_button()

    # Generate and open a textfile, with the name 'filebase'_arfun.txt.
    f = open(filebase+"_arfun.txt", "w")

    # FOR-Loop where the actual calculation of the areafunction is
    # performed
    for hgt_pzt10 in range(0, max_pzt10):
      # Percentage to write in the progress bar.
      self.progress_value = float(hgt_pzt10)/float(max_pzt10-1)
      self.run()
      # Allow updating of the progress bar.
      while gtk.events_pending():
        gtk.main_iteration_do()
      # 100% means tip apex, but we want the top to be 0%.
      hgt_pzt = 100 - float(hgt_pzt10)/10.0
      # Mark the projected area of the indenter by the given threshold
      # 'hgt_pzt' and store the marked area
      # in the 'grains' datafield. As a binary height map (only 0 and 1).
      d.grains_mark_height(grains, hgt_pzt, False)
      # Get the binary height map of the grains datafield.
      A = grains.get_data()
      # Initialize the number of pixels to 0
      pixel = 0
      # Loop through the height map 'A' and if a pixel is not 0
      # (meaning, it is 1) then increase the number of pixels.
      for i in range(0,xres-1):
        for j in range(0,(yres-1)):
          if A[i*512+j] > 0:
            pixel += 1
      # The area of one pixel is determined by the resolution and the
      # physical dimensions.
      pixel_area = xreal/xres * yreal/yres
      # Multiply the pixel area by the number of pixels.
      area = pixel * pixel_area * 1e18
      # Calculate the distance from the tip apex to the current
      # position ...
      hgt = z_max*(1-hgt_pzt/100.0)*1e9
      # ... and write it to the opened file.
      f.write(str(hgt) + " " + str(area) +"\n")

    # Close the file to ensure no further modification and free it for
    # further use.
    f.close()

  def main(self):
    gtk.main()

def run():

  interface = InterfaceWindow()
  interface.main()
```

Automated AFM-NI procedure

The Octave script printed in listing A.2 is designed to extract H and E_r from AFM-NI experiments. It is especially written to work with force-vs-distance plots stored in the binary `.ibw`-files outputted by the Asylum Research software. Note that this script requires the input of 16 parameters by the user. Therefore, a graphical interface was written to ease the usage of this program. The graphical interface was coded in C and is not listed in this work.

Listing A.2: Octave script that allows the automatic evaluation of AFM-NI experiments.

```
function savename = INDmain(loadname, diols, k, loadrate, holdtime,
    thermaltime, thermprcnt, samplerate, epsilon, basefit, holdred,
    thermred, holdpnt, thermpnt, areafunc_file, uld_fit_nr)

  %Import IgorPro .ibw files as ASCII text, then scale the values
  %accordingly
  xy0 = IBWtoTXT(loadname);
  xy0(:,2) = xy0(:,2)*1e9;

  %Subtract the thermal drift from the data (separate function, not
  %shown)
  INDpreproc(loadname, samplerate, thermaltime);
  lfm = length(loadname)-4;
  corrname = [loadname(1:lfm), ”z_corr.txt”];
  xy0(:,1) = load(corrname);

  xy = xy0;
  l = length(xy(:,2));

  %Get the maximal value (v) and its index (i)
  [v,i]=max(xy(1:holdpnt,2))

  %Find the zero force line by a line fit and subtract it from the data
  zero_line = INDlin_leasqr(xy(100:100+basefit,1),xy(100:100+basefit,2));
  xy(:,2)=xy(:,2)-(zero_line(2)*xy(:,1)+zero_line(1)*ones(l,1));

  %Calculate the RMS of noise level, set it to 0.1 if it is lower than
  %that
  noise = std(xy(100:100+basefit,2))
  if (noise < 0.10)
    noise = 0.10
  endif

  %Locate point of contact, using the noise level as a reference
  j = i;
  while xy(j,2) > 4*noise;
    j = j - 1;
    x_zero = xy(j,1);
    x_zero_index = j;
  endwhile
```

```
%Subtract deflection from distance to get indentation
xy(:,1) = xy(:,1)-xy(:,2);
%Calculate force from deflection
xy(:,2) = xy(:,2)*k;
%Shift all values so that the point of contact is at zero force
xy(:,1)=xy(:,1)-x_zero*ones(l,1);
%split the experiment in a loading curve and an unloading curve
 xy_load(:,1)=xy(1:i,1);
 xy_load(:,2)=xy(1:i,2);
 xy_unld1(:,1)=xy(i+1:l,1);
 xy_unld1(:,2)=xy(i+1:l,2);
m = int32(samplerate*holdtime);
 lul1 = length(xy_unld1(:,1));
 xy_unld(:,1)=xy_unld1(m-1:lul1,1);
 xy_unld(:,2)=xy_unld1(m-1:lul1,2);
 xy_load2(:,1)=xy_unld1(1:m-1,1);
 xy_load2(:,2)=xy_unld1(1:m-1,2);

 ll2 = length(xy_load2(:,1));

 factor2 = holdred;
 p = 1;
 for j=1:m-1
   if (mod(j,factor2) == 0)

     xy_load3(p,1) = xy_load2(j,1);
     xy_load3(p,2) = xy_load2(j,2);
     p = p+1;
   endif
 endfor

%Decrease number of datapoints in thermal drift compensation hold
%(faster pdf-plot!)
Fmax = max(xy_unld(:,2));
 uld1_time = (thermprcnt*Fmax)/(loadrate*1000)
 uld1_index = thermpnt;
 xy_unld5 = xy_unld(1:uld1_index,:);
 xy_unld6 = xy_unld(uld1_index+1:uld1_index+1+int32(thermaltime*
   samplerate),:);
 xy_unld7 = xy_unld(uld1_index+1+int32(thermaltime*samplerate)+1:length(
   xy_unld(:,1)),:);
 factor3 = thermred;
 p = 1;
 for j=1:int32(thermaltime*samplerate)

   if (mod(j,factor3) == 0)

     xy_unld6b(p,1) = xy_unld6(j,1);
     xy_unld6b(p,2) = xy_unld6(j,2);
     p = p+1;

   endif
```

```
endfor

t_therm = thermaltime*(0:length(xy_unld6(:,1))-1)'/(length(xy_unld6
  (:,1))-1);
time_load = ((x_zero_index:length(xy_load(:,1)))' - x_zero_index)/(
  length(xy_load(:,1)) - x_zero_index);
time_hold = time_load(length(time_load)) + (holdtime*(1:length(xy_load3
  (:,1)))')/(length(xy_load3(:,1)));
time_unld5 = time_hold(length(time_hold)) + (uld1_time*(1:length(
  xy_unld5(:,1)))')/(length(xy_unld5(:,1)));

%Fit the beginning of the unloading curve to obtain the
%unloading stiffness
unld5_length = length(xy_unld5(:,1));
[uld_fit, uld_p, uld_cvg, uld_iter] = leasqr(xy_unld5(1:uld_fit_nr,2),
  xy_unld5(1:uld_fit_nr,1),[50, 1, 1, 1, 1],@INDpower_law, 0.001, 1000);
Fmax = max(xy(:,2));
stiffness_fit = inv((1/2)*uld_p(2)*Fmax^(-1/2) + (1/4)*uld_p(3)*Fmax
  ^(-3/4) + (1/8)*uld_p(4)*Fmax^(-7/8));

%Creep and thermal drift correction of the unloading stiffness
t_crp = holdtime*(0:length(xy_load3(:,1))-1)'./(length(xy_load3(:,1))
  -1);
[crp_fit, crp_p] = leasqr(t_crp, xy_load3(:,1),[40, 1.5, 1.0, 1.0],
  @INDcreep_time, 0.001, 1000);
h_dot_tot = (1/2)*crp_p(2)*holdtime^(-1/2) + (1/4)*crp_p(3)*holdtime
  ^(-3/4) + (1/8)*crp_p(4)*holdtime^(-7/8)
stiffness = inv(1/stiffness_fit + h_dot_tot/(loadrate*1000));

x_max = max([xy_load3(:,1); xy_unld(:,1)]);
x0 = x_max - epsilon*Fmax/stiffness;
area_xy = load(areafunc_file);

if (x0 >= 100)
   [area_fit, p_area] = leasqr(area_xy(:,1),area_xy(:,2),[500, 10, 10],
  @INDareafunc_fit,1e-5,1000);
elseif (x0 <100)
   area_fit_end = 0;
   i = 1;
   while (area_xy(i,1) < 100)
      area_fit_end = i;
      i++;
   endwhile
   %Fit the experimentally obtained area function
   [area_fit, p_area] = leasqr(area_xy(1:area_fit_end,1),area_xy(1:
  area_fit_end,2),[500, 10, 10],@INDareafunc_fit,1e-5,1000);
endif

%Calculate the contact area at indentation depth from the fitted
%area function
A = INDareafunc_fit(x0,p_area);
```

```
   plot(area_xy(:,1), area_xy(:,2),(0:550)',INDareafunc_fit((0:550)',
     p_area));
   print('-dpng', 'test4.png');

   %Calculate reduced modulus and hardness
   Er = sqrt(pi)/2*(stiffness/sqrt(A));
   H = Fmax/A;

   %Calculate a line with the unloading slope for visualization
   stiffn_d = Fmax - stiffness*xy_unld(1);
   stiffn_y = xy_unld(1:int32(samplerate*uld1_time),1)*stiffness +
     stiffn_d;
   xy_fit = [xy_unld(1:int32(samplerate*uld1_time),1),stiffn_y];

   names = ["x0/[nm]\t\t\t", "Fmax/[nN]\t", "A/[nm^2]\t\t", "Er/[GPa]\t\t"
     , "H/[GPa]"];
   save_x0 = [x0, Fmax, A, Er, H];

   save_rslt = save_x0;
   save_rslt(2) = save_rslt(2)/1000;
   sl = strchr(loadname,'.') - 1;
   savename = loadname(1,1:sl);
   savename_load = [savename,"_load.dat"];
   savename_hold = [savename,"_hold.dat"];
   savename_unld = [savename,"_unld.dat"];
   savename_fit = [savename," _fit.dat"];
   savename_x0 = [savename, "_x0.dat"];
   savename_rslt = [savename, "_results.dat"];

   xy_load(:,2) = 1e-3*xy_load(:,2);
   xy_unld(:,2) = 1e-3*xy_unld(:,2);
   xy_load3(:,2) = 1e-3*xy_load3(:,2);
   xy_fit(:,2) = 1e-3*xy_fit(:,2);

   %Save the results and the information necessary to plot the data
   save(savename_load, 'xy_load','-ascii');
   save(savename_hold, 'xy_load3','-ascii');
   save(savename_unld, 'xy_unld','-ascii');
   save(savename_fit, 'xy_fit', '-ascii');
   save(savename_x0, 'names','save_x0');
   save(savename_rslt, 'save_rslt', '-ascii');

end
```

List of publications

1. Jansen, H.P., Sotthewes, K., **Ganser, C.**, Teichert, C., Zandvliet, H.J.W., and Kooij, E.S. (2012) Tuning kinetics to control droplet shapes on chemically striped patterned surfaces. *Langmuir*, **28**, 13137-13142.

2. Vasić, B., Kratzer, M., Matković, A., Nevosad, A., Ralević, U., Jovanović, D., **Ganser, C.**, Teichert, C. , and Gajić, R. (2013) Atomic force microscopy based manipulation of graphene using dynamic plowing lithography. *Nanotechnology*, **24**, 015303.

3. Persson, B.N.J. , **Ganser, C.**, Schmied, F., Teichert, C., Schennach, R., Gilli, E., and Hirn, U. (2013) Adhesion of cellulose fibers in paper. *J. Phys.: Condens. Matter.*, **25**, 045002.

4. Rebelo de Figueiredo, M., Bergmann, C., **Ganser, C.**, Teichert, C., Kukla, C., and Mitterer, C. (2013) Adhesion tendency of polymers to hard coatings. *Int. Polym. Proc.*, **28**, 415-420.

5. Hirn, U., Schennach, R., **Ganser, C.**, Magnusson, M., Teichert, C., and Östlund, S. (2013) The area in molecular contact in fiber-fiber bonds. in: *Advances in Pulp and Paper Research (ed. S. J. I'Anson): Proceedings of the Fundamental Research Symposium Cambridge 2013*, 201-226.

6. **Ganser, C.**, Hirn, U., Rohm, S., Schennach, R., and Teichert, C. (2014) AFM nanoindentation of pulp fibers and thin cellulose films at varying relative humidity. *Holzforschung*, **68**, 53-60.

7. Rohm, S., Hirn, U., **Ganser, C.**, Teichert, C., and Schennach, R. (2014) Thin cellulose films as a model system for paper fibre bonds. *Cellulose*, **21**, 237-249.

8. Fischer, W.J., Zankel, A., **Ganser, C.**, Schmied, F.J., Schroettner, H., Hirn, U., Teichert, C., Bauer, W., and Schennach, R. (2014) Imaging of the formerly bonded area of individual fibre to fibre joints with SEM and AFM. *Cellulose*, **21**, 251-260.

9. Lackner, J.M., Waldhauser, W., **Ganser, C.**, Teichert, C., Kot, M., and Major, L. (2014) Mechanisms of topography formation of magnetron-sputtered chromium-based coatings on epoxy polymer composites. *Surf. Coat. Tech.*, **241**, 80-85.

10. Saketi, P., Hirvonen, J., Lai, Y., **Ganser, C.**, Teichert, C., Järnström, J., Fardim, P., and Kallio, P (2014) Automated Drop-on-Fiber contact angle measurement using a microrobotic platform using a microrobotic platform. *Nord. Pulp Pap. Res. J.*, **29**, 225-231.

11. **Ganser, C.**, Weber, F., Czibula, C., Bernt, I., Schennach, R., and Teichert, C. (2014) Tuning hardness of swollen viscose fibers. *Bioinspired, Biomimetic and Nanobiomaterials*, DOI: **10.1680/bbn.14.00008**, 1–7.

12. Miletzky, A., Punz, M., Zankel, A., Schlader, S., Czibula, C., **Ganser, C.**, Teichert, C., Spirk, S., Zöhrer, S., Bauer, W., and Schennach, R. (2014) Modifying cellulose fibers by adsorption/precipitation of xylan. *submitted to Cellulose.*

13. Weber, F., **Ganser, C.**, Teichert, C., Schennach, R., Bernt, I., and Eckhart, R. (2014) Application of the Page-equation on viscose fibre - hand sheets. *submitted to Cellulose.*

14. Jansen, H. P., Sotthewes, K., **Ganser, C.**, Zandvliet, H. J. W., Teichert, C., and Kooij, E. S. (2014) The shape of picoliter droplets on chemically striped patterned substrates. *submitted to Langmuir.*

15. **Ganser, C.**, Gasparic, P., Zöhrer, S., Niegelhell, K., Czibula, C., Miletzky, A., Teichert, C., Stana-Kleinschek, K., Schennach, R., and Spirk, S. (2014) Interactions of birch xylan with cellulose thin films - a QCM-D and AFM study. *In preparation for submission to Cellulose.*

Acknowledgments

No work is ever done in solitude. During the three years, when I collected all the materials for this work and finally put it together, I crossed paths with many people. This is the place where I want to honor their contributions – sometimes obvious ones, sometimes not so obvious, but nonetheless always helpful and gratefully appreciated.

I want to thank

Ao. Univ.-Prof. Dr. Christian Teichert for the excellent supervision and encouragement, for teaching me about science and giving me the freedom to walk my own path, **Ao. Univ.-Prof. Dr. Robert Schennach** for heading the CD-Lab and giving me the possibility to perform my work within this great environment, for encouragement, fruitful discussions, and always having an open ear, **Univ.-Prof. Dr. Oskar Paris** for giving me the opportunity to perform my research at the Institute of Physics, **Esther Schennach, MSc.** for all the hard work behind the curtains of the CD-Lab, and great support with all the administrative tasks, **Patrice Kreiml** for taking a great load off my shoulders by diving into the depths of microbalance sorption measurements in my stead and most importantly for being a good friend, **Caterina Czibula** for reducing my amount of work by relentlessly pursuing the mysteries of AFM force mapping with functionalized tips and for proof-reading this work, **Dr. Markus Kratzer** for having an open ear for all problems, for fruitful discussions about analysis procedures, methods and experiments, and interesting conversations within and beyond science, **Dr. Wolfgang J. Fischer** for discussions and providing fiber-fiber bond samples, a great cooperation, and for a nice time in the CD-Lab, **Dr. Frederik Weber** for sharing the viscose fiber samples and swelling measurements of viscose fibers, for discussions, a great cooperation, and for a nice time in the CD-Lab, **Dipl.-Ing. Albrecht Miletzky** for sharing pulp fiber samples, discussions, a great cooperation, and for a nice time in the CD-Lab, **Dipl.-Ing. Sebastian Rohm** for producing and providing all kinds of cellulose films, a great cooperation, and for a nice time in the CD-Lab, **Dr. Ulrich Hirn** for fruitful discussions, encouragement, and a great cooperation, **Univ.-Prof. Dr. Wolfgang Bauer** for discussions during the meetings, encouragement, and a good time in Stockholm, **Dipl.-Ing. Stefan Diebald, Dipl.-Ing. Jussi Lahti, Siegfried Zöhrer** for discussions and a good time in the CD-Lab, **Dr. Franz J. Schmied, Dipl.-Ing. Leo Arpa** for helpful discussions regarding pulp fibers in scientific and industrial points of view, for providing industrial kraft pulp fiber samples, and a great collaboration, **Dr. Ingo Bernt, Dr. Walter Roggenstein** for helpful discussions on regenerated cellulose fibers, for producing and providing all kinds of viscose fiber samples, and a great collaboration, **Dr. Stefan Spirk** for a fruitful cooperation and encouraging words, **Dr. Herbert Wormeester, Dr. Arzu Colak** for sharing their knowledge on how to build a system that allows to control

relative humidity, **Dr. Kartik Pondicherry** for doing SEM images of one of my AFM tips, **Dr. Andreas Nevosad, Mgr. inz. Monika Mirkowska, Dipl.-Ing. Quan Shen, Dipl.-Ing. Stefan Lorbek, Stefan Klima, Lukáš Kormoš** for interesting discussions within and outside the SPM group, while having a great time, **Marianne Kräuter** and **Armin Zepic** for help with measurements during their internships, **Ao. Univ.-Prof. Dr. Josef Oswald, Ao. Univ.-Prof. Dr. Ronald Meisels, Dr. Markus A. Hartmann, Dr. Rainer T. Lechner, Dr. Parvin Sharifi, Mag. Soran Nabavi, Dipl.-Ing. Roland Morak, Dipl.-Ing. Christian Prehal, Dipl.-Ing. Max Burian** for providing a nice working climate at the Institute of Physics, **Ing. Heinz Pirker, Heide Kirchberger, Magdalena Ottrin, and Peter Moharitsch** for appreciated help with technical and administrative tasks, **The Federal Ministry of Economy, Family and Youth and the National Foundation for Research, Technology and Development** for funding of this this work,

and last but not least

my friends and family simply for being there.

Thank you.

Bibliography

[1] Klemm, D., Heublein, B., Fink, H., and Bohn, A. (2005) Cellulose: Fascinating Biopolymer and Sustainable Raw Material. *Angew. Chem. Int. Ed.*, **44**, 3358–3393.

[2] Bergfjord, C., Mannering, U., Frei, K. M., Gleba, M., Scharff, A., Skals, I., Heinemeier, J., Nosch, M.-L., and Holst, B. (2012) Nettle as a distinct Bronze Age textile plant. *Sci. Rep.*, **2**, 664.

[3] Hubbe, M. and Bowden, C. (2009) Handmade paper: a review of its history, craft, and science. *BioResources*, **4**, 1736–1792.

[4] Lindström, T., Wågberg, L., and Larsson, T. (2005) On the nature of joint strength in paper—a review of dry and wet strength resins used in paper manufacturing. *13th Fundamental research symposium*, vol. 1, pp. 457–562, The Pulp and Paper Fundamental Research Society Cambridge, UK.

[5] van de Ven, T. G. (2008) Capillary forces in wet paper. *Ind. Eng. Chem. Res.*, **47**, 7250–7256.

[6] Tejado, A. and van de Ven, T. G. (2010) Why does paper get stronger as it dries? *Mater. Today*, **13**, 42–49.

[7] Haslach Jr, H. W. (1996) A model for drying-induced microcompressions in paper: buckling in the interfiber bonds. *Composites Part B*, **27**, 25–33.

[8] Vainio, A. and Paulapuro, H. (2007) Interfiber bonding and fiber segment activation in paper. *BioResources*, **2**, 442–458.

[9] Fernandes Diniz, J., Gil, M., and Castro, J. (2004) Hornification—its origin and interpretation in wood pulps. *Wood Sci. Technol.*, **37**, 489–494.

[10] Rowell, R., Pettersen, R., Han, J., Rowell, J., and Tshabalala, M. (2005) Cell wall chemistry. *Handbook of wood chemistry and wood composites*, pp. 33–77, CRC Press, Boca Raton.

[11] Krässig, H., Schurz, J., Steadman, R. G., Schliefer, K., and Albrecht, W. (2007) *Cellulose*, pp. 1–55. Wiley-VCH Verlag GmbH & Co. KGaA.

[12] Donaldson, L. (2007) Cellulose microfibril aggregates and their size variation with cell wall type. *Wood Sci. Technol.*, **41**, 443–460.

[13] Booker, R. and Sell, J. (1998) The nanostructure of the cell wall of softwoods and its functions in a living tree. *Holz Roh- Werkst.*, **56**, 1–8.

[14] Terashima, N., Kitano, K., Kojima, M., Yoshida, M., Yamamoto, H., and Westermark, U. (2009) Nanostructural assembly of cellulose, hemicellulose, and lignin in the middle layer of secondary wall of ginkgo tracheid. *J. Wood Sci.*, **55**, 409–416.

[15] Mauseth, J. D. (2014) *Botany: An Introduction to Plant Biology*. Jones & Bartlett Learning, Burlington, 5^{th} edn.

[16] Higuchi, T. (1997) *Biochemistry and molecular biology of wood*. Springer, Berlin.

[17] Schmied, F. J., Teichert, C., Kappel, L., Hirn, U., Bauer, W., and Schennach, R. (2013) What holds paper together: Nanometre scale exploration of bonding between paper fibres. *Sci. Rep.*, **3**, 2432.

[18] Lenz, J., Schurz, J., and Wrentschur, E. (1988) The fibrillar structure of cellulosic man-made fibers spun from different solvent systems. *J. Appl. Polym. Sci.*, **35**, 1987–2000.

[19] Smole, M. S., Peršin, Z., Kreže, T., Kleinschek, K. S., Ribitsch, V., and Neumayer, S. (2003) X-ray study of pre-treated regenerated cellulose fibres. *Mater. Res. Innovations*, **7**, 275–282.

[20] Jiang, G., Huang, W., Li, L., Wang, X., Pang, F., Zhang, Y., and Wang, H. (2012) Structure and properties of regenerated cellulose fibers from different technology processes. *Carbohydr. Polym.*, **87**, 2012–2018.

[21] Saito, T., Hirota, M., Tamura, N., and Isogai, A. (2010) Oxidation of bleached wood pulp by TEMPO/NaClO/$NaClO_2$ system: effect of the oxidation conditions on carboxylate content and degree of polymerization. *J. Wood Sci.*, **56**, 227–232.

[22] Yu, Y., Kettunen, H., and Niskanen, K. (1999) Can viscose fibres reinforce paper? *J. Pulp Pap. Sci.*, **25**, 398–402.

[23] Weber, F., Koller, G., Schennach, R., Bernt, I., and Eckhart, R. (2013) The surface charge of regenerated cellulose fibres. *Cellulose*, **20**, 2719–2729.

[24] Binnig, G., Quate, C., and Gerber, C. (1986) Atomic force microscope. *Phys. Rev. Lett.*, **56**, 930–933.

[25] Ganser, C. (2011) *Surface characterization of cellulose fibers by atomic force microscopy in liquid media and under ambient conditions*. Master's thesis, Montanuniversität Leoben.

[26] Morita, S., Wiesendanger, R., and Meyer, E. (2002) *Noncontact atomic force microscopy*, vol. 1. Springer, Berlin.

[27] Zhong, Q., Inniss, D., Kjoller, K., and Elings, V. (1993) Fractured polymer/silica fiber surface studied by tapping mode atomic force microscopy. *Surf. Sci. Lett.*, **290**, L688–L692.

[28] Putman, C., Van der Werf, K., De Grooth, B., Van Hulst, N., and Greve, J. (1994) Tapping mode atomic force microscopy in liquid. *Appl. Phys. Lett.*, **64**, 2454–2456.

[29] Hörber, J. and Miles, M. (2003) Scanning probe evolution in biology. *Science*, **302**, 1002–1005.

[30] Moreno-Herrero, F., de Jager, M., Dekker, N. H., Kanaar, R., Wyman, C., and Dekker, C. (2005) Mesoscale conformational changes in the DNA-repair complex Rad50/Mre11/Nbs1 upon binding DNA. *Nature*, **437**, 440–443.

[31] Harris, D., Bulone, V., Ding, S., and DeBolt, S. (2010) Tools for cellulose analysis in plant cell walls. *Plant Physiol.*, **153**, 420–426.

[32] Schmitz, I., Schreiner, M., Friedbacher, G., and Grasserbauer, M. (1997) Phase imaging as an extension to tapping mode AFM for the identification of material properties on humidity-sensitive surfaces. *Appl. Surf. Sci.*, **115**, 190–198.

[33] Raghavan, D., Gu, X., Nguyen, T., VanLandingham, M., and Karim, A. (2000) Mapping polymer heterogeneity using atomic force microscopy phase imaging and nanoscale indentation. *Macromolecules*, **33**, 2573–2583.

[34] Teichert, C., Haas, A., Wallner, G. M., and Lang, R. W. (2002) Nanometer scale characterization of polymer films by atomic-force microscopy. *Macromolecular Symposia*, vol. 181, pp. 457–466, Wiley Online Library.

[35] Schmied, F. J., Teichert, C., Kappel, L., Hirn, U., and Schennach, R. (2012) Analysis of precipitated lignin on kraft pulp fibers using atomic force microscopy. *Cellulose*, **19**, 1013–1021.

[36] Oliver, W. and Pharr, G. (1992) Improved technique for determining hardness and elastic modulus using load and displacement sensing indentation experiments. *J. Mater. Res.*, **7**, 1564–1583.

[37] Yan, D. and Li, K. (2013) Conformability of wood fiber surface determined by AFM indentation. *J. Mater. Sci.*, **48**, 322–331.

[38] Ganser, C., Hirn, U., Rohm, S., Schennach, R., and Teichert, C. (2014) AFM nanoindentation of pulp fibers and thin cellulose films at varying relative humidity. *Holzforschung*, **68**, 53–60.

[39] Feng, G. and Ngan, A. H. W. (2002) Effects of creep and thermal drift on modulus measurement using depth-sensing indentation. *J. Mater. Res.*, **17**, 660–668.

[40] Tang, B. and Ngan, A. H. W. (2003) Accurate measurement of tip–sample contact size during nanoindentation of viscoelastic materials. *J. Mater. Res.*, **18**, 1141–1148.

[41] Gindl, W., Gupta, H., Schöberl, T., Lichtenegger, H., and Fratzl, P. (2004) Mechanical properties of spruce wood cell walls by nanoindentation. *Appl. Phys. A: Mater.*, **79**, 2069–2073.

[42] Clifford, C. A. and Seah, M. P. (2005) Quantification issues in the identification of nanoscale regions of homopolymers using modulus measurement via AFM nanoindentation. *Appl. Surf. Sci.*, **252**, 1915 – 1933.

[43] Tranchida, D., Piccarolo, S., and Soliman, M. (2006) Nanoscale Mechanical Characterization of Polymers by AFM Nanoindentations: Critical Approach to the Elastic Characterization. *Macromolecules*, **39**, 4547–4556.

[44] Jee, A.-Y. and Lee, M. (2010) Comparative analysis on the nanoindentation of polymers using atomic force microscopy. *Polym. Test.*, **29**, 95 – 99.

[45] Fuhrmann, A., Staunton, J., Nandakumar, V., Banyai, N., Davies, P., and Ros, R. (2011) AFM stiffness nanotomography of normal, metaplastic and dysplastic human esophageal cells. *Phys. Biol.*, **8**, 015007.

[46] Roos, W. and Wuite, G. (2009) Nanoindentation studies reveal material properties of viruses. *Adv. Mater.*, **21**, 1187–1192.

[47] Nilsson, B., Wågberg, L., and Gray, D. (2000) *Conformability of wet pulp fibres at small length scales*. Mitthögskolan, FSCN.

[48] Chhabra, N., Spelt, J., Yip, C., and Kortschot, M. (2005) An investigation of pulp fibre surfaces by atomic force microscopy. *J. Pulp Pap. Sci.*, **31**, 52–56.

[49] Sasaki, T., Okamoto, T., and Meshitsuka, G. (2006) Influence of deformability of kraft pulp fiber surface estimated by force curve measurements on atomic force microscope (AFM) contact mode imaging. *J. Wood Sci.*, **52**, 377–382.

[50] Ganser, C., Weber, F., Czibula, C., Bernt, I., Schennach, R., and Teichert, C. (2014) Tuning hardness of swollen viscose fibers. *Bioinspired, Biomimetic and Nanobiomaterials*, **10.1680/bbn.14.00008**, 1–7.

[51] Sensirion AG (2014), Introduction to humidity - basic principles on physics of water vapor. Application Note.

[52] Chatfield, C. (2004) *The analysis of time series*. CRC Press, Boca Raton.

[53] Teichert, C. (2002) Self-organization of nanostructures in semiconductor heteroepitaxy. *Phys. Rep.*, **365**, 335–432.

[54] Yang, H.-N., Wang, G.-C., and Lu, T.-M. (1993) *Diffraction from rough surfaces and dynamic growth fronts*. World Scientific, Singapore.

[55] Zhao, Y., Wang, G., and Lu, T. (2001) *Characterization of amorphous and crystalline rough surface: principles and applications*. Academic Press, San Diego.

[56] Pelliccione, M. and Lu, T.-M. (2008) *Evolution of thin film morphology: modeling and simulations*, vol. 108. Springer, Berlin.

[57] Nečas, D. and Klapetek, P. (2012) Gwyddion: an open-source software for SPM data analysis. *Cent. Eur. J. Phys.*, **10**, 181–188.

[58] Butz, T. (2011) *Fouriertransformation für Fußgänger*. Vieweg+Teubner, Wiesbaden.

[59] Champeney, D. (1973) *Fourier transforms and their physical applications*. Academic Press, New York.

[60] Cooley, J. and Tukey, J. (1965) An algorithm for the machine calculation of complex Fourier series. *Math. Comput*, **19**, 297–301.

[61] Frigo, M. and Johnson, S. (2005) The design and implementation of FFTW3. *Proc. IEEE*, **93**, 216–231.

[62] Mandelbrot, B. B. (1983) *The fractal geometry of nature*. WH Freeman and Co., New York.

[63] Family, F. (1990) Dynamic scaling and phase transitions in interface growth. *Physica A: Statistical Mechanics and its Applications*, **168**, 561 – 580.

[64] Krim, J., Heyvaert, I., Van Haesendonck, C., and Bruynseraede, Y. (1993) Scanning tunneling microscopy observation of self-affine fractal roughness in ion-bombarded film surfaces. *Phys. Rev. Lett.*, **70**, 57–60.

[65] Hurst, H. E. (1951) Long-term storage capacity of reservoirs. *Trans. Amer. Soc. Civil Eng.*, **116**, 770–808.

[66] Krim, J. and Indekeu, J. (1993) Roughness exponents: A paradox resolved. *Phys. Rev. E*, **48**, 1576–1578.

[67] Sinha, S., Sirota, E., Garoff, S., and Stanley, H. (1988) X-ray and neutron scattering from rough surfaces. *Phys. Rev. B*, **38**, 2297–2311.

[68] Palasantzas, G. (1993) Roughness spectrum and surface width of self-affine fractal surfaces via the K-correlation model. *Phys. Rev. B*, **48**, 14472–14478.

[69] Al-Harthi, S., Revathy, K., Gard, F., Mesli, A., George, A., Bartringer, J., Mamor, M., and Unnikrishnan, N. (2010) Self-assembly of silver nanoparticles and multiwall carbon nanotubes on decomposed GaAs surfaces. *Nanoscale Res. Lett.*, **5**, 1737–1743.

[70] Xu, C., Tian, H., Reece, C. E., and Kelley, M. J. (2011) Enhanced characterization of niobium surface topography. *Phys. Rev. ST Accel. Beams*, **14**, 123501.

[71] Munz, M., Kim, J.-H., Krause, O., and Roy, D. (2011) Imaging surfaces of nanoscale roughness by atomic force microscopy with carbon nanotubes as tips: a comparative study. *Surf. Interface Anal.*, **43**, 1382–1391.

[72] Pandit, P., Banerjee, M., and Gupta, A. (2014) Growth and morphological analysis of ultra thin PMMA films prepared by Langmuir–Blodgett deposition technique. *Colloids Surf., A*, **454**, 189 – 195.

[73] Hutter, J. L. and Bechhoefer, J. (1993) Calibration of atomic-force microscope tips. *Rev. Sci. Instrum.*, **64**, 1868–1873.

[74] Villarrubia, J. (1994) Morphological estimation of tip geometry for scanned probe microscopy. *Surf. Sci.*, **321**, 287 – 300.

[75] Octave community (2014), GNU Octave 3.8.1. www.gnu.org/software/octave/.

[76] Gindl, W., Konnerth, J., and Schöberl, T. (2006) Nanoindentation of regenerated cellulose fibres. *Cellulose*, **13**, 1–7.

[77] Kontturi, E., Thüne, P., and Niemantsverdriet, J. (2003) Novel method for preparing cellulose model surfaces by spin coating. *Polymer*, **44**, 3621 – 3625.

[78] Djak, M., Gilli, E., Kontturi, E., and Schennach, R. (2011) Thickness dependence of reflection−absorption infrared spectra of supported thin polymer films. *Macromolecules*, **44**, 1775–1778.

[79] Rohm, S., Hirn, U., Ganser, C., Teichert, C., and Schennach, R. (2014) Thin cellulose films as a model system for paper fibre bonds. *Cellulose*, **21**, 237–249.

[80] Levenberg, K. (1944) A method for the solution of certain nonlinear problems in least squares. *Quart. Appl. Math*, **2**, 164–168.

[81] Marquardt, D. (1963) An algorithm for least-squares estimation of nonlinear parameters. *Journal of the society for Industrial and Applied Mathematics*, **11**, 431–441.

[82] Tolan, M., Seeck, O., Schlomka, J.-P., Press, W., Wang, J., Sinha, S., Li, Z., Rafailovich, M., and Sokolov, J. (1998) Evidence for capillary waves on dewetted polymer film surfaces: A combined X-ray and atomic force microscopy study. *Phys. Rev. Lett.*, **81**, 2731.

[83] Persson, B. N. J., Ganser, C., Schmied, F., Teichert, C., Schennach, R., Gilli, E., and Hirn, U. (2013) Adhesion of cellulose fibers in paper. *J. Phys.: Condens. Matter*, **25**, 045002.

[84] Rohm, S. (2013) *Thin Cellulose Films as Model Systems for Paper-Fibres*. Master's thesis, Graz University of Technology.

[85] Grignon, J. and Scallan, A. M. (1980) Effect of pH and neutral salts upon the swelling of cellulose gels. *J. Appl. Polym. Sci.*, **25**, 2829–2843.

[86] Fält, S., Wågberg, L., and Vesterlind, E.-L. (2003) Swelling of model films of cellulose having different charge densities and comparison to the swelling behavior of corresponding fibers. *Langmuir*, **19**, 7895–7903.

[87] Pelegri, A. A. and Huang, X. (2008) Nanoindentation on soft film/hard substrate and hard film/soft substrate material systems with finite element analysis. *Compos. Sci. Technol.*, **68**, 147 – 155.

[88] Welch, B. (1947) The generalization of student's problem when several different population variances are involved. *Biometrika*, **34**, 28–35.

[89] Froix, M. F. and Nelson, R. (1975) The interaction of water with cellulose from nuclear magnetic resonance relaxation times. *Macromolecules*, **8**, 726–730.

[90] Donnan, F. G. (1911) Theorie der Membrangleichgewichte und Membranpotentiale bei Vorhandensein von nicht dialysierenden Elektrolyten. Ein Beitrag zur physikalisch-chemischen Physiologie. *Zeitschrift für Elektrochemie und angewandte physikalische Chemie*, **17**, 572–581.

[91] Korsunsky, A., McGurk, M., Bull, S., and Page, T. (1998) On the hardness of coated systems. *Surf. Coat. Technol.*, **99**, 171 – 183.

[92] Kreiml, P., Ganser, C., and Teichert, C. (2014). unpublished.

[93] Mandelbrot, B. B., Passoja, D. E., and Paullay, A. J. (1984) Fractal character of fracture surfaces of metals. *Nature*, **308**, 721–722.

[94] Lapique, F., Meakin, P., Feder, J., and Jøssang, T. (2002) Self-affine fractal scaling in fracture surfaces generated in ethylene and propylene polymers and copolymers. *J. Appl. Polym. Sci.*, **86**, 973–983.

[95] Jeffries, R. (1960) The sorption of water by cellulose and eight other textile polymers. *J. Text. I. Transactions*, **51**, T339–T340.

[96] Simpson, W. and TenWolde, A. (1999) *Wood handbook: wood as an engineering material*, chap. Physical properties and moisture relations of wood, pp. 3–1 – 3–24. United States Government Printing.

[97] Okubayashi, S., Griesser, U. J., and Bechtold, T. (2005) Moisture sorption/desorption behavior of various manmade cellulosic fibers. *J. Appl. Polym. Sci.*, **97**, 1621–1625.

[98] Parker, M., Bronlund, J., and Mawson, A. (2006) Moisture sorption isotherms for paper and paperboard in food chain conditions. *Packag. Technol. Sci.*, **19**, 193–209.

[99] Oliver, W. C. and Pharr, G. M. (2004) Measurement of hardness and elastic modulus by instrumented indentation: Advances in understanding and refinements to methodology. *J. Mater. Res.*, **19**, 3–20.

[100] Kese, K., Li, Z.-C., and Bergman, B. (2005) Method to account for true contact area in soda-lime glass during nanoindentation with the Berkovich tip. *Mater. Sci. Eng. A-Struct.*, **404**, 1–8.

[101] Erko, M. (2012) *Water properties in confined geometry*. Ph.D. thesis, Montanuniversität Leoben.

[102] Morak, R. (2013) *Structure and sorption analysis of wood templated ceramics*. Master's thesis, Montanuniversität Leoben.

[103] Anderson, R. B. (1946) Modifications of the Brunauer, Emmett and Teller Equation. *J. Am. Chem. Soc.*, **68**, 686–691.

[104] de Boer, J. H. (1953) *The dynamical character of adsorption*. Clarendon Press, Oxford.

[105] Guggenheim, E. A. (1966) *Application of Statistical Mechanics*. Clarendon Press, Oxford.

[106] Delwiche, S. R., Pitt, R. E., and Norris, K. H. (1991) Examination of starch-water and cellulose-water interactions with near infrared (nir) diffuse reflectance spectroscopy. *Starch-Stärke*, **43**, 415–422.

[107] Kreiml, P., Ganser, C., Bernt, I., Morak, R., Paris, O., and Teichert, C. (2014). unpublished.

[108] Zhou, S., Tashiro, K., Hongo, T., Shirataki, H., Yamane, C., and Ii, T. (2001) Influence of water on structure and mechanical properties of regenerated cellulose studied by an organized combination of infrared spectra, X-ray diffraction, and dynamic viscoelastic data measured as functions of temperature and humidity. *Macromolecules*, **34**, 1274–1280.

[109] Yakimets, I., Paes, S. S., Wellner, N., Smith, A. C., Wilson, R. H., and Mitchell, J. R. (2007) Effect of water content on the structural reorganization and elastic properties of biopolymer films: a comparative study. *Biomacromolecules*, **8**, 1710–1722.

[110] Sun, S., Mitchell, J. R., MacNaughtan, W., Foster, T. J., Harabagiu, V., Song, Y., and Zheng, Q. (2009) Comparison of the mechanical properties of cellulose and starch films. *Biomacromolecules*, **11**, 126–132.

[111] Nissan, A. H. (1976) H-bond dissociation in hydrogen bond dominated solids. *Macromolecules*, **9**, 840–850.

[112] Lee, S.-H., Wang, S., Pharr, G. M., Kant, M., and Penumadu, D. (2007) Mechanical properties and creep behavior of lyocell fibers by nanoindentation and nano-tensile testing. *Holzforschung*, **61**, 254–260.

[113] Götze, K. (1967) Die Fadenbildung. Götze, K. (ed.), *Chemiefasern nach dem Viskoseverfahren*, pp. 525–580, Springer Berlin Heidelberg.

[114] Ganser, C., Gasparic, P., Zöhrer, S., Niegelhell, K., Czibula, C., Miletzky, A., Teichert, C., Stana-Kleinschek, K., Schennach, R., and Spirk, S. (2014) Interactions of birch xylan with cellulose thin films - a QCM-D and AFM study. *In preparation for submission to Cellulose*, **n/a**, 1–X.

[115] Czibula, C. (in preparation) *Roughness analysis and chemical contrast of cellulose model films studied by atomic force microscopy*. Master's thesis, Montanuniversitaet Leoben.

[116] Heinz, W. F. and Hoh, J. H. (1999) Spatially resolved force spectroscopy of biological surfaces using the atomic force microscope. *Trends Biotechnol.*, **17**, 143–150.

[117] Akari, S., Horn, D., Keller, H., and Schrepp, W. (1995) Chemical imaging by scanning force microscopy. *Adv. Mater.*, **7**, 549–551.

[118] Akari, S., Korte, M., and Kühn, H. A. (2006) The colours of molecules. *Imaging & Microscopy*, **8**, 46–47.

[119] Butt, H.-J., Cappella, B., and Kappl, M. (2005) Force measurements with the atomic force microscope: Technique, interpretation and applications. *Surf. Sci. Rep.*, **59**, 1–152.

[120] Weber, F., Ganser, C., Teichert, C., Schennach, R., Bernt, I., and Eckhart, R. (2014) Application of the Page-equation on viscose fibre - handsheets. *submitted to Cellulose*, **n/a**, 1–9.

[121] Schmied, F. J., Teichert, C., Kappel, L., Hirn, U., and Schennach, R. (2012) Joint strength measurements of individual fiber-fiber bonds: An atomic force microscopy based method. *Rev. Sci. Instrum.*, **83**, 073902 –073902–8.

[122] Jansen, H. P., Sotthewes, K., Ganser, C., Teichert, C., Zandvliet, H. J., and Kooij, E. S. (2012) Tuning kinetics to control droplet shapes on chemically striped patterned surfaces. *Langmuir*, **28**, 13137–13142.

[123] Saketi, P., Hirvonen, J., Lai, Y., Ganser, C., Teichert, C., Järnström, J., Fardim, P., and Kallio, P. (2014) Automated drop-on-fiber contact angle measurement using a microrobotic platform. *Nord. Pulp Pap. Res. J.*, **29**, 225–231.